Dissertation

Zur Erlangung des akademischen Grades eines Doktors der Naturwissenschaften (Dr. rer. Nat.)

an der Fakultät für Mathematik, Informatik und Naturwissenschaften

Fachbereich Physik der Universität Hamburg

Alternating Magnetic Field Triggered Nanoplatform in Biomedical Application of Drug Delivery

Vorgelegt von

Kai-Wei Lin

geboren am 17.11.1990

in Taipei City

Institut für Nanostruktur- und Festkörperphysik (INF)

Hamburg, 2024

Abstract

For decades, drug delivery has been broadly discussed but it is still one of the most fascinating topics in biomedical field.[1] There are so far a lot of strategies which have greatly helped to convert promising therapeutics into successful therapies. [2, 3] From another side, the development of nanoscience, in which various of nanoscopic technologies and materials have been investigated, made significant contributions for drug delivery system. However, there are still challenging issues and factors need to be optimized such as trigger mechanism[4], cargo platforms[5] and so on. There are therefore still potential and strong reasons to discover and enhance the drug delivery technologies. Referring to controllable activation, magnetic trigger is one of the most common and promising physical strategies for drug delivery improvement.[4] As magnet fields have excellent tissue penetration and also have been applied in magnetic resonance imaging (MRI) with entire body[6], drug delivery system can be designed based on magnet field activations as well. In particular, alternating magnet field with high frequency (>10 kHz) can induce the magnetically responsive nanoparticles for heat generation.[7] In another hand, too strong heat generation causes hyperthermia and the controversies can be resulted. Not only malignant cells but also healthy cells can be damaged due to non-selectivity of treatment.[8] This property with pros and cons is thus an inspiration to construct drug cargo platforms, which are receptive from local heat triggered from alternating magnet field (AMF) and also averting hyperthermia for decreasing cytotoxicity.

In this thesis, technologies and developments of alternating magnet field in biomedical applications are discussed. Magnetic nanoparticles (MNPs) have been produced. Importantly, two drug cargo platforms with MNPs have been introduced: Metal-organic frameworks (MOFs) and polyelectrolyte multilayer-capsules (PEMCs). In the main project, zinc-dopped iron oxide nanoparticles (Zn-IONPs) with ligands oleic acid (OA) as representative MNPs have been synthesized and modified with citric acid, coated with zeolitic imidazolate framework-8 (ZIF-8), which is porous structure for drug cargo. Nanoparticles Zn-IONPs@ZIF-8 were loaded with coumarin and packed with electrolyte polymer poly(sodium-4-styrene sulfonate) (PSS) and poly(allylamine) hydrochloride (PAH). This nanomaterial was uptaken from HeLa cells in cell culture and the whole system was inspected in AMF. With different conditions of AMF treatment regional heat generated from Zn-IONPs led to breakage of electrolyte polymer and increase molecular

diffusion of coumarin, which brought out drug release. Based on the result, it was confirmed that there was weak release but not significant overall. Thus, in side project, ferromagnetic iron oxide nanoparticles (IONPs) involved PEMCs as drug cargo loaded with calcein have been discussed. PEMCs consisted of electrolyte polymers PAH and PSS, which covered spherical template calcium carbonate ($CaCO_3$) layer by layer. As the same strategy as mentioned, IONPs involved PEMCs loaded with calcein were uptaken from Hela cells as well and treated with AMF. Due to contribution of AMF, IONPs generated regional heat and broke the multilayers-structure of PEMCs, which led to calcein release. Based on results, PEMCs were not controllable with AMF. There was leakage before treatment and few release afterwards. However, there is still potential from PEMCs in application of drug release.

Overall, two different platforms as drug cargo triggered with AMF are investigated in cell culture. It is concluded that magnetism as a trigger for drug release can be accomplished. Although there are still several issues needed to be concerned and optimized, however, it is an improvement that magnetism could be one of the outstanding options applied for controllable drug release.

Zusammenfassung

Seit Jahrzehnten wird die Wirkstofffreisetzung intensiv diskutiert, aber sie bleibt eines der faszinierendsten Themen im biomedizinischen Bereich. Bisher gibt es viele Strategien, die maßgeblich dazu beigetragen haben, vielversprechende Therapeutika in erfolgreiche Therapien umzuwandeln. Auf der anderen Seite hat die Entwicklung der Nanowissenschaften, in denen verschiedene nanoskopische Technologien und Materialien untersucht wurden, bedeutende Beiträge für die Wirkstofffreisetzungssysteme geleistet. Dennoch gibt es weiterhin herausfordernde Probleme und Faktoren, die optimiert werden müssen, wie z.B. Auslösemechanismen, Trägerplattformen und so weiter. Daher gibt es nach wie vor Potenzial und starke Gründe, die Technologien zur Arzneimittelabgabe zu entdecken und zu verbessern. In Bezug auf die kontrollierbare Aktivierung ist der magnetische Auslöser eine der gebräuchlichsten und vielversprechendsten physikalischen Strategien zur Verbesserung der Wirkstofffreisetzung. Da Magnetfelder eine ausgezeichnete Gewebedurchdringung aufweisen und auch in der Magnetresonanztomographie (MRT) am gesamten Körper angewendet wurden, kann das Wirkstofffreisetzungssystem ebenfalls auf Magnetfeldaktivierungen basieren. Insbesondere kann ein sich abwechselndes Magnetfeld mit hoher Frequenz (> 10 kHz) die magnetisch reaktionsfähigen Nanopartikel zur Wärmeerzeugung aktivieren. Andererseits kann eine zu starke Wärmeerzeugung Hyperthermie verursachen, was zu Kontroversen führen kann. Sowohl bösartige als auch gesunde Zellen können aufgrund der Nichtselektion des Treatments geschädigt werden. Diese Eigenschaft mit Vor- und Nachteilen ist somit eine Inspiration zur Konstruktion von Arzneimittelträgerplattformen, die auf lokale, durch ein wechselndes Magnetfeld (AMF) ausgelöste Wärme ansprechen und gleichzeitig Hyperthermie vermeiden, um die Zytotoxizität zu verringern.

In dieser Thesis werden Technologien und Entwicklungen des Wechselmagnetfelds in biomedizinischen Anwendungen diskutiert. Magnetische Nanopartikel (MNPs) wurden hergestellt. Besonders wichtig ist, dass zwei Arzneimittelträgerplattformen mit MNPs vorgestellt wurden: Metall-organische Rahmenstrukturen (MOFs) und Polyelektrolyt-Multilayer-Kapseln (PEMCs). Im Hauptprojekt wurden zinkdotierte Eisenoxid-Nanopartikel (Zn-IONPs) mit Liganden wie Ölsäure (OA) als repräsentative MNPs synthetisiert und mit Zitronensäure modifiziert, beschichtet mit einem zeolitischen Imidazolate-Rahmen-8 (ZIF-8), einer porösen Struktur für Arzneimittelträger. Die

Nanopartikeln Zn-IONPs@ZIF-8 wurden mit Coumarin beladen und mit dem Elektrolytpolymer Poly(Natrium-4-styrolsulfonsäure) (PSS) und Poly(allylaminhydrochlorid) (PAH) verpackt. Dieses Nanomaterial wurde von HeLa-Zellen in Zellkultur aufgenommen, und das gesamte System wurde im AMF untersucht. Bei unterschiedlichen Bedingungen der AMF-Behandlung führte die regionale Wärme, die von Zn-IONPs erzeugt wurde, zu einer Zerstörung des Elektrolytpolymers und einer erhöhten molekularen Diffusion von Coumarin, was zur Freisetzung des Medikaments führte. Basierend auf dem Ergebnis wurde bestätigt, dass eine schwache Freisetzung, jedoch insgesamt nicht signifikant, stattfand. Im Subprojekt wurden ferromagnetische Eisenoxid-Nanopartikel (IONPs), die in PEMCs als Arzneimittelträger mit Calcein geladen waren, diskutiert. Die PEMCs bestanden aus den Elektrolytpolymeren PAH und PSS, die schichtweise die kugelförmige Vorlage Calciumcarbonat ($CaCO_3$) bedeckten. Nach der gleichen Strategie, wie bereits erwähnt, wurden die IONPs, die in PEMCs mit Calcein geladen waren, ebenfalls von HeLa-Zellen aufgenommen und mit AMF behandelt. Aufgrund des Beitrags des AMF erzeugten die IONPs regionale Wärme und brachen die Multilayer-Struktur der PEMCs, was zur Freisetzung von Calcein führte. Basierend auf den Ergebnissen waren die PEMCs nicht kontrollierbar mit AMF. Es gab ein Auslaufen vor der Behandlung und nur wenige Freisetzungen danach. Dennoch besteht weiterhin Potenzial der PEMCs in der Anwendung der Wirkstofffreisetzung.

Insgesamt werden zwei verschiedene Plattformen als Arzneimittelträger, die durch AMF ausgelöst werden, in der Zellkultur untersucht. Es wird festgestellt, dass Magnetismus als Auslöser für die Freisetzung von Wirkstoffen realisiert werden kann. Obwohl es weiterhin mehrere Aspekte gibt, die berücksichtigt und optimiert werden müssen, ist es ein Fortschritt, dass Magnetismus eine der herausragenden Optionen für eine kontrollierbare Wirkstofffreisetzung sein könnte.

Content

Abbreviations

Sorted by alphabet:

2-MeIM	2-methylimidazole
2PLSM	Two-photon Laser Scanning Microscopy
ACS	American Cancer Society
AMF	alternating magnetic field
$CaCO_3$	calcium carbonate
CLSM	laser scanning microscopy
Co	Cobalt
DDA	Dodecylamine
DLS	Dynamic Light Scattering
DMEM	Dulbecco's Modified Eagles Medium
DMF	N,N-dimethylformamide
EDTA	Ethylenediaminetetraacetic acid
Fe	Iron
$Fe(acac)_3$	iron(III) acetylacetonate
Fe_3O_4	magnetite
FL-spectra	Fluorescence Spectrometer
FPA	focal plane array
ICP-MS	Inductively Coupled Plasma Mass Spectrometry
IONP	iron oxide nanoparticle
IR	Infrared Radiation
LbL	Layer-by-Layer
LSM	laser scanning microscopy
MeOH	Methanol
MNP	magnetic nanoparticle
MOF	metall-organic framework
MRI	magnetic resonance imaging
NaOH	Sodium Hydroxide
Ni	Nickel
NNI	National Nanotechnology Initiative
OA	oleic acid

P/S	Penicillin-Streptomycin
PAH	poly(allylamine) hydrochloride
PBS	Phosphate-Buffered Saline
PEMC	polyelectrolyte multilayer-capsule
PMA	Poly(isobutylene-alt-maleic anhydride)
PSS	poly(sodium-4-styrene sulfonate)
SAR	specific absorption rate
SEM	scanning electron spectroscopy
TAMRA	Tetramethylrhodamine
TEA	Triethylamine
TEM	transmission electron spectroscopy
THF	Tetrahydrofuran
ZIF-8	zeolitic imidazolate framework - 8
$Zn(NO_3)_2 \cdot 6H_2O$	Zinc Nitrate Hexahydrate
Zn-IONP	zinc doped iron oxide nanoparticle
$\gamma\text{-}Fe_2O_3$	maghemite

Symbols

B	Magnetic flux intensity
B_R	Magnetization due to the interaction between the magnetic domains
f	Frequency
H	Magnetizing force
H_0	Magnetic field intensity
H_c	Coercivity
k_B	Boltzmann-constant
K_u	Anisotropy constant
M_s	Magnetization
T	Temperature
V_H	Hydrodynamic volume
V_M	Primary volume of the particles
ΔG	Gibbs Free Energy
η	Viscosity

μ	Chemical potential
μ_0	Permeability of free space
τ_0	Attempt time
τ_B	Brownian relaxation time
τ_N	Néel relaxation time
χ_0	Susceptibility

Introduction

Nanotechnology has emerged as one of the most promising fields of research and development in the 21st century. The prefix "nano," derived from the Greek word for "dwarf," denotes a scale of one-billionth of a meter (10^9 m).[9] According to the National Nanotechnology Initiative (NNI) in the United States, nanotechnology encompasses the research and application of materials at the nanoscale, characterized by their unique physical, chemical, and biological properties.[9] The conceptual foundation of nanotechnology was articulated by American physicist and Nobel laureate Richard Feynman in his 1959 lecture titled "There's Plenty of Room at the Bottom," which forecasted a promising future for the field.[10] Today, as Feynman's hypothesis becomes a reality, there has been an explosive growth in the understanding and application of nanotechnology across various disciplines. However, two critical questions remain regarding the exploration of the "nano-world": How are nanoparticles produced? How are they observed?

To synthesize nanomaterials, two primary approaches have been developed: the top-down and bottom-up methods.[9, 11] The top-down approach involves the reduction of bulk materials into nanoparticles, while the bottom-up approach focuses on constructing nanostructures atom by atom or molecule by molecule through various physical and chemical processes. A notable example of the bottom-up strategy is self-assembly, whereby atoms and molecules spontaneously organize into ordered nanostructures through intermolecular interactions. Both methodologies give rise to diverse physical, chemical, and biological strategies for nanoparticle synthesis.[11]
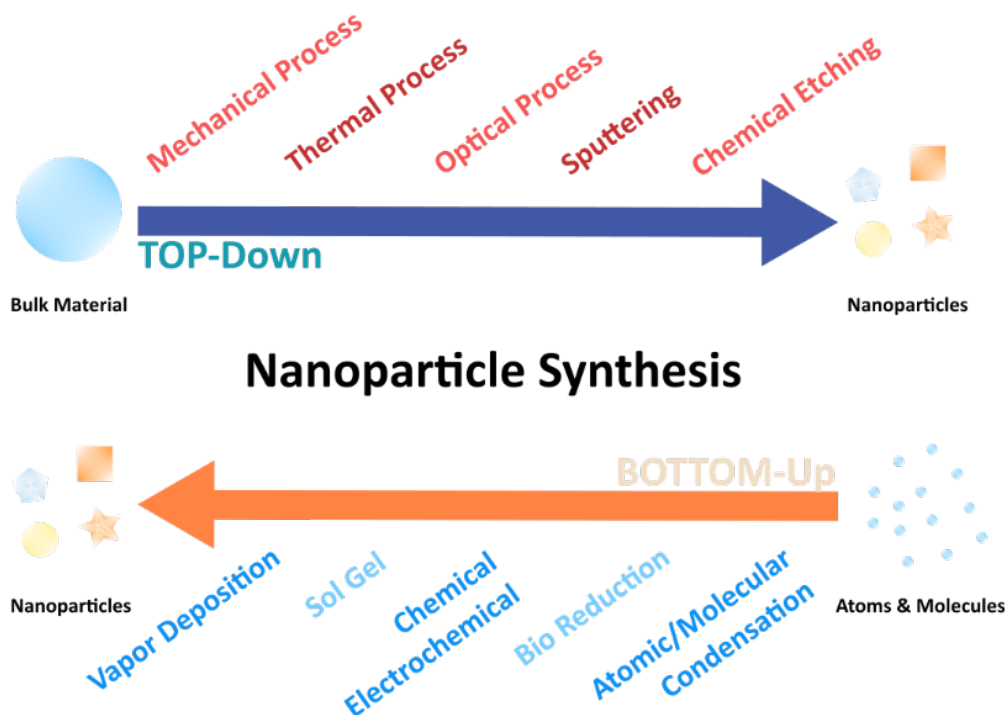
Figure 1: Illustration of top-down and bottom-up approaches. Modified from *S. Bayda et al.*[9]

Since centuries, scientists have been eager for exploring the world in small scale, and the observation in tiny space is always an eager for understanding objects, structures and phenomena which cannot be recognized by human eyes. With the improvements of techniques, there are various kinds of microscopic system demonstrating the knowledges of materials in small scales, including size, geometry and other characteristics. Advancements in microscopy have facilitated the observation of objects that are imperceptible to the naked eye. Various forms of microscopy, including optical, electron, X-ray, and scanning probe microscopy, yield valuable insights into nanomaterials. Notably, electron microscopy relies on the diffraction, reflection, or refraction of electron beams interacting with the sample. The scattered radiation and other signals produced from this interaction are collected to generate an image. For example, two widely used techniques for analyzing size, shape, and size distribution are Scanning Electron Microscopy (SEM) and Transmission Electron Microscopy (TEM). SEM produces images by directing a focused electron beam across the sample's surface, generating various signals that provide information about its topography and composition. Conversely, TEM utilizes a beam of electrons transmitted through the sample to form an image, enabling the

examination of materials at the nanoscale. Furthermore, light microscopy introduced the optical observation, by which the light or fluorescent properties of specimens can be characterized. Since the nanotechnologies, including synthesis and observation, has been broadly developed, it is meaningful to apply these technologies in various fields for solving issues or optimization.

Besides, the development of nanotechnology offers support for solving problems in human civilization, especially issues related to life and health. Cancer, one of the most threatening issues causing unnatural death worldwide, is a group of deceases involving abnormal cell growth with potential to invade or spread to other body parts. According to the report from F. Bray and their co-workers based on updated estimates from International Agency for Research on Cancer (IARC) in 2022, there were around 20 million cancers cases newly diagnosed and 9.7 million patients died from cancer.[12]

In recent decades, interest in the application of nanoparticles in biomedicine has risen steadily, particularly in areas such as bioimaging[13-15], biosensors[16-18], and drug delivery systems.[19, 20] The development of controllable drug release systems shows significant potential for advancing therapeutic interventions. A key challenge in this domain is understanding how external stimuli interact with nanomaterials. Questions regarding the nature of these interactions and their controllability are essential for the successful construction of such systems. Various external stimuli, including light[21], magnetic fields, electric fields, and ultrasound, have been explored for use in drug delivery systems, with magnetic fields eliciting considerable interest. Notably, the use of iron oxide nanoparticles (IONPs) has attracted significant scholarly attention due to their exceptional chemical, biological, and magnetic properties, which offer promising opportunities for drug release applications. This thesis discusses two distinct nanomaterials as drug carriers triggered by alternating magnetic fields (AMF). In the main project, IONPs are coated with the porous structure ZIF-8, incorporating coumarin and encapsulated with polyelectrolyte layers. In the side project, polyelectrolyte multilayer films (PEMCs) are fabricated with IONPs sandwiched between polyelectrolyte layers and loaded with calcein. Both nanoparticle platforms are subjected to AMF treatment, and their drug release profiles have been investigated.

1.   Theories and Technical Supports

1.1. Magnetism

Magnetism is a scientific phenomenon that has been documented for over two millennia.[22] It encompasses a range of properties that manifest in the presence of a magnetic field, enabling objects to attract or repel one another. Materials can be classified based on their responses to magnetic fields, leading to a categorization of their magnetic behavior. The two predominant forms of magnetism are diamagnetism and paramagnetism.[23, 24]

Diamagnetism is characterized by the tendency of materials to be repelled by an external magnetic field. When an external magnetic field is applied, a magnetic field is induced within the material, oriented in the opposite direction, which consequently results in a repulsive force. This phenomenon is observed in all materials; however, a material is classified as diamagnetic only when its magnetic behavior is solely attributable to diamagnetism in its interaction with the magnetic field.[23-25]

In contrast, paramagnetism represents a different type of magnetic behavior, whereby materials exhibit a weak attraction to an external magnetic field. In this instance, materials generate an induced magnetic field that aligns in the same direction as the externally applied field. Unlike diamagnetism, paramagnetism arises from the presence of unpaired electrons within the material. In the field of chemistry, each atomic orbital within an atom is capable of housing two electrons with opposing spins, forming an electron pair. Due to the opposite spins of the paired electrons, their magnetic dipole fields cancel each other out, resulting in no net dipole moment. When an atom has a single electron occupying an orbital, that unpaired electron generates a magnetic dipole moment due to its inherent spin. Consequently, atoms with unpaired electrons exhibit magnetic dipoles and interact with external magnetic fields. The alignment of all magnetic dipole moments with the external magnetic field is indicative of paramagnetism.[24, 26, 27]

While both diamagnetism and paramagnetism exhibit opposing magnetic behaviors, it is noteworthy that they are not permanent effects and dissipate in the absence of an external magnetic field. However, a distinct category of magnetism exists known as

ferromagnetism, which is characterized by materials that display unique properties and significant potential for diverse applications across various fields.[24]

Diamagnetism

H=0   H →

Paramagnetism
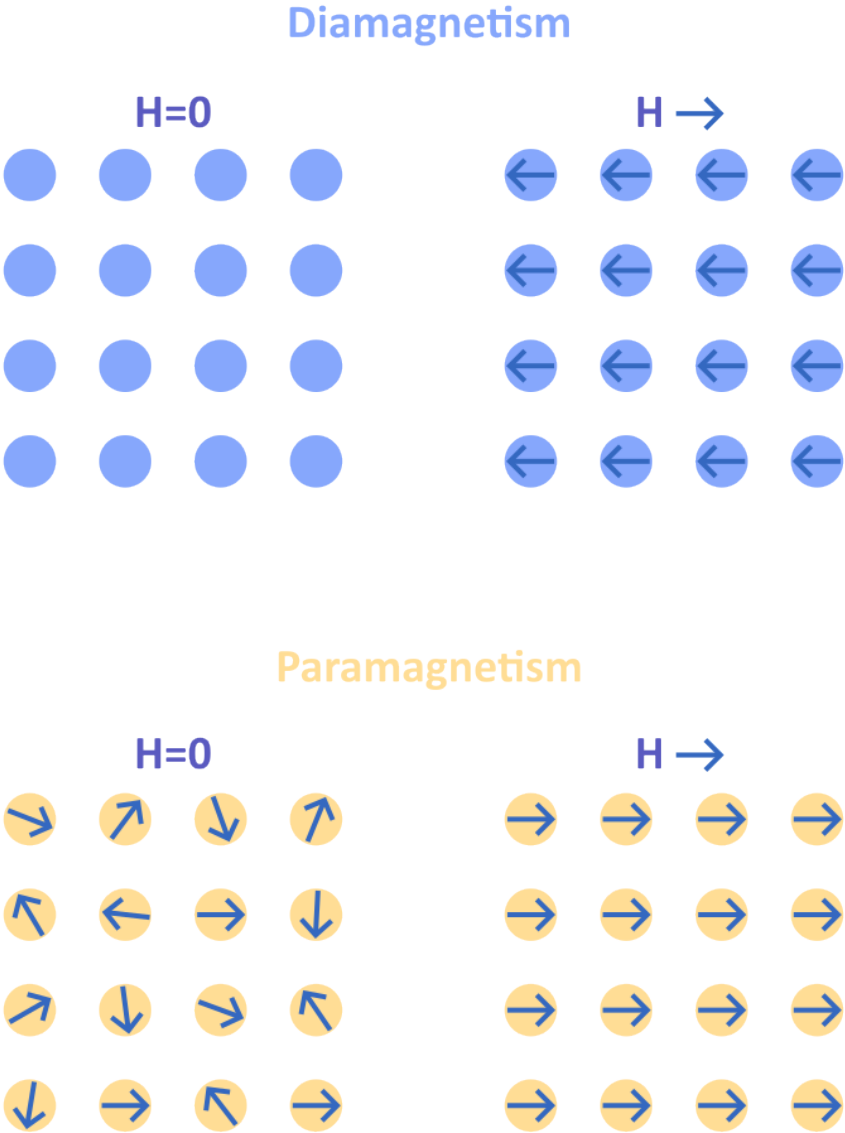
H=0   H →

Figure 2:   Schematic representation of diamagnetism and paramagnetism.

1.1.1.   Ferromagnetism and Superparamagnetism

Magnetic permeability defines the induced magnetization of a material based on the contribution of external magnetic field. The more magnetic moments aligned with magnetic field, the higher magnetization. In comparison with diamagnetism and

paramagnetism, several materials show strong magnetic coercivity. After magnetization and removing external magnetic field, partial magnetic moments (domains) still remain alignment and show permeability, which is defined as ferromagnetism.[28] The materials can, therefore, be form as a permanent magnet and attracted to another magnet. This specific magnetic stand is termed as ferromagnetism, which only exists in few materials such as pure form, oxides, alloys or compounds of several transition metals and rare-earth metals[28].

Apart from above, another specific phenomenon is superparamagnetism which directs the magnetic behavior when the size of ferromagnetic or ferrimagnetic particles are so small that each particle are approximated as a giant single magnetic domain.[29, 30] Depending on the material, size can be from a few to one or two hundred of nanometers. The appearance of magnetic property is based on (unpaired) electron coupling, which leads to the single magnetic domain (vectoral magnetic moment) in each crystal. Before the introduction of a magnetic field, the magnetic moments of and superparamagnetic particles reverse easily and randomly between crystallographic axis so that there is no magnetic moment in entirety. Following this, an external magnetic field directs the alignment of magnetic moments, especially superparamagnetic particles showing high magnetic susceptibility that even a relatively weak magnetic field are enough for alignment. Different from ferromagnetism, the removement of external magnetic field causes randomization of superparamagnetic particles due to thermal agitation, which is defined as Néel relaxation.[31, 32] From another hand, particles including their magnetic moments are able to rotate by introducing and then removing external magnetic field, termed Brownian relaxation. [31, 32]

Both magnetic states are able to convert electromagnetic energy to thermal energy.[33, 34] In principle, hysteresis loss and relaxation loss are the main heating mechanisms and different magnetism determines which heat mechanism is dominant.[35, 36] While hysteresis loss significantly arises in ferromagnetic materials,[36, 37] relaxation loss mainly takes place from superparamagnetic materials.[31, 35]
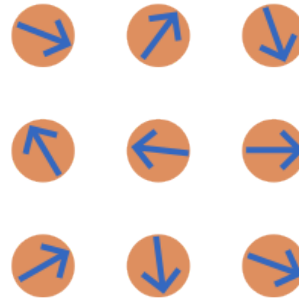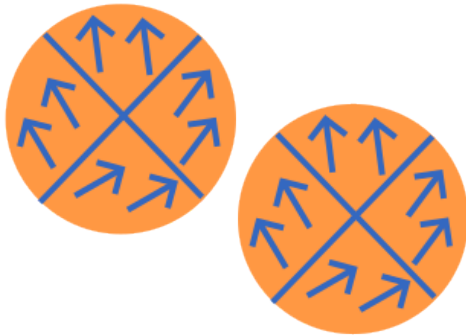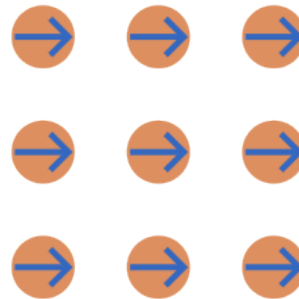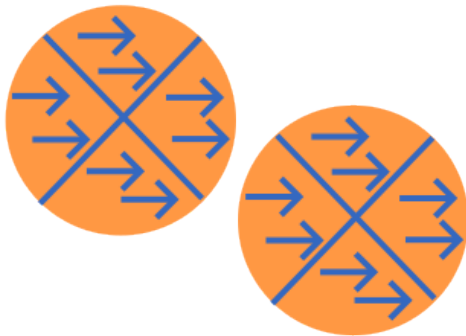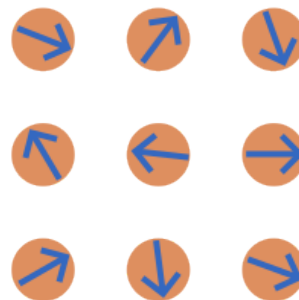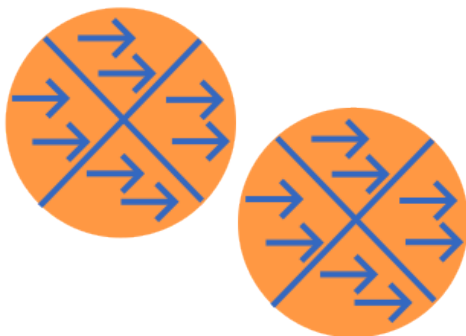
Figure 3: Schematic representation of interaction between magnetic field and magnetic particles with ferromagnetism and superparamagnetism. Image modified from *D. Alcantara et al.*[38]

1.1.2.   Hysteresis Loss and Relaxation Loss

Magnetic hysteresis is a phenomenon from ferromagnetic materials and it is described as a lag of magnetic flux intensity (B) behind magnetic field strength or magnetizing force (H). As shown in Figure 4, magnetic moments of ferromagnetic material are in random orientation in the beginning with zero field value (origin of coordinate in Figure 4). Once a magnetic field appears, magnetic moments are orientated by the magnetic field and the material is magnetized until saturation (M_s) due to the alignment of all magnetic moments. When the magnetic field turns back to zero, the ferromagnetic material remains, however, a certain extent or even considerable degree of magnetization due to the interaction between the magnetic domains ($+B_R$). In this situation, there must be a reserved and increased magnet field applied to drop the magnetization of material back to zero again, which is coercivity ($\pm H_c$, B=0).

Figure 4:   Image of hysteresis loop describing magnet response of ferromagnetic material. Image cited from *I. Altpeter et al.*[20]

Subsequently, magnetic moments align in opposites direction and reach saturated magnetization if the reversed magnet field maintains. The whole process as is a cycle as complete loop, which is known as a hysteresis loop. Due to agitation of magnetic moments
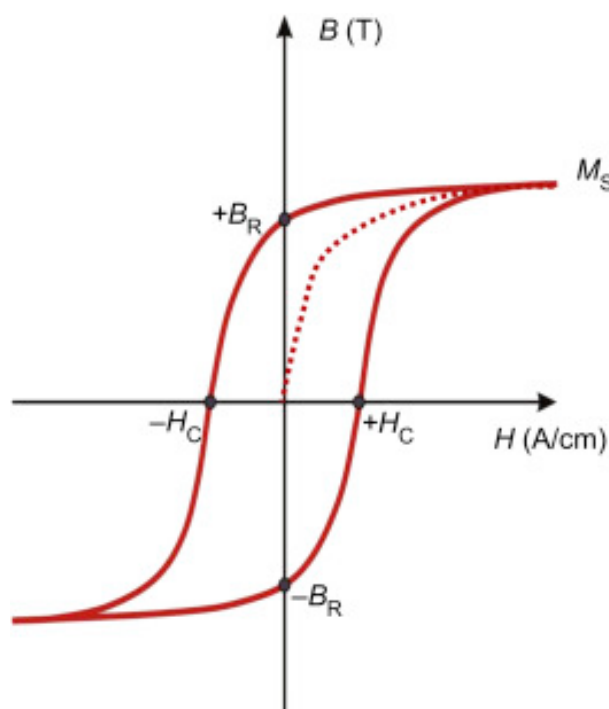
and overcoming their resistance, there is heat generation as energy lost in the cycle, which is hysteresis loss.

Concerning superparamagnetism, it is suggested from *Rosensweig* that both relaxations take place with independency[39] and time of both Néel relaxation τ_N and Brownian relaxation τ_B can be represented by

$$\tau_N = \tau_0 \exp\left(\frac{K_u V_m}{k_B T}\right) \qquad (1)$$

$$\tau_B = \frac{3\eta V_H}{k_B T} \qquad (2)$$

where τ_0, K_u, V_M, k_B, T, η, and V_H indicate the attempt time, anisotropy constant, primary volume of the particles, Boltzmann-constant, temperature, solvent viscosity, and hydrodynamic volume of the particles, respectively. Due to the independency of both relaxations, the effective relaxation time τ can be expressed by

$$\frac{1}{\tau} = \frac{1}{\tau_N} + \frac{1}{\tau_B} \qquad (3)$$

And the power dissipation P can be further demonstrated by:

$$P = \pi\mu_0\chi_0 H_0^2 f \frac{2\pi f\tau}{1 + (2\pi f\tau)^2} \qquad (4)$$

where μ_0, χ_0, H_0 and f denote permeability of free space, susceptibility, magnetic field intensity and frequency, respectively. This equation demonstrates that the magnetic relaxations contribute the conversion from electromagnetic energy to thermal energy. Ferromagnetic and superparamagnetic materials are valuable as magnetic thermal triggers for further applications.
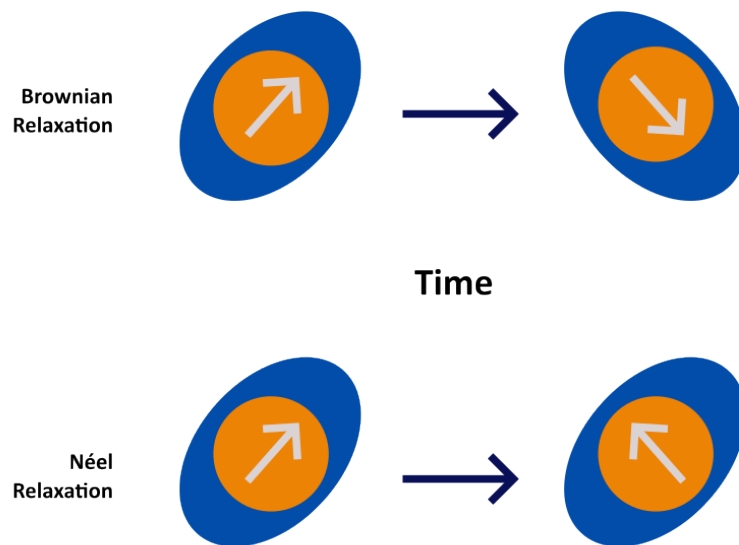
Figure 5: Schematic illustration demonstrating process of Néel relaxation and Brownian relaxation.

1.2. Magnetic Nanoparticles

Magnetic nanoparticle (MNP) as a concept describes particle in nanoscale with magnetic properties. Since decades, MNPs offer attractive possibilities and are being intensively investigated in nanomedical field. Base on development of technologies so far, the size of particles can be controlled from single to tens of nanometers, which is comparable to various of biological units such as a cell, a virus, a protein, etc.[40] Furthermore, in order to optimize the efficiency of therapeutic treatment, materials with strongly saturated magnetization are premeditated. Specifically, there is high potential from transition metals (Fe, Co, Ni, etc.) and metal oxides (Fe_3O_4, γ-Fe_2O_3, etc.). Pure metals possess the highest saturation of magnetization but show high sensitivity to oxidation.[41] Thus, it is not pertinent to apply pure metal nanoparticles in biomedical field once there is no appropriate surface modifications.[42, 43] In contrast, due to less sensitivity of oxidation, metal oxides provide stable magnetic response, which is more applicable.[44] Therefore,

iron oxides as metal oxides nanoparticles are in priority for application in this project and there are several backgrounds need to be considered.

1.2.1.　　　Iron Oxide Nanoparticles (IONPs)

Considering all magnetic nanoparticles, iron oxide nanoparticles, such as magnetite (Fe_3O_4) and maghemite (γ-Fe_2O_3), are promising materials and intensively applied as their outstanding magnetic performance, simple synthesis strategies and significant low toxicity in compare with other materials like nickel or cobalt. Due to four unpaired electrons in 3d orbitals, each iron atom has a strong magnetic moment. All magnetic moments align once an external magnetic field has involved and even been taken out afterwards.

Many magnetic oxides are spinel structures. As a spinel structure, the formula is in general $M^AM^B_2X_4$, where M^A and M^B are tetrahedrally and octahedrally coordinated respectively. Normally, there are two kinds of spinel structure: Normal spinel structure and inverse spinel structure. As normal spinel structure, there is close-packed array of anions, in which A-site cations fill 1/8 of the tetrahedral holes and B-sites cations occupy 1/2 of the octahedral holes. In contrast, inverse spinel has perfectly similar structure with the same large unit cell, in which, however, A-sites ions and half of B-sites ions switch places. Thus, the formular should be $M^B(M^AM^B)X_4$ for insisting the inverse structure.

Magnetite crystallizes in inverse spinel cubic structure, which contains Fe^{3+} ions in the sites with tetrahedral oxygen coordination (A-sites, light grey in Figure 6) and mixture of Fe^{3+} and Fe^{2+} ions in the same proportion in the sites with octahedral oxygen coordination (B-sites, dark grey in Figure 6). There are 24 magnetic atoms in a magnetite unit cell, in which 8 and 16 are tetrahedrally and octahedrally coordinated, respectively. Thus, the chemical formula is written as $Fe^{3+}(Fe^{2+}Fe^{3+})O_4$ in order to insist Fe^{3+} in A-site and ($Fe^{2+}Fe^{3+}$) in B-sites.
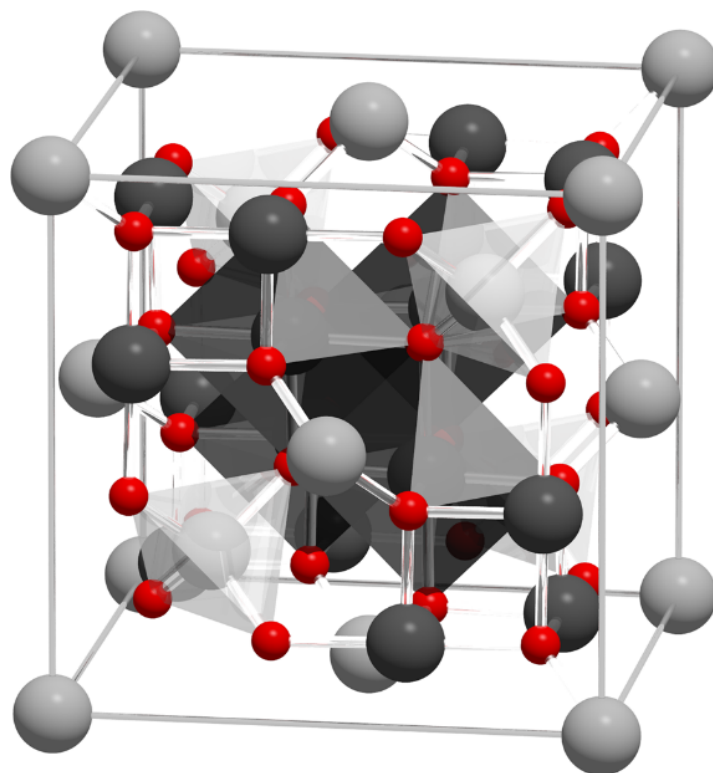
Figure 6: Visualization of magnetite unit cell. Tetrahedral (Fe^{2+}, light grey), octahedral (mixture of Fe^{2+} and Fe^{3+}, dark grey) and oxygen (red) sites are identified. Image cited from *R. Moreno et al.* [45]

To date, there are two main chemical approaches for magnetite nanoparticles synthesis: aqueous and organic-based syntheses.[46] As a typical aqueous synthesis, iron chloride $FeCl_3$ was dissolved in water as microemulsions and mixed with NaOH aqueous solution in order to increase pH value.[47] After shaking or stirring in room temperature with certain time, microemulsion phases were obtained iron oxide precipitate. The whole process, including synthesis and product collection, is simple and in mild condition. However, homogeneity from nanoparticles is still a challenging issue in this case. In order to achieve homogeneous nanoparticles, aqueous synthesis requires long time, which is not easy. Moreover, even subtle changes of experimental conditions affect the size and size distribution.[48]

In contrast, organic-based synthesis shows outstanding performance for size, shape and distribution controlling. In typical organic-based synthesis, iron(III) acetylacetonate ($Fe(acac)_3$) as precursor was added to mixture of oleic acid and benzyl ether, from which the precursor is soluble in oleic acid and react-able with it.[49] During the process, there is

exchange between acetylacetonate ion and oleate ion. Fe(acac)$_3$ is then converted in iron oleate, which is soluble in media as well.[50] Figure 7 describes the chemical equilibrium of exchange between acetylacetonate and oleate. Moreover, during vacuum or pressure atmosphere, the equilibrium breaks and will be dislocated at the left side, once that acetylacetonate is a bidentate ligand, which leads to a six-member-chelate ring while oleate is a monodentate ligand. In order to make sure iron oleate in bigger quantity, it is thus required to keep low pressure (<2 bar) to eliminate acetylacetonate.
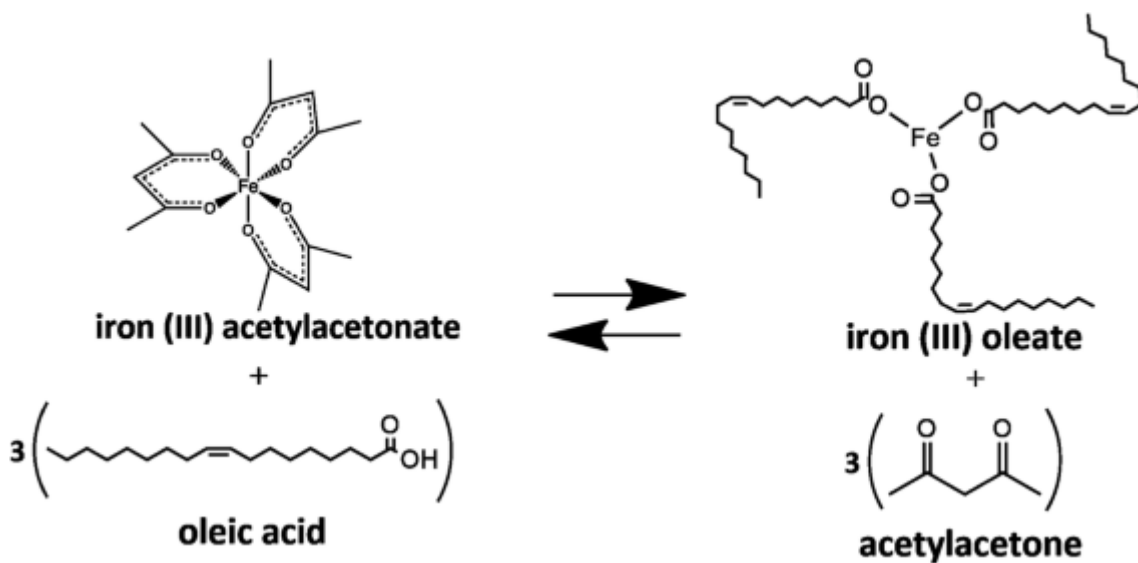
Figure 7:   Illustration of equilibrium of exchange between iron(III) acetylacetone and iron(III) oleate. Image cited from *E. Scopel et al.*[50]

Afterwards, nucleation of iron oxide occurs via heating the solution of iron-oleate complex in a long chain hydrocarbon solvent.[51] Generally, metal carboxylates decompose once they are heated and the temperature is around or even higher than 300°C.[52] As expressed by Equations 5 and 6, The decomposition takes place based on the breakage of M-O and MO-C bonds of metal carboxylate, which form radical species.

$$M - OOCR \rightarrow M^\bullet + RCOO^\bullet \quad (5)$$

$$M - OOCR \rightarrow MO^\bullet + RC^\bullet O \quad (6)$$
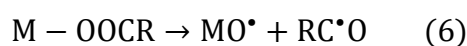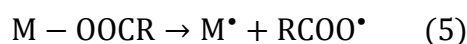
There are several paths for these radical species: recombination, self-decomposition into smaller molecules or further reaction with other metal carboxylate complexes for disseminating decomposition reaction.[51] Thermal decomposition of metal carboxylates in solid state leads to the formation of metal oxide. Based on previous outstanding work from P. K. Narnaware et al.[53], iron oxide nanoclusters are composed of magnetite (Fe_3O_4) and maghemite (γ-Fe_2O_3). These clusters aggregate once they achieve enough Gibbs free energy ΔG and, in contrast, they solubilize again if ΔG is not reached, which means the growth of clusters to particles is an irreversible process and oleate structure expose at the surface of particles as surface ligands.[50] Regarding this, general process can be summarized in three periods: thermal decomposition, nucleation and size growth, demonstrated in Figure 8.
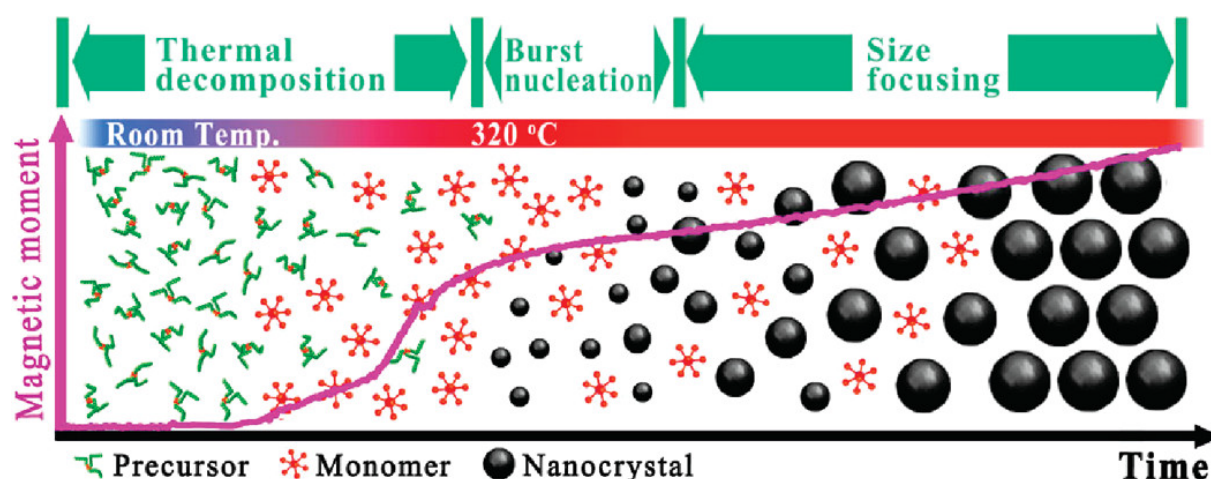
Figure 8: Kinetics of the formation of iron oxide nanoparticles. Image cited from *S. G. Kwon et al.*[51]

In addition, the determination of final structure IONPs has been investigated. Interesting, according to work from *Qiao et al*,[54] it is proposed that the equilibrium between chemical potential of monomers and the chemical potential of different crystal plane plays an important role in determination of the final particle size and shape. For magnetite, chemical potential μ of crystal planes can be rated as: $\mu\{100\}> \mu\{110\}> \mu\{111\}$, which means the crystal plane {111}, {110} and {100} possess lowest, intermediate and highest reactivity.[46, 54] In the beginning of nuclei generation, the chemical potential of monomers μ_m is higher than other chemical potential of crystal planes, termed as diffusional growth.

Subsequently, monomers will move from the solvated form with high chemical potential to the planes with lower chemical potential, which brings out the propose that activation barriers dominant the monomer depositions on each plane.[54] Initially, the growth of nucleus in 3 directions, leading to tetrahedron and octahedron formation, shown in Figure 9 b-c). During the reaction, the concentration of monomers decreases leading to μ_m reduction until {100} cannot grow anymore, i.e., μ{100}> μ_m> μ{110}> μ{111}. At the same time, however, the facets {111} and {110} are still growing, turning the octahedra to tetradecahedral structure as Figure 9 d). Afterwards, since μ_m decreases terminating {110} growing but remains μ{100}> μ{110}>μ_m>μ{111}, tetradecahedra are formed into cubes, as demonstrated in Figure 9 e). In addition, if the concentration of monomers is still high enough offering {111} growth, particles are going to be formed in star structure.
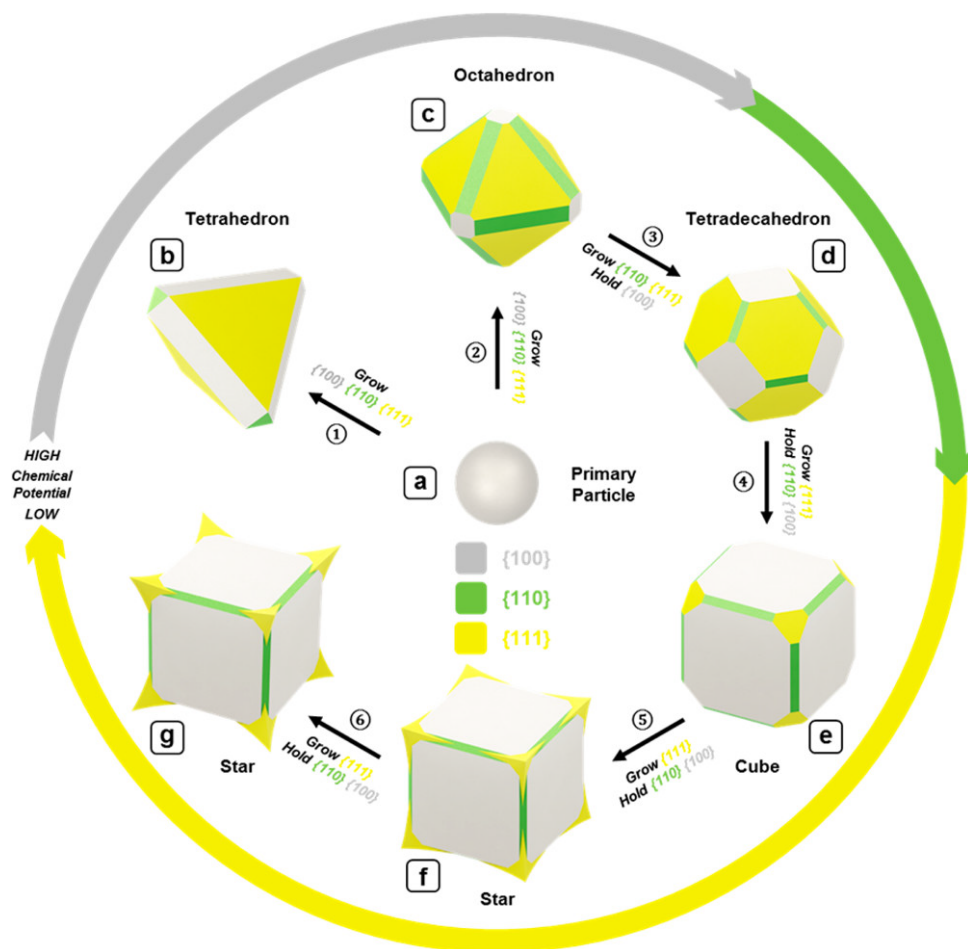

Figure 9: Schematic illustration of the proposed growth model: a) primary particle enclosed by undetermined facets; b) tetrahedron dominantly enclosed by {111}; c) octahedron dominantly enclosed by {111}; d)

tetradecahedron (truncated cube/octahedron) dominantly enclosed by {100} and {111}; e) cube dominantly enclosed by {100}; f) star dominantly enclosed by {100} with extruded ⟨111⟩ vertices; g) star with more extruded ⟨111⟩ vertices. The color gray stands for {100} planes in both the outer ring and 3D models; green, {110}; and yellow, {111}. Image cited from *Qiao et al*.[54]

1.2.2. Zinc Doping for Iron Oxide Nanoparticles (Zn-IONPs)

For ferromagnetic material, size plays a significant role in magnetization. For example, ferromagnetic materials magnetite in bulk scale own remarkable saturation magnetization of 92-100 emu/g and 60-80 emu/g respectively.[55] In contrast, nanoparticles of the same materials above, however, show lower saturation magnetization due to the high fraction of atoms on the surface of a nanoparticle.[56] The atoms at the surface have different coordination as well as dangling bonds, which causes misalignment of spins and, in other words, there is no contribution from surface atoms to the total magnetization. In addition, surface oxide effect is another important factor to weaken the total magnetization of a particle.[27]

Metal doping shows great interest for material modification and it can change the structural, electric, magnetic and other properties of the material.[57-60] As doping for iron oxide, foreign metals or elements as dopants are introduced into the structure, which can be generally formed as $M_xFe_{3-x}O_4$ and M is dopant cation like Ni^{2+}, Mn^{2+}, Zn^{2+}, Co^{2+}, Mg^{2+} and Cu^{2+}. Considering biomedical applications, there are limited options from dopant in order to prevent toxicity.

Based on the overview from *M. A. Zoroddu et al*.[61], both iron and zinc are two of the most abundant essential metal elements for human body. As 70 kg bodyweight of reference man, there are around 5 g iron and 2 g zinc in the body.[62] Zinc as an abundant essential d-metal ion plays important roles in human health. Deficiency of zinc causes risks of health hazard such as inflammation, DNA damage, dwarfism, etc.[63-66] Due to the importance of zinc ion to human body, it is highly considered that zinc ion would be biocompatible as a dopant for IONPs.
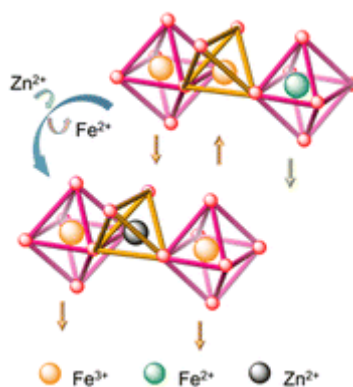
Figure 10: Illustration of the difference between iron oxide particles with and without zinc doping. Without doping, Fe^{3+} ions occupy tetrahedral and half octahedral coordination. Fe^{2+} ions occupy the rest octahedral coordination. With zinc-doping, all Zn^{2+} and Fe^{3+} ions take tetrahedral and octahedral coordination respectively. Image cited from *G. Kasparis et al.*[67]

1.3. Metal-Organic Frameworks (MOFs)

Metal-organic frameworks (MOFs) represent a class of hybrid porous materials composed of metallic ions and organic molecules, which serve as nodes and linkers, respectively, as illustrated in Figure 11. Since 1990s, the first MOF structure has been reported by Yaghi[68], who mixed $Cu(NO_3)_2 \cdot 2.5H_2O$ with 4,4'-bipyridine (4,4'-bpy) in water and demonstrated orange crystalline $Cu(4,4'\text{-bpy})_{1.5} \cdot NO_3(H_2O)_{1.25}$ framework structure. Afterwards, the development became intensive. According to Cambridge Structural Database (CSD), giant amount of MOFs structures have been registered and the number of related research publications is still increasing.[69, 70] Due to the various choices of metallic ions and organic linkers, over 90,000 MOFs have been synthesized and over 500,000 predicted.[71] There are two types of units from all MOFs, organic and inorganic. Metallic ions as the inorganic part form the core. Then organic molecules, which typically consist of carboxylates, phosphate, sulfonate and so on, connected the inorganic cores, which construct secondary building units (SBUs). This combination of organic-inorganic units leads to form a crystalline structure of MOF with high porosity. Depending on the extension points of metallic units and the number of bridging ligands from organic linkers, different secondary building unit (SBU) geometry can be achieved from simple 1-dimentional (1D) chains to 3-dimentional (3D) networks.
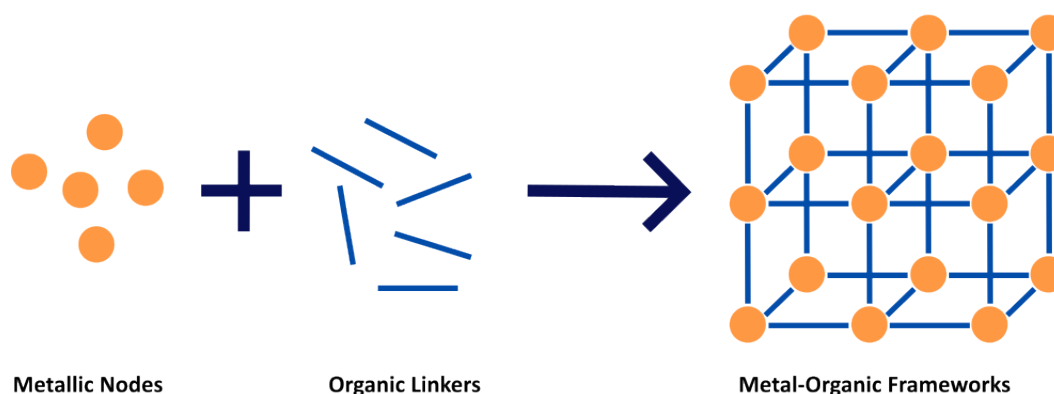
Figure 11: Schematic formulation of Metal Organic Frameworks (MOFs). Image modified from *A. F. Sahayaraj et al*.[72]

Due to high surface area and porosities, MOFs exhibit the specific properties and are often applied in catalysis, gas storage and gas separation. They can be contributed as catalysts for many reactions, including oxidation, reduction and carbon-carbon bond formation. Separation between carbon dioxide and nitrogen, hydrogen storage are other classic examples of MOFs applications. In addition to their well order and tunable porous structure, MOFs are promising materials for applications in biomedical field. Particularly, drug carrier is one of the most explored applications, from which high surface area and porosity of the structure make MOFs suitable for drug encapsulation and delivery. Loaded in pores, external adsorption from surface and chemical bonding to either metallic or organic units, these dynamics above lead to thus high interest of MOFs applied as drug cargo. So far, many MOFs structure have been reported to apply various kinds of biomedical therapies. Here, zeolitic imidazolate framework–8 (ZIF-8) is one of the most common MOFs in biomedical applications. It is a 3D structure consisting zinc ions as metallic nodes and organic 2-methylimidazole (2-MeIM). ZIF-8 holds inherent porous cavities with average size of ~12 Å along and a narrow aperture of ~3.4 Å, which offer plenty of spaces for loading guest molecules.[73] According to the work from H. Yin et al.,[74] the ZIF-8 structure will maintain in 300°C atmosphere for 24 h, including in air, water (steam) or other inert gases, which shows outstanding thermal stability. Moreover, ZIF-8 shows biocompatibility due to low toxicity of zinc ions and 2-MeIM. However, it

decomposes easily in acidic solutions due to the exchange reaction of zinc ions from binding with 2-MeIM to re-binding with other anionic groups. In comparison, ZIF-8 keeps stable in basic solutions. Thus, ZIF-8 is actively applied as a pH-responsive platform[75-77] and it is an advanced material for biomedical treatment.[59, 78, 79]
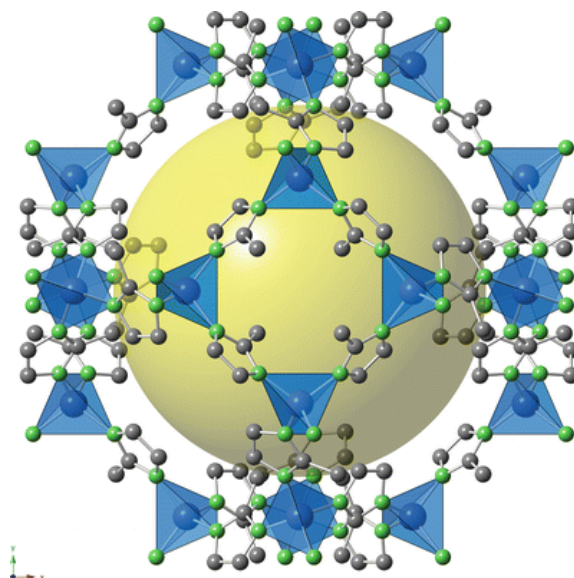
Figure 12:   Structure of the zeolitic imidazolate framework-8 (ZIF-8). Image cited from work by *N. Hara*.[80]

1.4. Polyelectrolyte Multilayers (Capsules)

Layer-by-Layer (LbL) deposition model was first published by *Iler* in 1966, who introduced the alternate layers of positively and negatively charged colloidal particles.[81] Since then, with the development of LbL-technology, the deposition of polyelectrolyte multilayers was considered intensively for surface modification. Polyelectrolytes (PEs) are macromolecular polymer compounds owning at least 10%-15% functional groups, which determine the characteristics of the polymer such as ionic charge, functionality and so on. With the contributions of electrostatic interactions, the first layer is formed by adsorption of a PE on the surface of substrate possessing opposite charges. Afterwards, PE layers can be adsorbed and form the structure substrate/(polycation/polyanion)$_n$ or substrate/(polyanion/polycation)$_n$, depending on the charge of substrates.[82] As inspiration, the technique of LbL-adsorption can modify the surface functionalities of materials.

Besides, a substrate can be decomposable by chemical or physical strategies and PEs can maintain as an independent multilayered material. According to the summary by *L. L. del Mercato et al.*,[83] polyelectrolyte multilayered capsules (PEMCs) have been actively investigated and functionalized in the past years. The fabrication of PEMCs is based on the spherical substrates with LbL-adsorption and the decomposition of the substrate afterwards. The templates can be classified as organic or inorganic, which are dissoluble in acidic and aqueous solutions respectively. They affect the properties of capsules significantly, such as size, distribution and further approaches loading molecules like drugs or dyes inside. Not only the substrates as cores, the choices of PEs as shell structure play an important role due to their influences to biocompatibility and decomposability in cell culture. Capsules can be functionalized as optical, magnetic or photothermal responsive materials by the introduction of inorganic charged nanoparticles between the multilayers or inside the cores. Different nanoparticles endue various important characteristics to capsules such as labeling, controllable triggers and so on. Regarding to magnetism, the introduction of magnetic nanoparticles offers specific magnetic applications to capsule systems such as magnetic resonance imaging (MRI), directing by external magnet, AMF responsive drug cargo and so on.[84]

Considering cytotoxicity, it is possible that the main sources for toxicity come obviously from the PEs composing the wall and from the functionalities embedded in the cavity and (or) in the wall, even it is so far still not well studied.[83] Interestingly, polycations with positive charge can damage the cellular membrane with following activation of signaling pathways, which leads to mitochondrial depolarization and generation of reactive oxygen species causing cell death.[85-88] Thus, the cationic charge density of the polycations need to be considered for reducing cell damage. In addition, once polycations possess amine functionalities, they may increase interaction with anionic intracellular components and lead to oxygen-independent cell death as well.[89] Thus, in order to reduce toxicity, it is suggested to consider the functionalities which are already applied and reported in cell culture and biomedical treatment. So far, sodium poly(styrene sulfonate, sodium salt) (PSS), poly(allylamine hydrochloride) (PAH) and polydiallyl dimethyl ammonium chloride (PDADMAC) have been broadly applied in , from which PSS possessing negative charge can adsorb positively charged polyelectrolytes PAH and PDADMAC. According to the work from *N. Brkovic et al.*,[90] capsules with (PSS/PAH)$_x$/AuNPs/PAH/PSS layer geometry are prepared for photothermal responsive drug cargo. From their report,

hollow capsules with various dyes were uptaken from different cells and the release could be controlled with light due to introducing photothermal sensitive AuNPs. Furthermore, another outstanding work from S. Carregal-Romero demonstrated magnetically triggered release of microcapsules with introduction of iron oxide nanoparticles.[91] Capsules were treated with AMF and broke due to the heat generation of iron oxide nanoparticles in multilayers generating cargo molecules. In Summary, PEs have versatility for both surface modification materials or microcapsules and showed great performance in vitro studies and further biomedical applications.

1.5. Cytotoxicity Assay

Cell is the smallest living creature having basic structure and functional unit, which indicates that understanding cells is a rudiment of biomedical investigation. Since early 20th century, cell culture as a versatile strategy has been developed as a studying approach in order to exam the cellular behaviors in a controlled environment.[92] Due to the homogeneity and associated reproducibility, it is reliable to introduce cell lines in scientific research.[93] Properties and behaviors between cancer cells and drugs are the key for cancerous investigations. Particularly, cytotoxicity assays, measuring the cytotoxic compounds to lead health or dead cell, are broadly applied in in vitro toxicological and pharmacological studies.[94] It is a critical ending point for the evaluation of drug effects and further in vivo research.

Most cytotoxicity assays follow the difference of principle between live and dead cells, from which fluorescent distinction is commonly applied. Moreover, fluorescent molecules targeting different staining are usually introduced into cell culture. For example, SYTO deep red and coumarin possess cellular (cell membrane) permeability and only stain the nuclei and cytoplasm of live cells, respectively. In the opposite way, due to the selective permeability of live cells, some membrane-impermeant fluorescent molecules like trypan blue can label the dead cells. Considering the application of drug delivery in cell culture, it is often to load cargos with representative cellular staining molecules and observe fluorescence pattern before and after external stimuli as triggers. Following this, tracking fluorescence patterns can indicate if and how the drug delivery system exhibit toxicity to cells.

In general, two-dimensional (2D) cell culture is a widely applied in vitro approach for cytotoxicity, which demonstrates cells attachment and growth as a monolayer at the plastic surface of a flat flask or petri dish in 37°C , the average temperature of human body.[95] Although 2D cell culture are not able to simulate the natural structure of tumors or tissues, it still offers simple and low-cost maintenance and demonstration of functional investigation, which is why it has been the major type of cell culture technique in numerous field.[94]
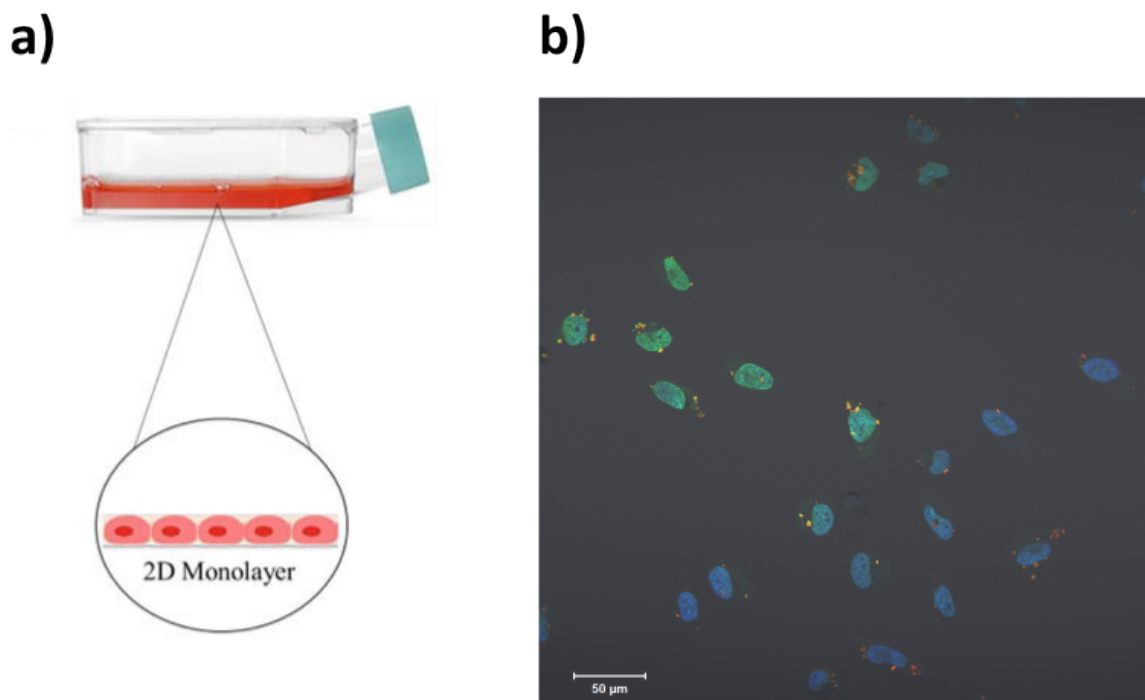
Figure 13: a) Schematic illustration of 2D cell culture. Cited from S. *Ballav et al.*[94]; b) representative image of HeLa cells with HOECHST 33342 nucleus staining.

1.6. Two-photon Laser Scanning Microscopy (2PLSM)

Since 1845, the first observation of fluorescence has been reported by Fredrick W. Herschel, who recognized that a transparent quinine solution is able to be excited from sunlight (UV light) and exhibit blue light emission.[96, 97] In 1852, George Stokes reported

this phenomenon followed by the process: An electron orbiting an atom can absorb the light and go to the excited state. The electron cannot last in excited state for long time and thus go back to the normal state, which exhibits the fluorescence, demonstrated in Figure 14.[98] In principle, light emitted from an indicator usually has a longer wavelength than that of the absorbed light (excitation) due to the energy loss in this process. In general, each photon absorbed leads to a photon release with lower energy. However, it is possible for indicator to absorb the energy from 2 or even more photons causing single photon emission. Particularly, as shown in Figure 14, the energy of each excited "multiphoton" is lower than the emitted photon (in Figure 14, $h\nu_{A1}=h\nu_{A2} < h\nu_B$). Therefore, it is possible to apply light with lower energy for higher energy light emission, for example, red light can be used to generate green or blue light.
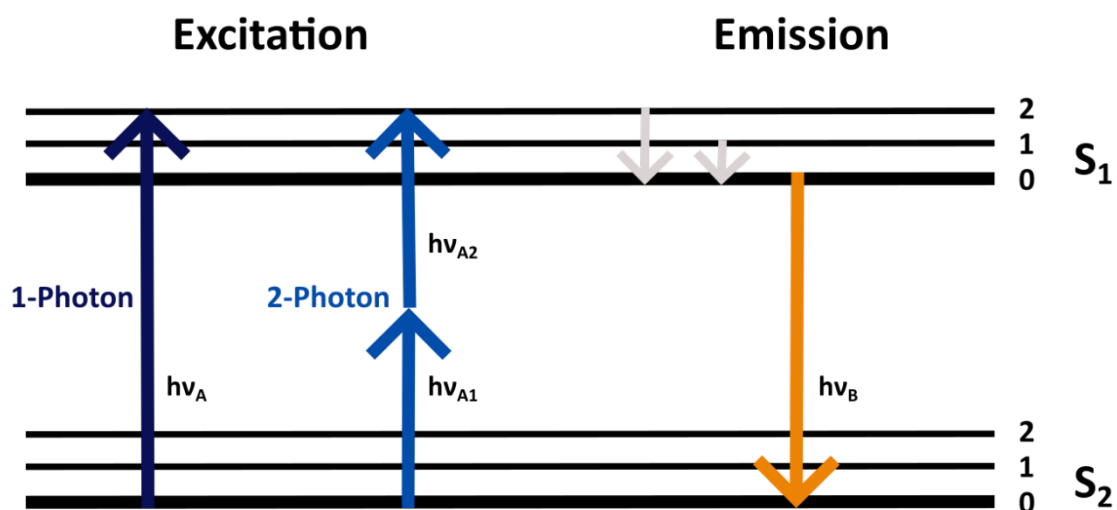
Figure 14:   Jablonski diagram of 1-photon and 2-photon excitation.

With this principle, many microscopic systems have involved laser as a key parameter for fluorescent observation. Optical sectioning via spatial filters, separating the emitted light and excitation light, is an outstanding improvement for microscopic system, from which background signals are able to be reduced and the out-of-focus area can be blurred, named as confocal laser scanning microscopy (CLSM).[99] Furthermore, the application of multiphoton excitation in microscopic system allows light with lower energy to generate

light with higher energy and overcomes the unidirectionality of light (energy) conversion, called two photon laser scanning microscopy (2PLSM).

Because of the advantages, including reduction of out-of-focus photobleaching, less autofluorescence, deeper tissue penetration and intrinsically high three-dimensional resolution,[100] 2PLSMs have been broadly applied for investigating cell physiology, from which the biological specimen can be imaged by the assembly of multiple fluorescent signals. [101]

Main Project: Magnetothermal Cargo Delivery with Metal-Organic Frameworks (MOFs) in vitro

2.   Motivation

Drug delivery, the transportation of a pharmaceutical compound to the target part for therapeutic treatment, is still being investigated. It is ideal to provide drug vehicles with high stability, biocompatibility and trigger controllability, which leads to an efficient therapeutic effect. Considering cancer, one of the most threatening diseases and the second cause of death worldwide, it is meaningful to build a drug cargo system that they can be stable in cancer-cellular atmosphere and controllable for activation of drug release. Furthermore, it is promising to apply magnetic field as a trigger to release drugs due to the outstanding penetration of magnetic field to human tissue and body, and almost non-toxicity of human body exposure with magnetic field with current up to 4.0 Tesla (3183.1 kA/m).[102] Therefore, it is promising to construct a nano-cargo triggered with alternating magnetic field (AMF) and applied for drug release in cell culture.

Herein, the nano cargo system Zn-IONPs@ZIF-8@PMA-DDA-TAMRA@PEs loaded with fluorescent molecules coumarin has been designed, from which Zn-IONPs have ability for regional heat generation responding to AMF and ZIF-8 structure provide the platform for drug loading. Subsequently, PMA-DDA-TAMRA is a fluorescent polymer covering the surface of ZIF-8 shell in order to localize the nanoparticles during cell-cultural observation. Thereupon, Zn-IONPs@ZIF-8@PMA-DDA-TAMRA were dispersed in saturated coumarin in water solution for drug loading. Also, the introduction of PEs (PAH and PSS) is to stabilize the nano cargo and reduce drug leakage before triggering. For in vitro studying, the nano cargo was uptaken from Hela cells, which need to be incubated in 37°C for 24 h afterwards. Following this, Hela cells with uptaken nano-cargo Zn-IONPs@ZIF-8@PMA-DDA-TAMRA(Coumarin)@PEs were treated with alternating magnetic fields for 1 h tracking the release stands via two-photon spectroscopy.

Synthesis and characteristics of Zn-IONPs were the first assignments for investigation. Zn-IONPs as a magnetic material are the media between magnetic field and nano cargo system. Thus. It is required to find out the particles with significant magnetic performance

in alternating magnetic fields. Zn-IONPs initiate regional heat with the external alternating magnetic fields and the generated thermal energy was applied to interact the other parts of the cargo.

In addition, the stability of Zn-IONPs in water solution is a critical point that the separation of Zn-IONPs in water solution affects the ZIF-8 growing and aggregation of particles Zn-IONPs@ZIF-8 should be avoided. The Zn-IONPs production was followed by organic-based synthesis and oleic acid ligands at particle surface need to be exchanged with another hydrophile one. According to the trial of surface modification with various ligands, it is confirmed that Zn-IONPs modified with citric acid brought out the water-stable system offering the spherical ZIF-8 growth with multiple Zn-IONPs, characterized with microscopies SEM and TEM.

Besides, it is necessary to functionalize the particles with fluorescence in order to localize the cargos in cell culture contrasting the releasing guest drug or dye. Thus, a kind of stable fluorescent molecules/structures binding with particles is desirable. For this, the fluorescent structure TAMRA bound with PMA-DDA was introduced to cover the surface of Zn-IONPs@ZIF-8. In order to differ the observation of particles and drug staining, there should be fluorescent gap between TAMRA and guest drug, which means the emissions of TAMRA and drug should not be overlapped. Considering the peaks of excitation and emission from TAMRA structure at 552 nm and 578 nm respectively, coumarin with 443 nm excitation and less than 500 nm emission is one of the proper choices as a guest drug presenting the process of release.

Another concerning issue is the leakage of guest drug from Zn-IONPs@ZIF-8@PMA-DDA-TAMRA. Thus, there should be further surface modification of particles. Zn-IONPs@ZIF-8@PMA-DDA-TAMRA show negative surface charges, by which the introduction of PEs is a strategy that the particles can be covered with multilayered structure based on electrostatic interaction. A further concern came out if there is a certain PEs-structure to stabilized the cargo avoiding leakage and responsive with alternating magnetic fields processing release.

Drug cargos in cell cultural studying rise up other concerns related to biocompatibility. One of the critical issues brought out that too strong heat generation from magnetic particles may cause hyperthermia, which has cytotoxicity. Thus, it is important to find out

the junction point that the cargo can generate certain regional heat to activate release and avoid hyperthermia at the same time.
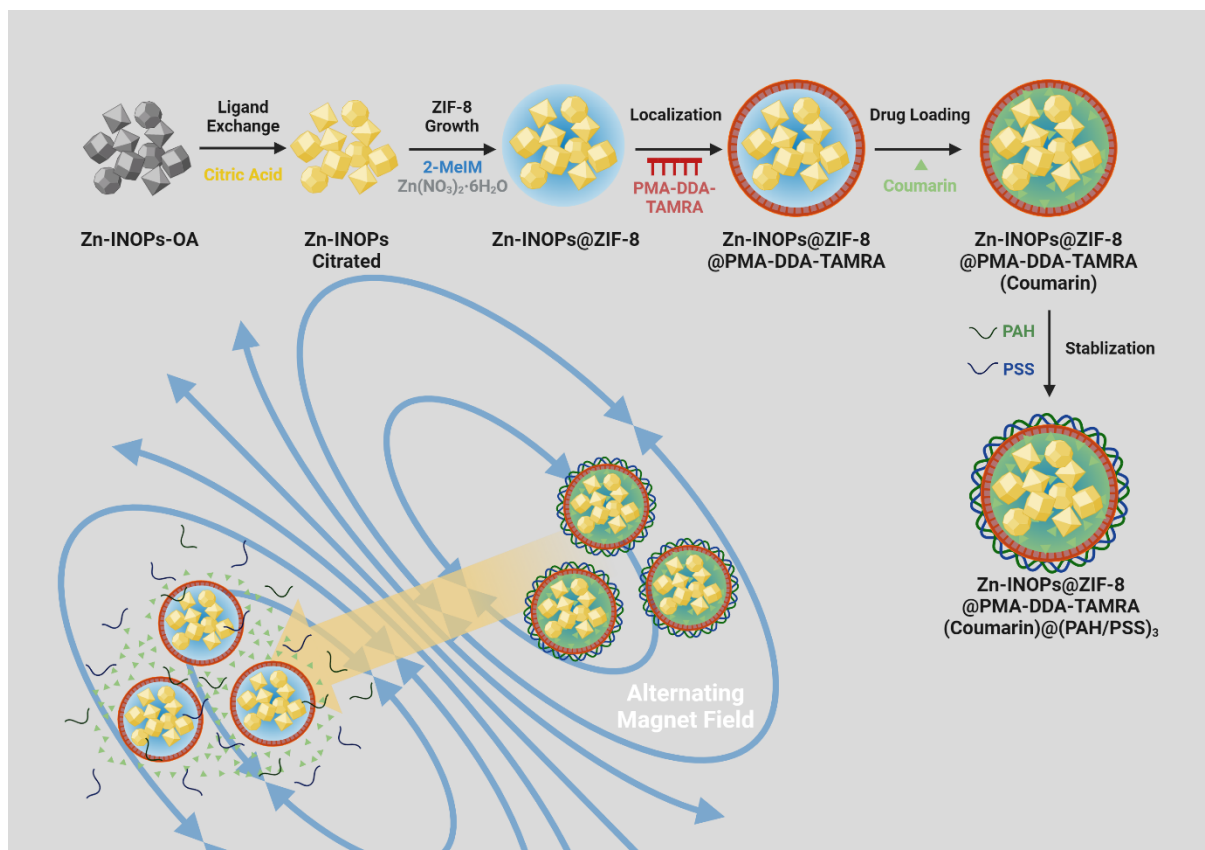
Figure 15: Fabrication of nanoparticle synthesis Zn-IONPs@ZIF-8@PMA-DDA-TAMRA/(PAH/PSS)$_3$ with coumarin loading and treatment with AMF.

3. Materials, Synthesis and Methods

3.1. Materials

Name	CAS	Company	Comments
Iron(III) acetylacetonate	#8.03912	Sigma-Aldrich	
Zinc(II) acetylacetonate	#8.08803	Sigma-Aldrich	
Oleic Acid	#O1008	Sigma-Aldrich	
1-Octadecene	#8.22112	Sigma-Aldrich	
Dibenzyl Ether	#33630	Sigma-Aldrich	

1-Tetradecene	#87189	Sigma-Aldrich	
Citric Acid	#220345 000	Acros Organics	99.5%
Zinc Nitrate Hexahydrate $(Zn(NO_3)_2 \bullet 6H_2O)$	#228737	Sigma-Aldrich	98%
2-Methylimidazole (2-MeIM)	#M50850	Sigma-Aldrich	
Poly(isobutylene-alt-maleic anhydride) (PMA)	#531278	Sigma-Aldrich	$M_w \sim 6000$
Dodecylamine (DDA)	#8.03527	Sigma-Aldrich	
Tetramethylrhodamine (TAMRA)	#271C0	Lumiprobe	5-isomer
Coumarin 343	#393029	Sigma-Aldrich	
Poly(sodium-4-styrene sulfonate) (PSS)	#243051	Sigma-Aldrich	
Poly(allylamine) Hydrochloride (PAH)	#283215	Sigma-Aldrich	$M_w \sim 17{,}500$
Chloroform	#Y015.2	Carl Roth	
Chlorobenzene	#KK01.3	Carl Roth	
N,N-dimethylformamide (DMF)	#6251.1	Carl Roth	
Triethylamine (TEA)	#8.08352	Sigma-Aldrich	
Tetrahydrofuran (THF)	#6788.1	Carl Roth	
Methanol (MeOH)	#8.22283	Supelco EMPLURA®	
Sodium Hydroxide (NaOH)	#6771.1	Carl Roth	
SYTO™ Deep Red	#S34900	Invitrogen™	Nucleic acid staining for live cells
Dulbecco's Modified Eagles Medium (DMEM)		ThermoFisher	
Phosphate-Buffered Saline (PBS)		Invitrogen	
Fetal Bovine Serum (FBS)		Biochrom	

Penicillin-Streptomycin (P/S)		ThermoFisher	
Trypsin-EDTA 0.05%		ThermoFisher	

3.2. Key Instruments

Name	Model	Company	Function
Transmission Electron Microscopy (TEM)	JEM- 1400PLUS	JEOL	NPs Geometry Visualization
Scanning Electron Microscopy (SEM)	SIGMA Gemini	ZEISS	NPs Morphology Visualization
Inductively Coupled Plasma Mass Spectrometry (ICP-MS)	7700 Series	Agilent	Concentration Control
Laser Scanning Microscope (LSM)	LSM 980 mit Airyscan 2	ZEISS	Drug Release in Cell Culture
Alternating Magnetic Field (AMF)	D5 Series	nanoscale Biomagnetics	Treatment of Drug Release
Infrared (IR) Camera	Xi 400	Optris	Temperature Distribution
UV–vis Absorption Spectrophotometer	Agilent 8453	Agilent	NPs Characterization
Fluorescence Spectrometer (FL-spectra)	Cary Eclipse	Agilent	NPs Characterization
Dynamic Light Scattering (DLS)	NANO ZS	Malvern	NPs Characterization

3.3. Synthesis and Modifications

3.3.1. Synthesis of Zn-IONPs with Oleic Acid Ligands

The synthesis of Zn-IONPs with oleic acid (OA) ligands is based on the reference from the work by *S. H. Noh et al.*[37] According to the protocol, Iron(III) acetylacetonate (0.4237 g; 1.2 mmol), zinc(II) acetylacetonate (0.4728 g; 1.8 mmol), and oleic acid (1.423 g; 5 mmol) were added to a mixture of 1-octadecene (7.89 g; 10 mL), dibenzyl ether (10.42 g; 10 mL),

and 1-tetradecene (2.31 g; 3 mL). The mixture was heated to 90 °C at a rate and kept at this temperature in vacuum (~3 × 10^{-2} mbar) for 60 min under vigorous magnetic stirring. Afterwards, the slurry was heated up to the reflux temperature (approximately 294 °C) at a rate of 17 °C/min (13 min in total) under nitrogen flow and kept at this temperature for 30 min. Subsequently, the reaction was cooled down to room temperature. Finally, the mixture was collected and condensed with acetone before centrifugation with speed 7000 rpm for 5 min. After washing with 20 ml acetone twice and centrifugation 7000 rpm for 5 min, was dispersed in 10 ml chloroform.

3.3.2.   Ligand Exchange of Zn-IONPs with Citric Acid

Particles were modified with sodium citrate for optimization of hydrophilicity, which is referred from *K. Davis et al.*[103] Zn-IONPs (12 mg) in chloroform was taken and redispersed in solvent (15 mL) mixed from chlorobenzene and dimethylformamide (DMF) with proportion 1:1. Then, after adding citric acid (10 mg), the mixture was agitated in 100°C for 18 h. Afterwards, the mixture was precipitated with diethyl ether and the product was collected by magnet. After washing twice with acetone and magnet collection, the particles were redispersed in 1 mL H$_2$O.

3.3.3.   Coating of Citrate-Zn-IONPs@ZIF-8

In order to provide the platform drug loading, ZIF-8 were ought to grow around the Zn-IONPs and the strategy is referred from *C. Carrillo-Carrión et al.*[104] Particles in H2O (2.4 mg; 200uL) are taken. After adding Zn(NO$_3$)$_2$•6H$_2$O (19.2 mg; 1mL), mixture was stirred for 5 min. Subsequently, 2-methylimidazole (2-MeIM; 190 mg; 1 mL) was added into the mixture and stirred for 15 min. Afterwards, the product was first centrifuged with speed 7000 rpm for 5min. Then, particles were washed twice with 5 mL methanol and collected by magnet in order to separate ZIF-8 without magnetic particles. Finally, particles were redispersed in 1 mL methanol.

3.3.4. Synthesis of Polymer PMA-DDA-TAMRA

Synthesis of polymer was based on work from *C. A. J Lin et al.*[105] Poly(isobutylene-alt-maleic anhydride) (PMA; Mw~6000) 10.22 mM unit (Mw 154 g/mol; 1.574g) and 30 mL DMF was added into a 100 three neck flask. The mixture was sonicated until it is not opaque anymore. Then, dodecylamine (DDA; 7.668 mM; 1.422 g; Mw: 185.35 g/mol; 75% molar ratio of PMA unit), TAMRA-amine (0.256 mM; 2.5% molar ratio of PMA unit) and 2.5 mL triethylamine (TEA) were added and the mixture was sonicated for a few seconds. It is recommended to add some tetrahydrofuran (THF) to solubilize DDA if the mixture cannot be dissolved in DMF.

The mixture was heated to 70°C in darkness overnight. The color of solution was from light-red in the beginning to orange-red at the end.

Later on, the solvent of mixture was removed by contribution of rotary evaporator with rotation 100 rpm, temperature 75°C and maximum vacuum. Following this, 25 mL chloroform was added to dissolve the polymer and the whole solvent was removed again via rotary evaporator.

Finally, 20.44 mL chloroform was added to polymer in order to get 0.5 M stock solution.
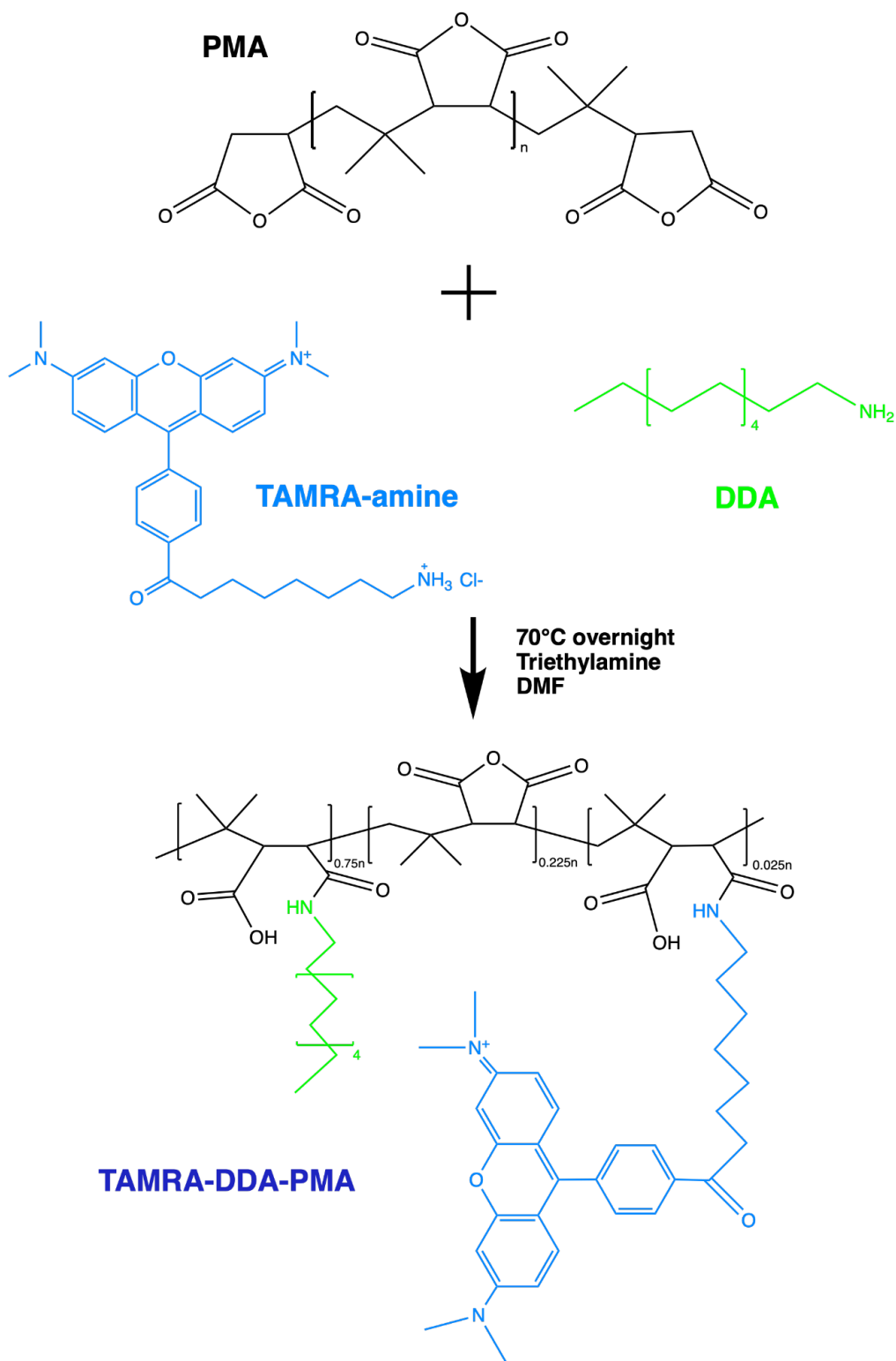
Figure 16: Schematic demonstration of the synthesis PMA-DDA-TAMRA.

3.3.5. Binding of Zn-IONPs@ZIF-8 with PMA-DDA-TAMRA

For localization of particles, polymer PMA-DDA-TAMRA was involved for modification. Referred from the work from *J. Hühn et al.*,[106] PMA-DDA-TAMRA stock solution (0.5 mL; 0.5 M) was diluted with 2.5 mL chloroform. Then, particles Zn-IONPs@ZIF-8 in 1mL methanol was added and mixed. Subsequently, the solvent was removed gently by rotary evaporator with rotation 100 rpm, temperature 30°C and vacuum 300 mbr. Afterwards, 4 mL chloroform was added to the product again for dissolving and removed again via rotary evaporator with rotation 100 rpm, temperature 30°C and maximum vacuum.

Following above, 10 mL NaOH aq was added and the mixture was sonicated for hydrophilization. Product was twice washed with MillQ-water, collected by magnet and finally redispersed in 1 mL methanol for next step.

3.3.6. Drug Loading (Coumarin)

Based on previous step, solvent of the nanoparticles was discarded and coumarin in methanol in saturated concentration (1mL; 2 mg/mL) was added. The system was incubated overnight afterwards. Finally, product was twice washed with MillQ-water, collected with magnet and redispersed in 1 mL H_2O.

3.3.7. Layer-by-Layer with Polyelectrolytes (PAH/PSS)

To reduce the drug leackage, polymer PSS (2 mg/mL in 0.5 M NaCl aq; pH≥7) and PAH (2 mg/mL in 0.5 M NaCl aq; pH≥7) were involved for constructing layer-by-layer (LbL) structure. Hereby, the polymer layer structure PAH/PSS was referred from the work by *S. Carregal-Romero et al.*[91] First, 1mL particles $Fe_{2.6}Zn_{0.4}O_4$@ZIF-8/PMA-DDA-TAMRA was taken. As the surface of particles is negatively charged, 1 mL polymer PAH was added. The mixture was then sonicated for 2 min and shaking for 12 min. Afterwards, solvent was discarded. Product was washed with MillQ-water twice and redispersed in 1 mL H_2O. Following this, 1 mL PSS was added and the mixture was treated with the same procedure as PAH. If a pair of PAH-layer and PSS-layer is considered as one set, three sets were constructed in the end and the product was finally redispersed in 1 mL H_2O.

3.3.8.   Cell Culture

HeLa (cervical cancer cell line) were cultured in Dulbecco's Modified Eagle Medium with phenol red, 4.5 g/L D-glucose, L-glutamine and pyruvate (DMEM, 1X, Gibco, #41966-029) supplemented with 10% Fetal Bovine Serum (Gibco, #10270-106) and 1% Penicillin Streptomycin (P/S, Corning, 100X, #30-002-CI). Cells were maintained under humid conditions at 37 °C and 5% of CO_2.

In order to perform 2-photon images with living cells, Hela Cells with amount 50×10^3 in1 mL cell culture medium were seeded on 35 mm low µ-Dish with 500 grids (Ibidi, Germany, #80156) for 24 h before up-taking particles again 24h incubation.

3.3.9.   Two-Photon Imaging

All 2-Photon images were acquired by LSM 980 mit Airyscan 2 with objective 20x and processed with ZEN Microscopy Software. Applied ex./em. wavelengths for 2-photon images were followed:

- 458 nm/470-500 nm: Coumarin as up-taken drug (green)
- 561 nm/570-600 nm: TAMRA-labeled nanoparticles (blue)
- 633 nm/670-700 nm: Invitrogen™ SYTO™ Deep Red for nucleus staining (red)

Images were taken from the beginning and after each 10 min AMF treatment until 60 min. Cell dish was placed at the center of the planar coil PC70 from D5 Serie by nanoScale Biomagnetic. Program of software from D5 was set as experiment mode with frequency 300 kHz and current 15.2 kA/m or 24.4 kA/m for 10 min.

3.3.10.   IR Camera / Heating Map

Heating maps were acquired by applying Optris Xi 400 infrared camera equipped with an 18° x 14° spectral range lens. The camera features a focal plane array (FPA) detector with a frame rate of 80 Hz and a resolution of 382 x 288 pixels. It can detect infrared radiation within the spectral range between 8 µm and 14 µm. The emitted infrared radiation from the sample was processed utilizing the corresponding PIX software, which rendered the data as temperature-related colored structures. Areas with lower temperatures were

represented in dark color (blue or black), while regions with higher temperatures exhibited bright yellow or orange hues. The system was capable of resolving temperature differences of 0.1 °C or greater. During a typical measurement, the sample was positioned within a 34 mm × 34 mm ibidi dish and tracked from above, with the distance between the camera and the sample maintained at approximately 15 cm.

4. Results

4.1. Synthesis of Zn-IONPs

The synthesis of magnetic particles was guided from the literatures that size of particles determines the magnetic thermal behavior. Particles with bigger size demonstrated ferromagnetism via hysteresis loss. In contrast, particles with smaller size follow in general superparamagnetism depending on Néel and Brown relaxations..[107] Both magnetic behaviors are able to offer the heating generation. The first aim is thus finding out if magnetic particles possess adequate heat generation responded from alternating magnetic field (AMF) for further applications. Following the protocols, nanoparticles Zn-IONPs were reproduced and determined via transmission electron spectroscopy (TEM). According to Figure 17, all the sizes of Zn-IONPs were between 20 - 23 nm with shape more likely tetradecahedron or truncated cubic. Besides, based on the statistic, size distributions demonstrated the homogeneity, which are almost the same in all syntheses. Therefore, it is confirmed that homogeneous Zn-IONPs with size around 20 nm can be synthesized and reproducible.
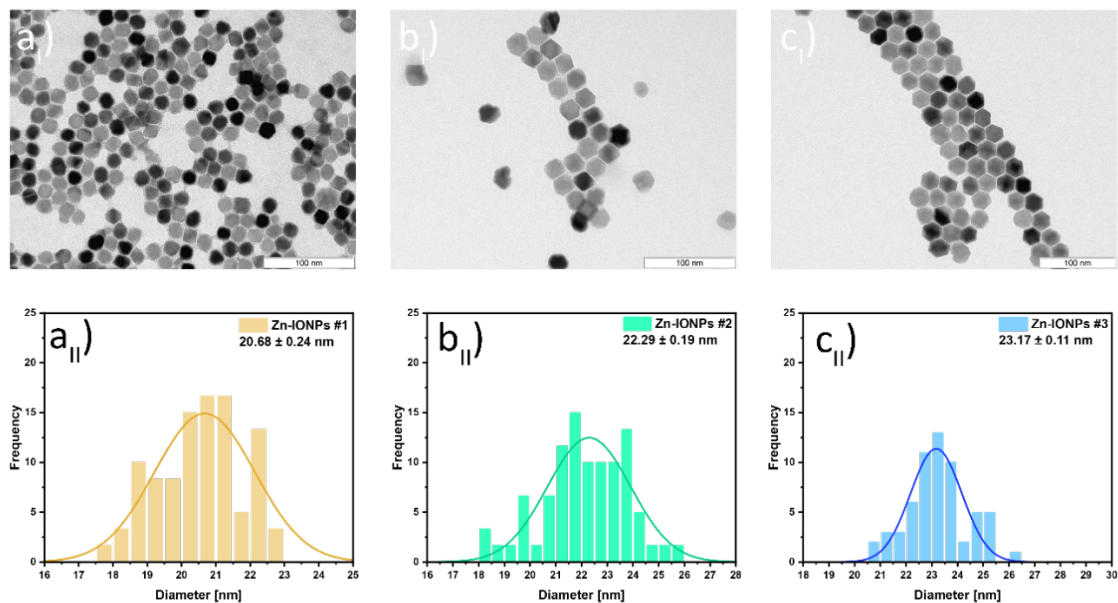
Figure 17: Representative TEM images (I) and size distributions (II) of Zn-IONPs: a) NPs #1; b) NPs #2; c) NPs #3. Determined from the TEM, the sizes are respectively: a) d=20.68 ± 0.24 nm, b) d=22.29 ± 0.19 nm, c) d=23.17 ± 0.11 nm

4.2. ZIF-8 and Zn-IONPs@ZIF-8

In order to improve the dispersity of Zn-IONPs in water solution for ZIF-8 growing, surface modification with other ligands are necessary. Inspired from the work by *C. Carrillo-Carrión et al.*,[104] hydrophobic nanoparticles Zn-IONPs with OA-ligands were dispersed in surfactant CTAB water solution, from which the geometry of ZIF-8 can be controlled. In practice, however, this strategy showed geometrical inhomogeneity with unpredictable shape and broad size distribution, as shown in Figure 18 c). It is possible that the magnetic interaction leaded to agglomeration easily and the surfactant covered aggregates instead of individual nanoparticles, which leads to inhomogeneous geometry of Zn-IONPs@ZIF-8. In order to overcome this issue, it is considerable to process other ligand exchanges with small molecules. Referred from work by *K. Davis et al.*,[103] citric acid and caffeic acid were considered for modifications. According to Fig. Figure 18 a), more homogeneous spherical Zn-IONPs@ZIF-8 can be achieved and reproduced after modification of Zn-IONPs with citric acid, which is similar to the geometry of pure ZIF-8 particles synthesized with the same protocol. In contrast, shown in Figure 18 b), Zn-IONPs modified with caffeic acid led to strong agglomeration, which may not be satisfying for further application. As comparison, the production of Zn-IONPs@ZIF-8 through modification with citric acid is so far the ideal strategy.
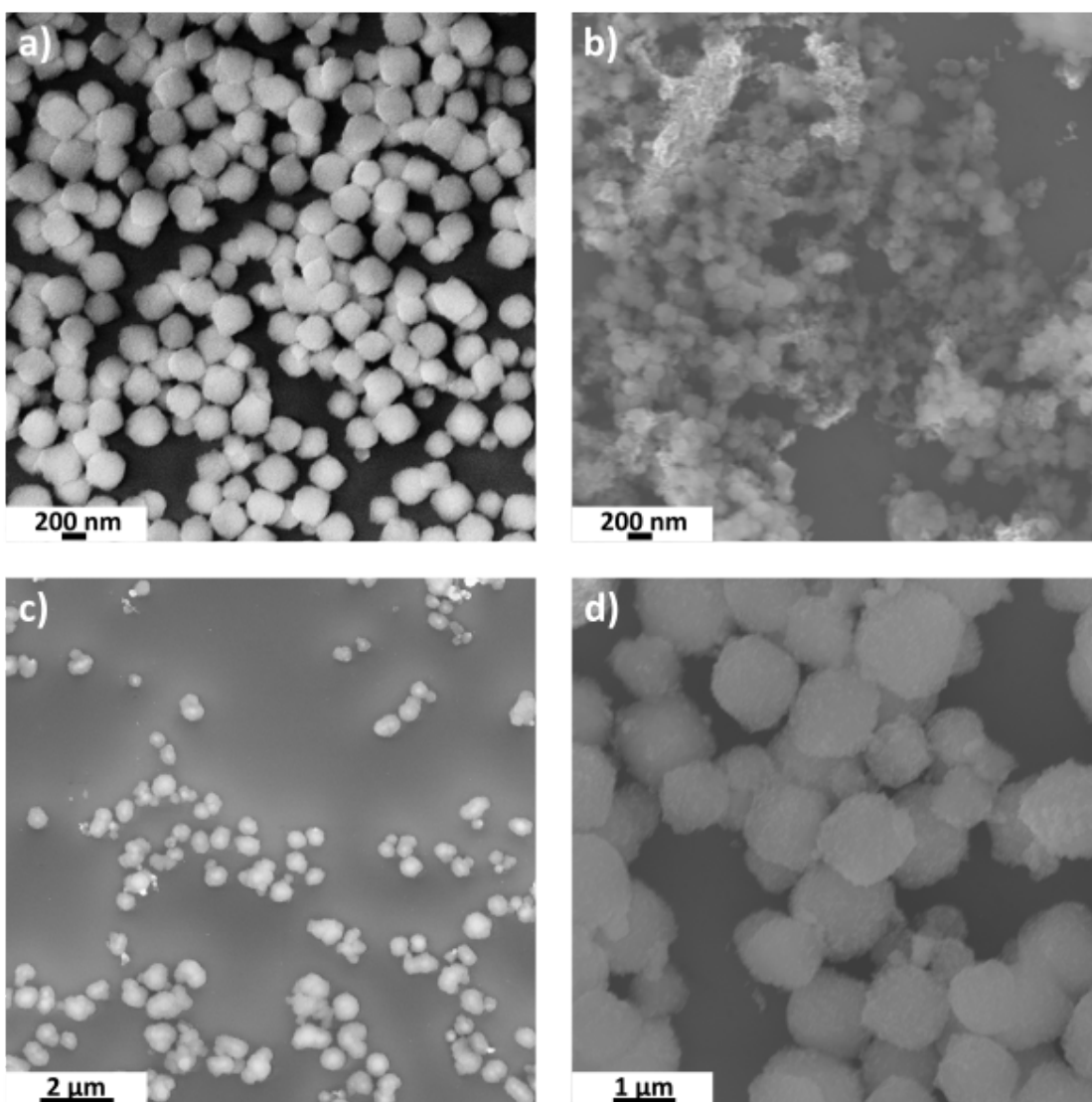
Figure 18: SEM images of a) ZIF-8 particles; b-d) Zn-IONPs@ZIF-8 via various strategies: b) caffeic acid modification before ZIF-8 growing; c) Participation of CTAB during ZIF-8 growing; d) citric acid modification before ZIF-8 growing.

Following this, the structure of nanoparticles Zn-IONPs@ZIF-8 with citric acid strategy and pure ZIF-8 were compared. Even the size, shape and distribution of Zn-IONPs@ZIF-8 and pure ZIF-8 were quite similar, by which the sizes were approximately 657 nm and 574 nm respectively, the difference of the structure can be observed that the Zn-IONPs can even be recognized by Zn-IONPs@ZIF-8 spheres in compare with pure ZIF-8, shown in Figure 19 e) and b) respectively.
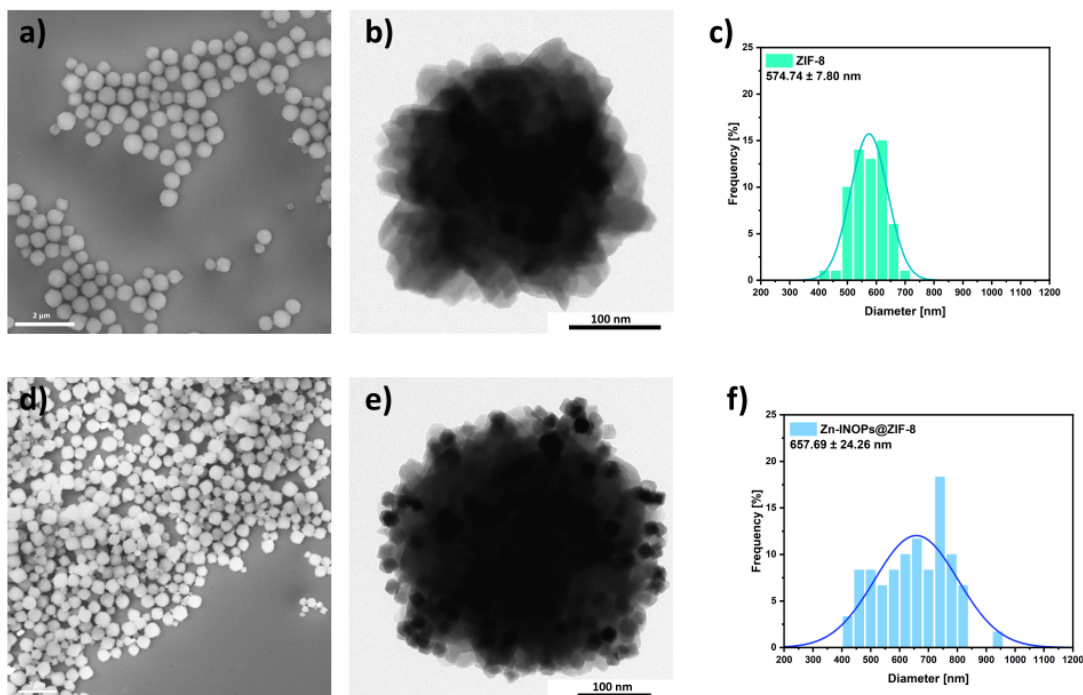
Figure 19: Represevtative SEM images a) and d); TEM images b) and e); size distribution c) and f) in order to show size, shape, distribution of a-c) ZIF-8 and d-f) Zn-IONPs@ZIF-8. Size was determined respectively: ZIF-8, 574.74 ± 7.80nm; Zn-IONPs@ZIF-8, 657.69nm ± 24.26nm.

4.3. Heat Generation (Alternating Magnetic Field)

Alternating magnet field (AMF) was provided from instrument D5 Series by nanoScale Biomagnetics, which is for heat generation and hyperthermia with magnetic trigger. Cooling water bath should be provided during operation. For heating measurement, 1 mL 1 mg/mL particles in water were dispersed in glass vial, which is matched with temperature sensor and calorimetry coil from D5. Vial was inserted into the coil. Frequency and current (300 kHz; 15.2 kA/m, 24.4 kA/m, 36.6 kA/m) were as set and temperature was tracked and recorded for 600 s.

The first heating measurement is 1mL 1 mg/mL Zn-IONPs in water solution with AMF treatment in different conditions, demonstrated in Figure 20. In contrast, an extra sample with only 1 mL water was also measured with 3 AMF conditions. It demonstrated that Zn-

IONPs are able to release heat with AMF. Once the frequency is fixed, higher magnetic currents led to higher temperature induction. In comparison, the temperature of blank sample remained in 20°C, which proves there is little contribution of heating induction by water.
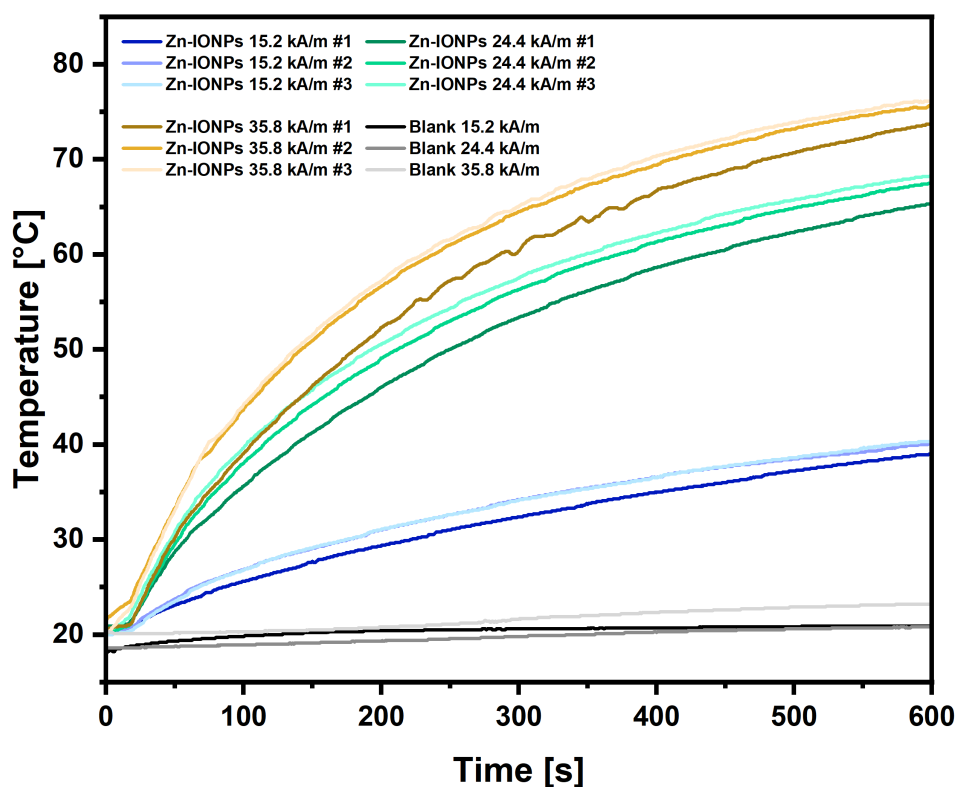

Figure 20: Heat generation of citrate Zn-IONPs in treatment of alternating magnetic field with frequency 303 kHz and current 15.2 kA/m, 24.4 kA/m and 35.8 kA/m. Image demonstrates the reproducibility of heat generation. Blank: 1 mL MilliQ-Water.

For further measurement of heat generation, concentration of nanoparticles in each stand was controlled by the concentration of iron-ions as 1 mg/mL in 1 mL MilliQ-water. Each sample was separated in 1.5 mL vial for AMF treatment. According to Figure 21 a-c), with the same condition of AMF, the temperature rate decreases if more materials are modified for Zn-IONPs. Heat was absorbed from ZIF-8 and polymer. There is temperature peak around 100 s by Zn-IONPs@ZIF-8/LbL structure, which shows breaking time of the

polymer structure, and the rate is the same as Zn-IONPs@ZIF-8 afterwards. Figure 21 d) shows the current affects the efficiency of temperature rate from Zn-IONPs with different modifications. Higher temperature rate with higher current of AMF in all cases are proved. Based on Figure 21 in general, it is interesting that even with the same concentration of Zn-IONPs, more steps of modification weaken the performance of heat generation in AMF and this conclusion is supportive to reduce hyperthermia.
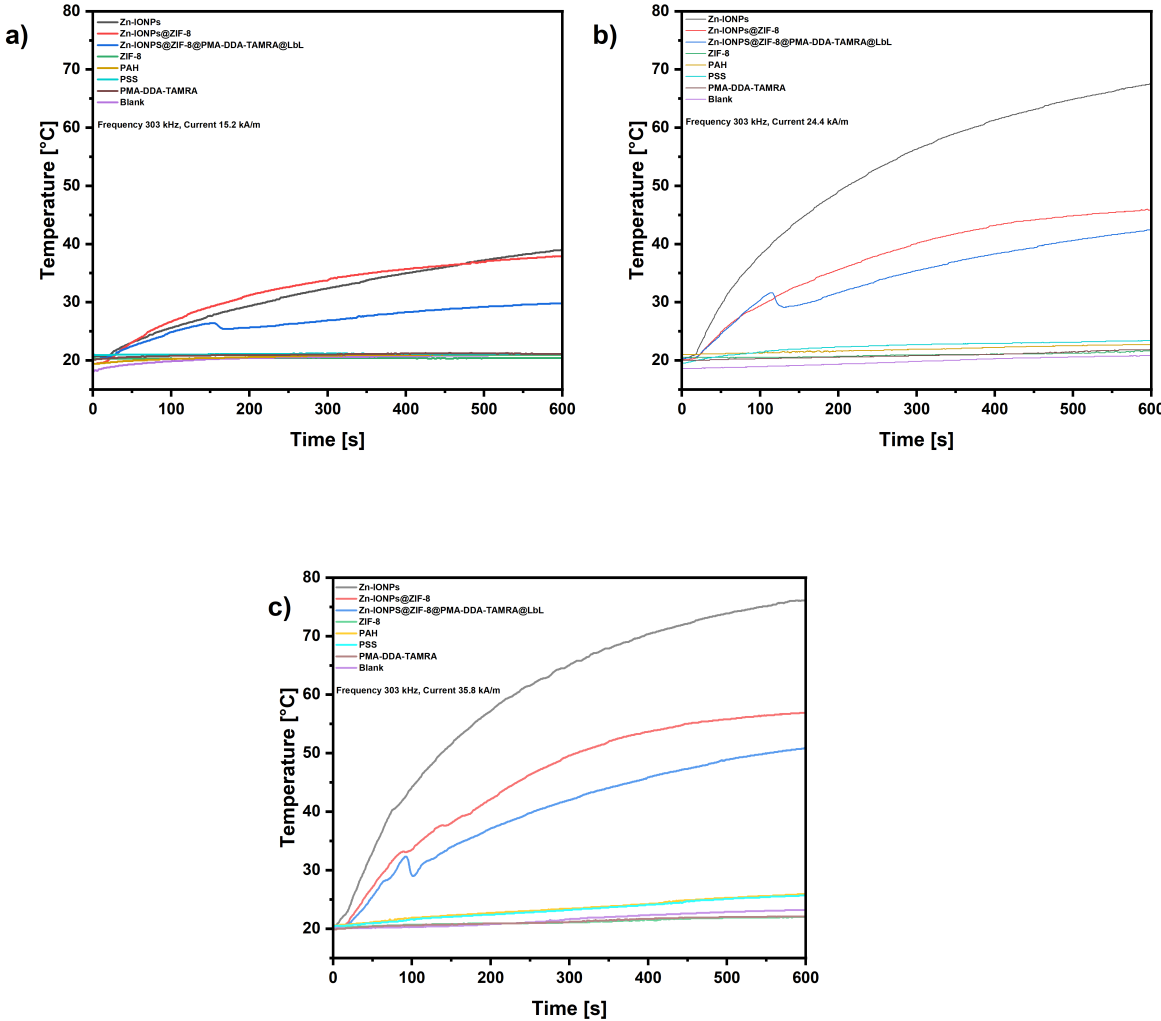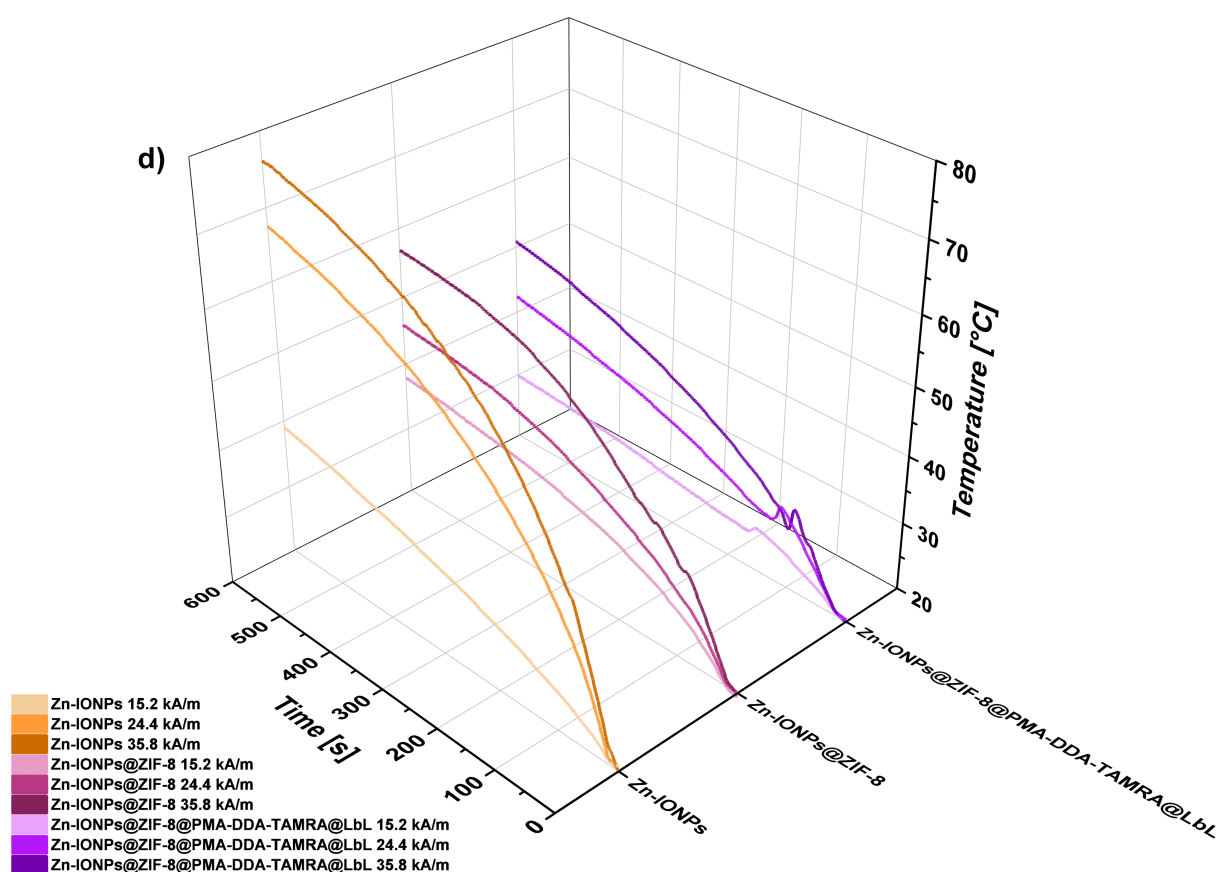
Figure 21: SAR value from Zn-IONPs modified with ZIF-8 and polymer layers in treatment from AMF with various conditions: a) current: 15.2 kA/m, frequency: 300 kHz; b) current: 24.4 kA/m, frequency: 300 kHz; c) current: 36.6 kA/m, frequency: 300 kHz. d) Summary from a-c) with each stand of modifications from particles.

4.4. Drug Release

4.4.1. Release Rate and Polyelectrolyte Layers

In the context of drug delivery systems, the phenomenon of drug leakage represents a significant challenge that necessitates resolution. During the assessment of drug leakage, it was observed that a fluorescent induction of the supernatant occurred in the absence of treatment, indicating the dispersion of the drug within the supernatant. To investigate this issue, three distinct samples of Zn-IONPs@ZIF-8@PMA-DDA-TAMRA, which were loaded with coumarin, were prepared: two samples underwent alternating magnetic field

(AMF) treatment with varying current, while one served as a blank control. The supernatant of each sample was monitored at multiple time points through fluorescence spectroscopy. The results depicted in Figure illustrate an increasing intensity peak at 492 nm across all conditions, suggesting that drug leakage is prevalent, as evidenced by the linear simulations presented in the same figure, which reveal a similarity in the fluorescence gradient of the supernatant.

To address the challenge posed by drug leakage, polyelectrolytes were employed as a means of optimization. Polyelectrolytes, specifically poly(allylamine hydrochloride) (PAH) and poly(sodium-4-styrene sulfonate) (PSS), which possess positive and negative charges, respectively, were utilized to monitor surface charge alterations as a means of assessing layer assembly. Zeta potential analysis, depicted in Figure, indicated that the Zn-IONPs@ZIF-8@PMA-DDA-TAMRA particles exhibited a negative surface charge. The incorporation of the polyelectrolytes PAH and PSS effectively altered the surface charge to positive and negative, respectively, culminating in a dynamic fluctuation of the overall surface charge. This behavior confirmed the successful construction of a multilayered structure on the surface of Zn-IONPs@ZIF-8@PMA-DDA-TAMRA through the application of these polyelectrolytes.

Subsequently, the fluorescence of coumarin in the supernatant from the Zn-IONPs@ZIF-8@PMA-DDA-TAMRA samples with varying quantities of polyelectrolyte layers was monitored and illustrated in Figure. Notably, both Zn-IONPs@ZIF-8@PMA-DDA-TAMRA@PAH/PSS and Zn-IONPs@ZIF-8@PMA-DDA-TAMRA@(PAH/PSS)$_2$ exhibited a decrease in fluorescence intensity, consistent across both AMF-treated and untreated samples. This observed reduction in fluorescence intensity may be attributed to the thermal dependent solubility of coumarin in water solution.[108]

In contrast, the samples Zn-IONPs@ZIF-8@PMA-DDA-TAMRA@(PAH/PSS)$_3$ displayed divergent patterns, where the fluorescence of coumarin in the supernatant increased specifically under AMF treatment; conversely, the untreated samples maintained a decreasing trend. This finding indicates that the nanoparticles Zn-IONPs@ZIF-8@PMA-DDA-TAMRA@(PAH/PSS)$_3$ possess the capability to mitigate drug leakage, rendering drug release feasible solely in the presence of AMF.
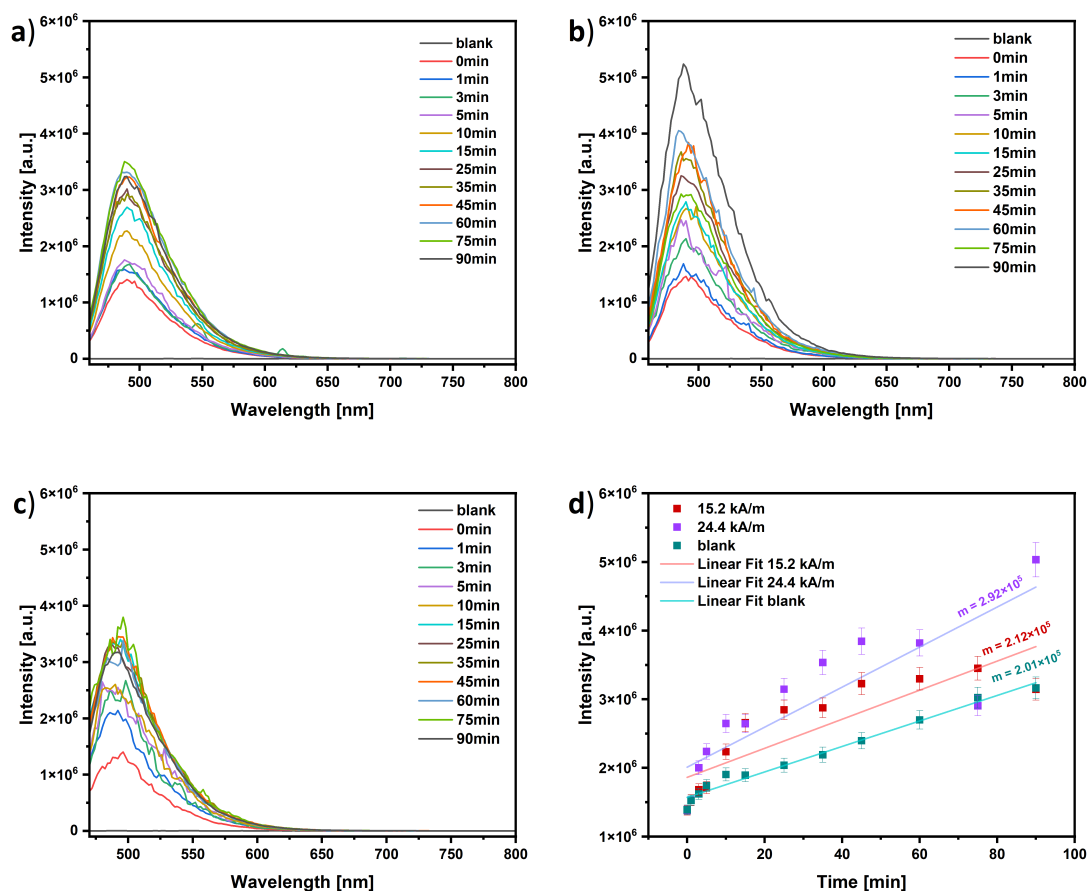
Figure 22: Fluorescence intensity of supernatant from Zn-IONPs@ZIF-8@PMA-DDA-TAMRA (coumarin) with alternating magnet field (AMF) in various condition a) current: 15.2 kA/m, frequency: 300 kHz; b) current 24.4 kA/m, frequency: 300 kHz; c) blank. Intensity peaks at wavelength 492 nm from a-c) are noted, summarized and linear fitted in d).
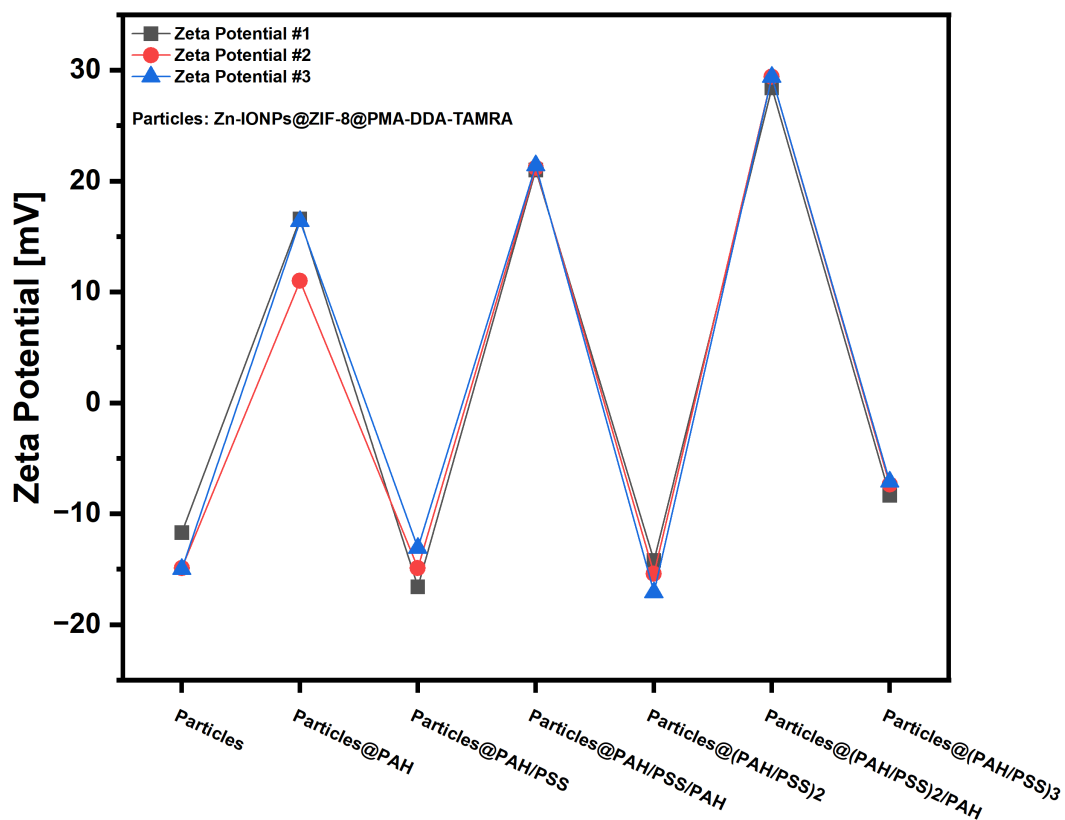
Figure 23: Zeta potential tracking for the process of particles Zn-IONPs@ZIF-8@PMA-DDA-TAMRA modified with polyelectrolytes PAH and PSS, which possess positive and negative charge respectively. Surface charge changed alternatively
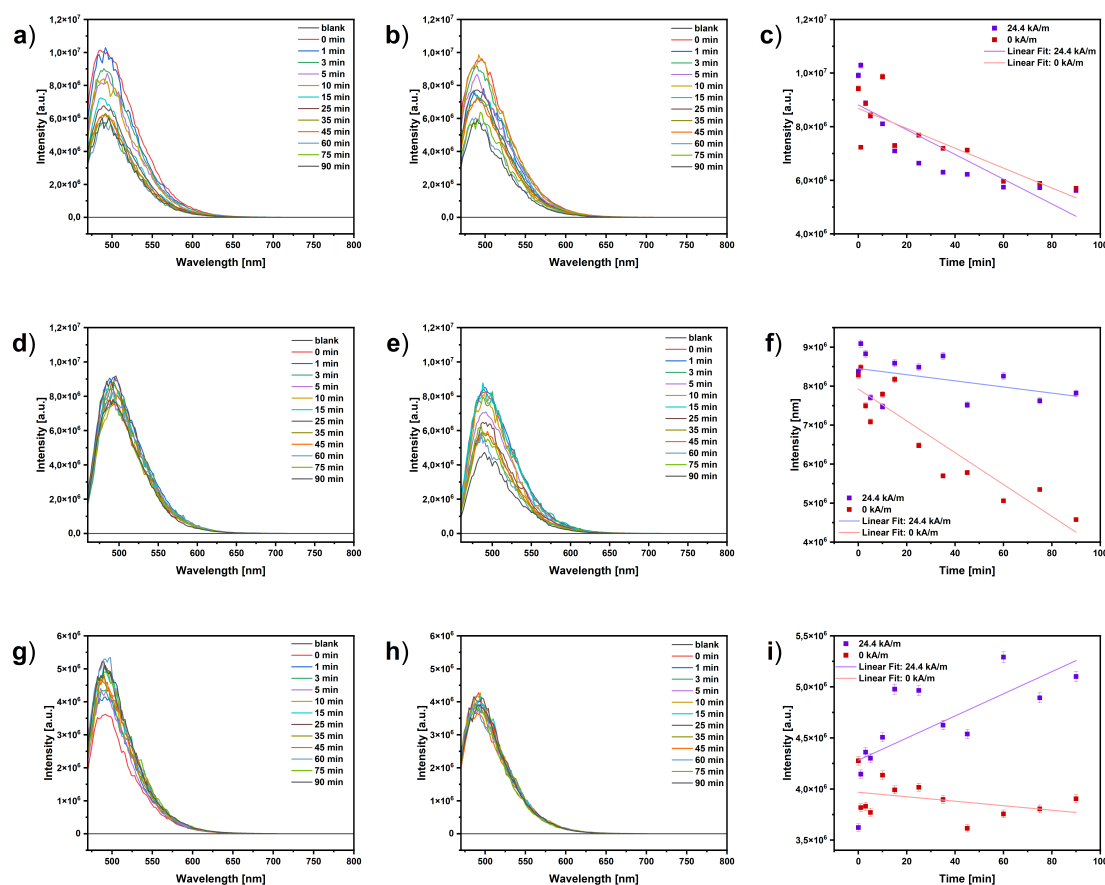
Figure 24: Fluorescence intensity of supernatant from nanoparticles Zn-IONPs@ZIF-8 with various of polymer layers: a-c) particle@PAH/PSS; d-f) particle@(PAH/PSS)$_2$; g-i) particle@(PAH/PSS)$_3$. Here, particle represents Zn-IONPs@ZIF-8@PMA-DDA-TAMRA. For a), d), g) the particles were treated with AMF with current 24.4 kA/m and frequency 300 kHz and for b), e), h) there was no magnetic treatment as blank. The intensity peaks at wavelength 492 nm in each test point were noted, linear fitted and compared as c), f) i).

4.4.2.   Switch On / Off

Since it is confirmed that nanocargo Zn-IONPs@ZIF-8@PMA-DDA-TAMRA@(PAH/PSS)$_3$ provide the promising drug loading stability and trigger-ability with AMF introduction, it is interesting to investigate the release controllability, by which the release can be directed based on AMF participation. Following this, 1mg/mL Zn-IONPs@ZIF-8@PMA-

DDA-TAMRA@(PAH/PSS)$_3$ loaded with coumarin was treated with intermittent AMF in current 24.4 kA/m and frequency 300 kHz, in which each 15 min treatment should follow up 15 min pause as a routine processing 3 times. As shown in Figure 25, it is interesting that fluorescence intensity increased stepwise, which indicated the release process directed by AMF participation. Due to the temperature-sensible solubility of coumarin in water, there is intensity reduce during none treatment period as "cooling time".[108] Fluorescence rate was calculated by the function, in which acidic treatment (10uL 1mg/mL EDTA was added and the sample stood for 90 min) was processed after switch on/off experiment and defined as entire dissolvement, in which fluorescence intensity from coumarin after acidic treatment was maximum:

$$\text{Fluorescence Rate [\%]} = \frac{\text{Fluorescence}_{\text{time point}}}{\text{Fluorescence}_{\text{EDTA}}} \times 100\% \qquad (7)$$
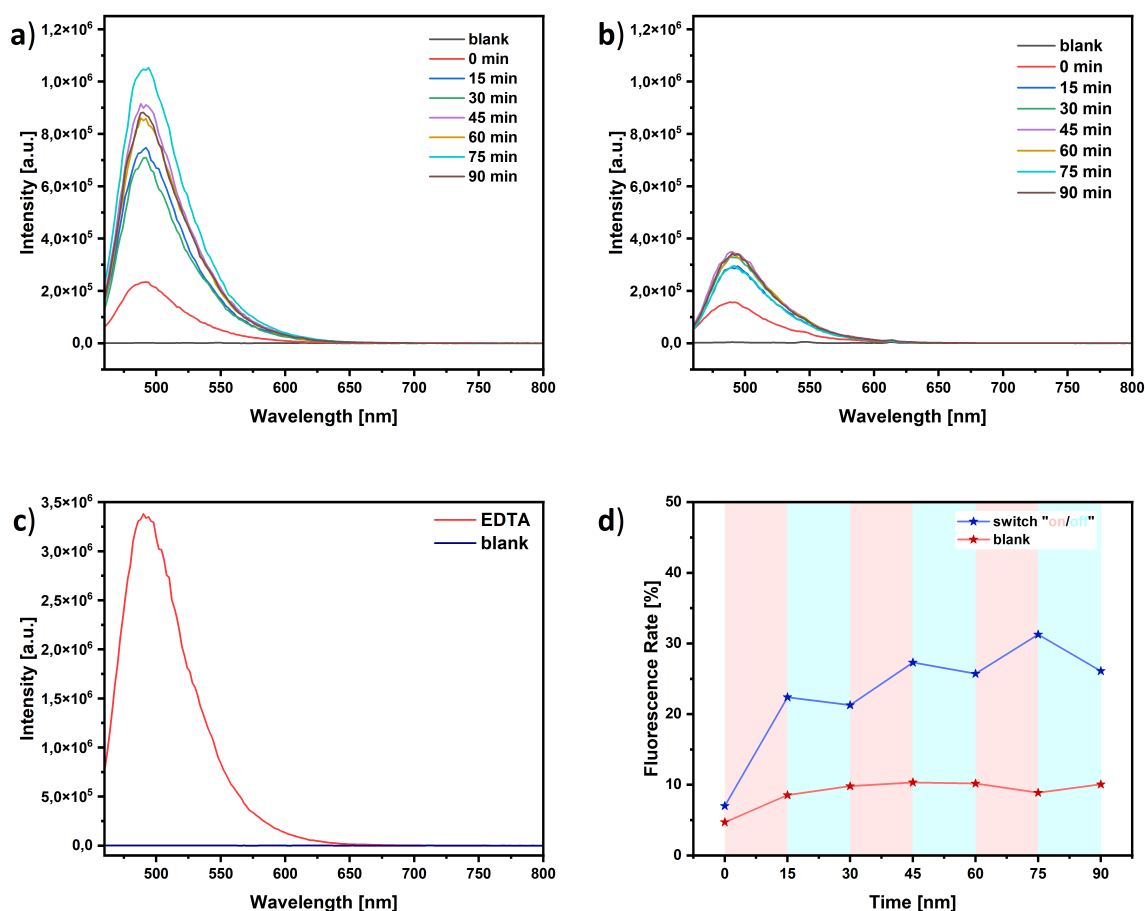
Figure 25: Fluorescence of coumarin release from Zn-IONPs@ZIF-8/(PAH/PSS)$_3$ with a) intermittent AMF treatment with current 24.4 kA/m and frequency 300 kHz; b) no treatment for entire 90 min; c) 1 uL 1 mg/mL EDTA as acid treatment for destroying ZIF-8 in order to show the max capacity of Zn-IONPs@ZIF-8; d) summary of intensity peaks at 492 nm in each test point. Fluorescence rate was calculated with given function.

4.4.3.   Heating Map

Heating map was imaged by Optris Xi 400 infrared (IR) camera and the IR emission was recalculated via PIX Software in order to provide heat distribution with color spectrum. For heating image, 1 mL 1 mg/mL particles in water were dispersed in 35 mm µ-Dish, which was afterwards placed on planar coil PC 70 from D5. After frequency and current setting (300 kHz; 15.2 kA/m, 24.4 kA/m, 36.6 kA/m), images were taken from camera in each minute from the start of AMF treatment until 10 min.

Not only heat generation measurement, temperature distribution of sample has been observed via IR-camera as well. Samples were controlled as 1 mg/mL in 1 mL MilliQ-water but separated homogeniously in a petri dish with Internal Ø=34mm. The observation area of IR-camera is therefore set as 34 mm × 34 mm. According to the Figure 4, temperature increase can be observed in each sample, especially the citrated Zn-IONPs, which shows the most significant difference between the start and the end of AMF treatment. Additionally, this result is in line with Figure 26 and another provement between modification and heating performance, the more modifications of nanoparticles, the less temperature increase.
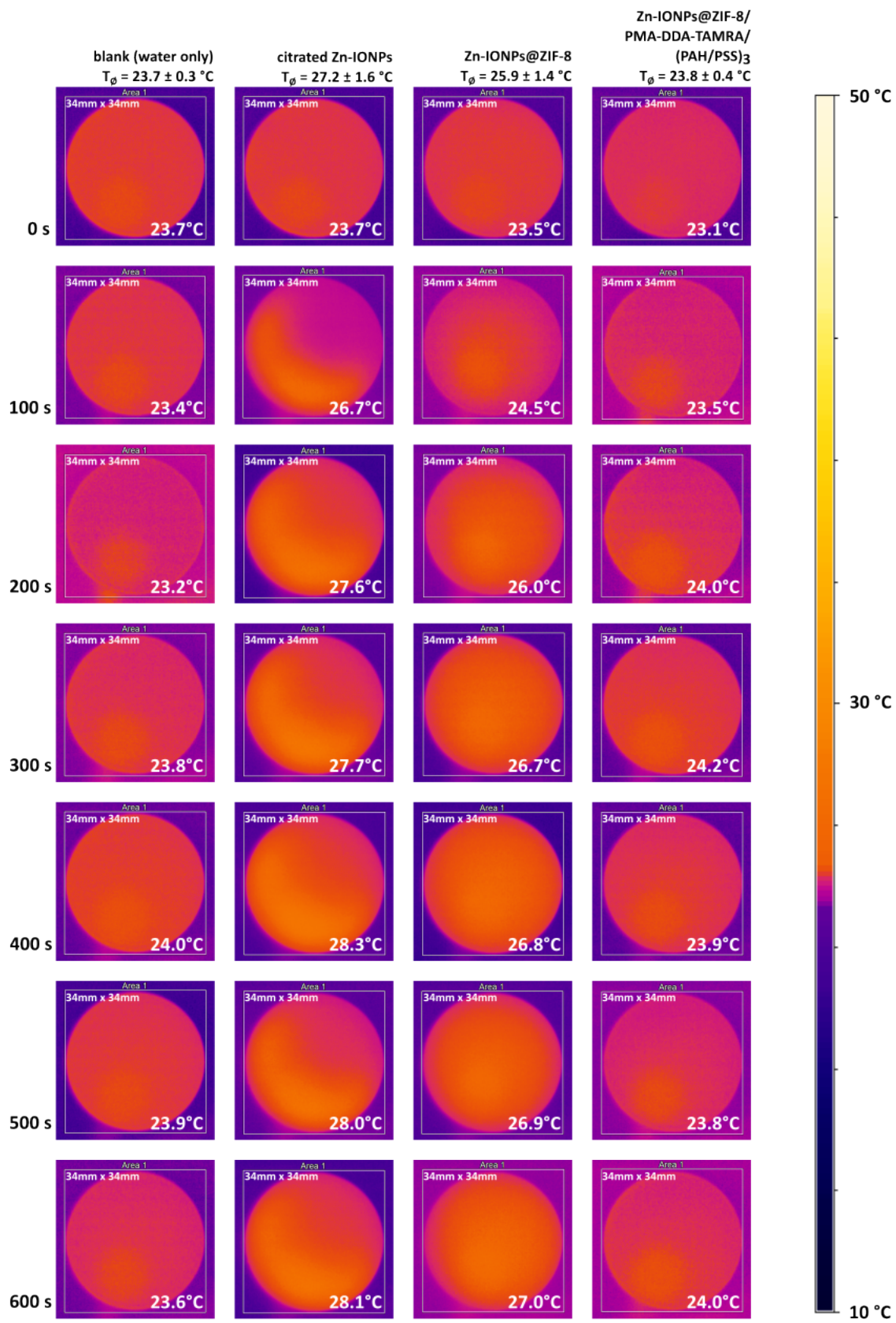
Figure 26: Temperature distribution of nanoparticles in each stand of modifications treated with AMF with current 24.4 kA/m and frequency 300 kHz. All particles were separated in 1 mL MilliQ-water in Ø=34mm petri dish. Observation Area is static and with size 34 mm × 34 mm. Average temperature with difference value from each sample was given respectively.

4.4.4. Two-Photon Imaging

As shown from images of 2-photon spectroscopy, it is clear to see the signal from coumarin (green), TAMRA structure (blue), SYTO deep red (red) and bright field. From Figure 27, fluorescence of coumarin (green) and TAMRA (blue) is in general spot-like and perfectly overlapped, which shows the location of particles. Plus, in Figure 27 a$_v$), plenty of particles were uptaken in alive Hela cells, which proves the successful cell uptake from particles before AMF treatment.

Subsequently, Hela cells with particles are treated with AMF. As shown from Figure 28, overlap from coumarin and TAMRA decreased. In contrast from fluorescence of TAMRA, which were still the same as before AMF treatment, there was gentle diffusion from fluorescence of coumarin but still in cells. This shows the coumarin release. However, due to weak fluorescence diffusion, tracking of cells with particles in AMF and release rate are necessary. In principle, 2-photon images were taken in each 10 min AMF treatment and cells even with weak coumarin staining need to be counted as cells with released drug. In Figure 29, fluorescence of coumarin increased and diffused gently with the gradual process of AMF treatment. Then, staining rate was calculated with followed function:

$$\text{Staining Rate } [\%] = \frac{N_{\text{cells, coumarin diffusion}}}{N_{\text{cells, total}}} \times 100\% \qquad (8)$$

And as shown in Figure 30 a), the trend of staining rate went higher with process of treatment. With stronger AMF treatment, there is around 40% staining rate increase. In contrast, there is around 10% staining rate increase as leakage. Interestingly, in order to neglect drug leakage, staining rate can be optimized as netto staining rate with followed function:

Netto Staining Rate [%]

$$= (\text{Staining Rate}_{\text{with AMF}} - \text{Staining Rate}_{\text{without AMF}}) \qquad (9)$$
$$- (\text{Staining Rate}_{\text{start, with AMF}} - \text{Staining Rate}_{\text{start, without AMF}})$$

According to the result shown in Figure 30 b), there were gradual netto increase between 20%-30% with AMF trigger. Although the final netto staining rate from all cases showed no difference between both AMFs with different currents 15.2 kA/m and 24.4 kA/m, from which all the final rates were random. However, based on results mentioned before, these are key evidences of drug release in cell culture with contribution of triggered AMF treatment.
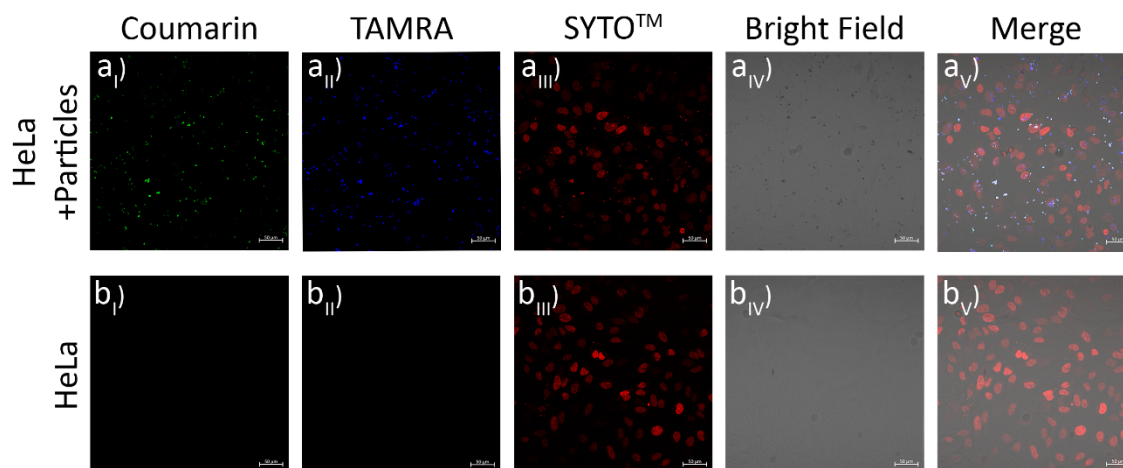

Figure 27: 2-photon images of a) Hela cells with nanoparticles: Zn-IONPs@ZIF-8(coumarin)/(PAH/PSS)$_3$ and b) Hela cells. Each channel represents respectively: I) coumarin (green), II) TAMRA, III) SYTO™ deep red, IV) bright field and V) merge. All images were taken after 24 h incubation and before AMF treatment.
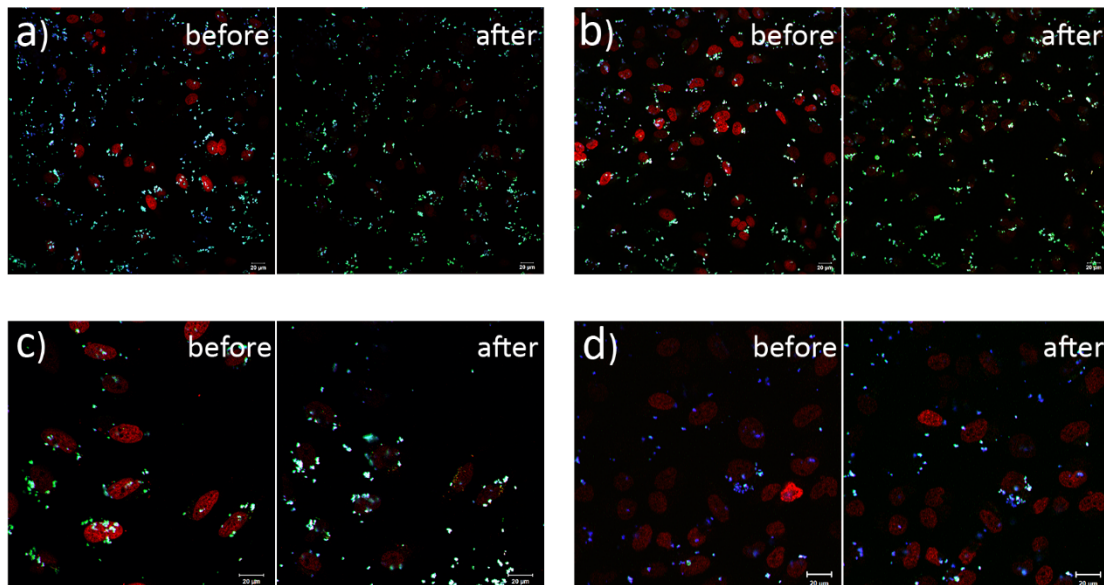
Figure 28: Representative 2-photon images of Hela cells with nanoparticles before (left) and after (right) AMF treatment in different conditions: a-b) 300 kHz, 15.2 kA/m; c-d) 300 kHz, 24.4 kA/m. Channels of intensity are coumarin (green), TAMRA (blue) and SYTO™ deep red (red) respectively. In comparison, there are weak intensity increase and spreading of coumarin.
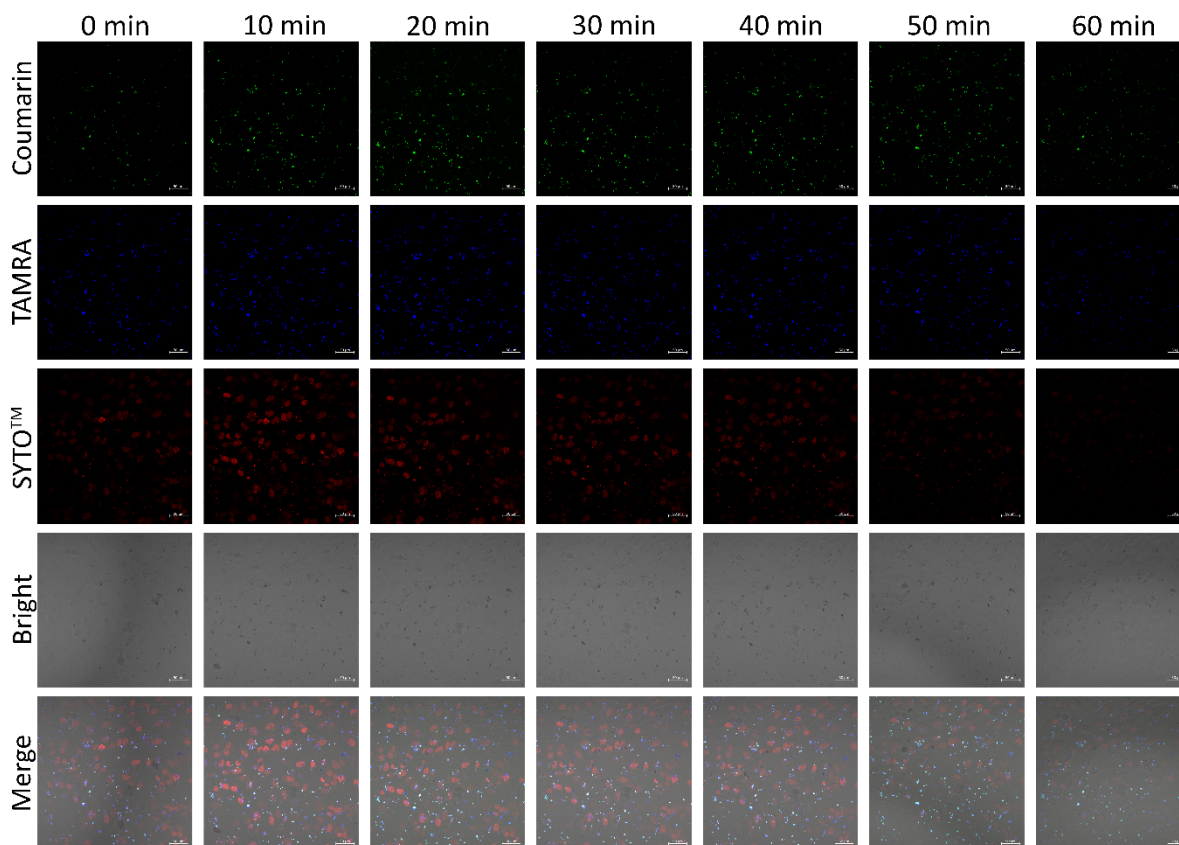
Figure 29: Representative 2-photon images of Hela cells with particles in process of AMF treatment (300 kHz, 24.4 kA/m) in each 10 min track.
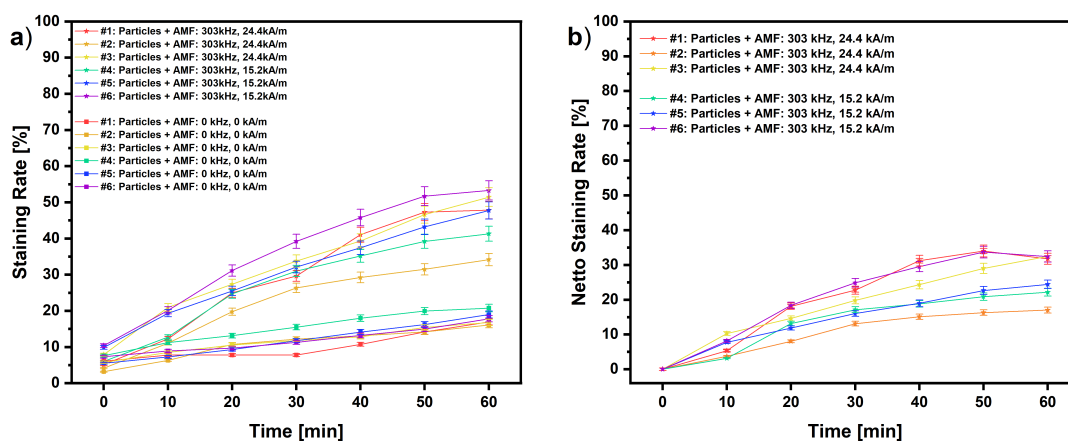

Figure 30: a) Images of release rate from Hela cells + particles with/without AMF treatment in different condition. Staining rate is concluded from 2-photon images in each time point. According to the images, staining rate of HeLa with particles and 60 min AMF treatment is about

between 30-50% and there is only almost 20% release rate from HeLa + particles without AMF as contrast. b) Netto staining rate optimized from a).

4.4.5.   Cellular Heating Map

Additionally, it is interesting to see how the temperature distribution looks like, when particles-uptaken cells are treated with AMF. As similar as previous process of 2-photon spectroscopic observation, images from IR-camera are taken before and in every 10 min from AMF treatment. In Figure 31, despite the participation of particles, there is weak temperature increase from cells with AMF, from which there was maximum only 1 °C difference. In opposites, cells without AMF were still in cool stand, which was around 0.1 °C increase and it means there was no heating.

Based on results, from which there was coumarin release from particles but no significant temperature increase, it can be concluded that the particles were affected from AMF and released coumarin. In another hand, due to the lower amount particles taken from cells, temperature of whole atmosphere in cell culture were not be influenced. It is thus determined that the particles could be applied in cell culture, which showed the drug release and also avoided hyperthermia.
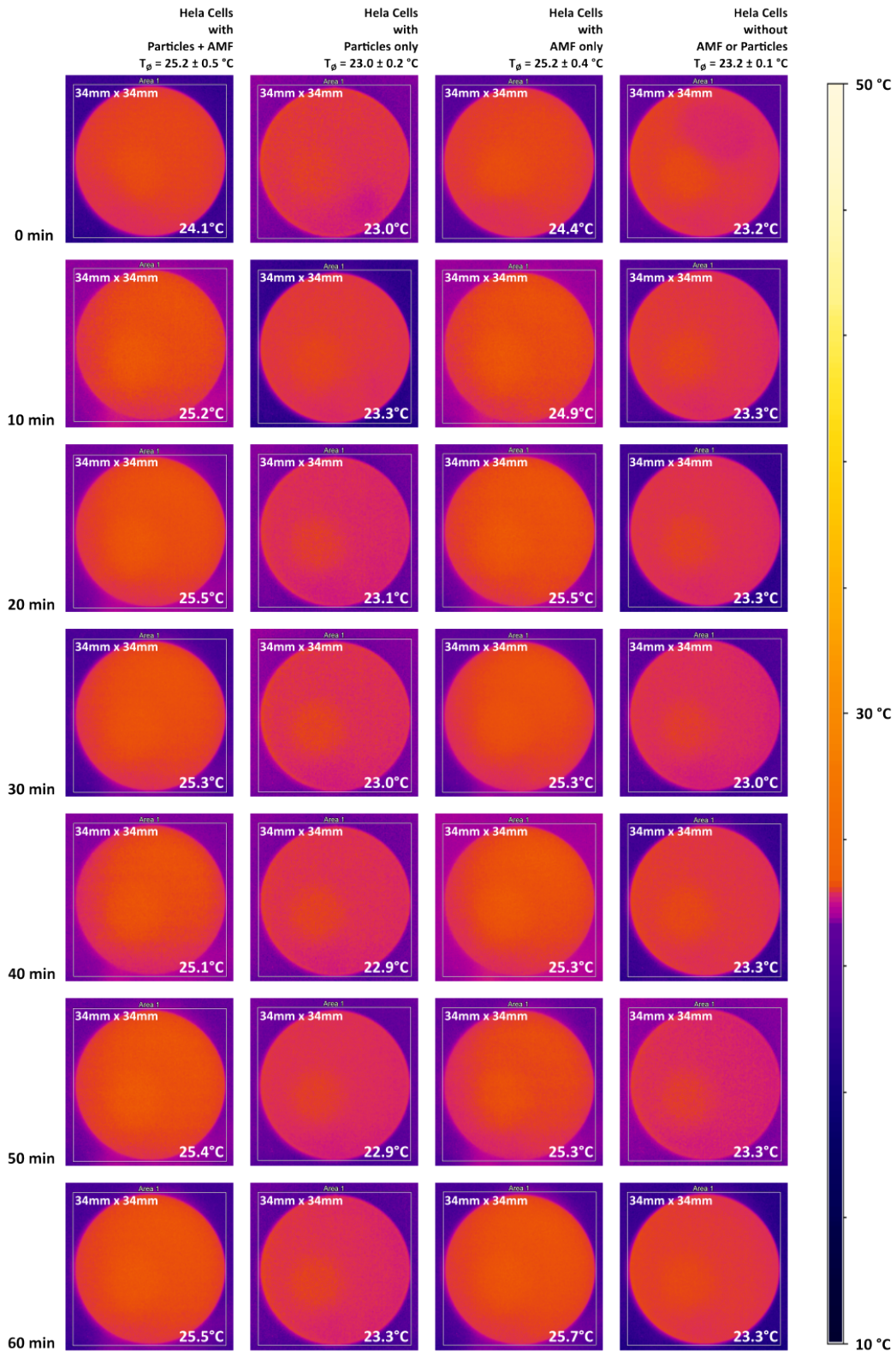
Figure 31: Temperature distribution of Hela cells and nanoparticles with 1 h AMF treatment: 24.4 kA/m and 300 kHz. Observation Area is static and with

size 34 mm × 34 mm. Average temperature with difference value from each sample was given respectively.

4.4.6.   Cell Viability

Last but not least, cytotoxicity is also important for characterization. The previous expectation is that regional heating are only adequate offering structural breakage of cargo and hyperthermia can be avoided. During particles participation and AMF treatment, cells stained with SYTO deep red from 2-photons images were counted and viability rate was calculated with followed function:

$$\textbf{Viability Rate } [\%] = \frac{\textbf{Stained Nucleus}_{\textbf{time point}}}{\textbf{Stained Nucleus}_{\textbf{start}}} \times \textbf{100}\%$$

According to Figure 32, it is determined that the combination of particles and AMF decreased the cell viability in approximately 10%. In contrast, the absence of particles or AMF led to weaker reduction. It is proposed that regional heating caused local hyperthermia.
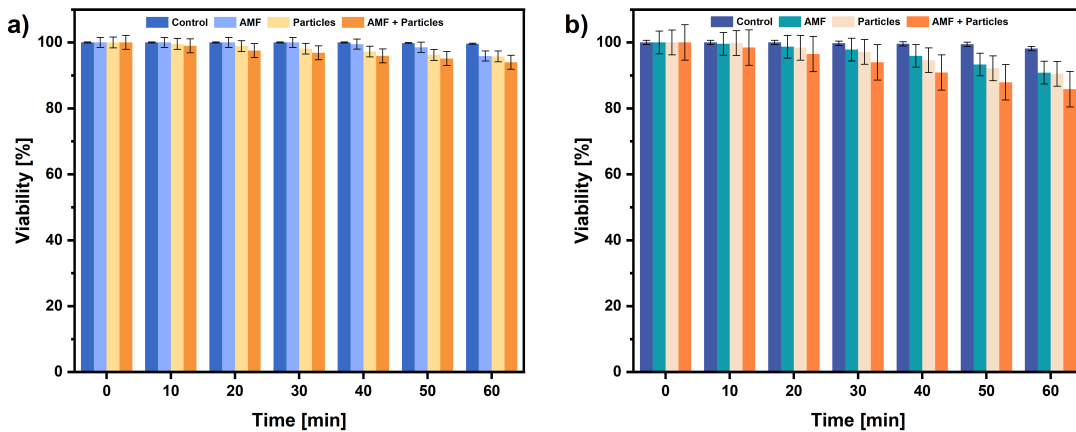

Figure 32:   Cell viability of HeLa cells in 1 h tracking with various conditions: blank, only with AMF, only with particles and with both particles and AMF. The conditions of AMF are a) 15.2 kA/m, 300 kHz and b) 24.4 kA/m, 300 kHz respectively.

4.5. Summary

Since decades, nano drug delivery system has been broadly developed. In general, the materials for drug delivery are ought to responsive to external stimuli in order to trigger or control the release. As mentioned before, magnetic field as an external stimulus demonstrated high potential in application of drug release due to outstanding tissue penetration in compared with light. Thus, it is meaningful to design a magnet responsive drug delivery system and investigate the interaction between magnetic field and the drug cargo.

In summary of main project, the magnetic triggered nano cargo Zn-IONPs@ZIF-8@PMA-DDA-TAMRA@(PAH/PSS)$_3$ has been performed. First, homogeneous magnetic zinc doped iron oxide nanoparticles (Zn-IONPs) were successfully synthesized with size around 20 nm. Porous hybrid framework ZIF-8 coating multiple magnetic particles enlarged the size to approximately 500 nm and offered the space for drug loading. Besides, the participation of PMA-DDA-TAMRA provided fluorescent localization of nanoparticles during microscopic observation. Furthermore, polyelectrolytes PAH and PSS construct the LbL-structure at the surface of Zn-IONPs@ZIF-8@PMA-DDA-TAMRA, which prevented the drug leakage before applications. Controlling the concentration of particles by fixing concentration of c(Fe-ion) =1 mg/mL, the heat induction of nanoparticles were tracked during AMF treatment, showing high temperature increase and indicating the responsivity of particles with magnetic field. More modifications demonstrated the decrease of heating rate. In addition, drug release of nano cargo with AMF can be demonstrated via fluorescence spectra, from which the fluorescence of supernatant increased gradually. This determined the process of drug release is controlled by AMF participation, proven by the switch on /off experiment.

In cell culture, HeLa cells have taken the cargos and nuclei-stained with SYTO deep red after 24h incubation. Moreover, drug release has taken place with 60 min AMF treatment, from which the fluorescence of guest drug coumarin dispersed from cargo and weakly stained the cytoplasm. In cell viability assay, however, the participation of both particles and AMF led to viability decrease around 10% at the end, which indicated the slight cytotoxicity. Moreover, the weakness of coumarin staining demonstrated the low capacity of cargo.

Side Project: Magnetothermal Cargo Delivery with Polyelectrolyte Multilayered Capsules (PEMCs) in vitro

5.   Motivation

From the main project, nanoparticles Zn-IONPs@ZIF-8@PMA-DDA-TAMRA@(PAH/PSS)$_3$ as nano drug cargos can be controlled by AMF for release. However, low drug capacity causing weak release was still a challenge. Thus, it is necessary to find out another strategy in order to overcome this main issue and achieve optimization. Inspired from LbL technology that polyelectrolytes are able to initiate self-assembly due to electrostatic interaction, it is considerable to investigate polyelectrolyte multilayered capsules cooperated with magnet responsive nanoparticles.

In practice, IONPs with OA-ligand were synthesized and coated with amphiphilic polymer PMA-DDA offering negative charges and hydrophilization. Following this, IONPs@PMA-DDA are able to participate in electrostatic assembly for PEMCs synthesis, consisting of polyelectrolytes PAH and PSS with positive and negative charge, respectively. Here, IONPs-PEMCs with size approximately 1-2 μm possessed large space and were loaded with guest fluorescent molecules calcein. Afterwards, drug cargo calcein@IONPs-PEMCs was applied for release by introduction of AMF.

In order to find out the equilibrium between cargo stability and trigger-responsivity, the construction of multilayers is an interesting point for investigation. Thus, the discussion about different positions of IONPs in the same PEMCs has been presented. In addition, PEMCs with IONPs confined inside the core, inspired from particles in main project, have been investigated.

Furthermore, the comparison of controllability between PEMCs and nanoparticles Zn-IONPs@ZIF-8@PMA-DDA-TAMRA@(PAH/PSS)$_3$ has been discussed.
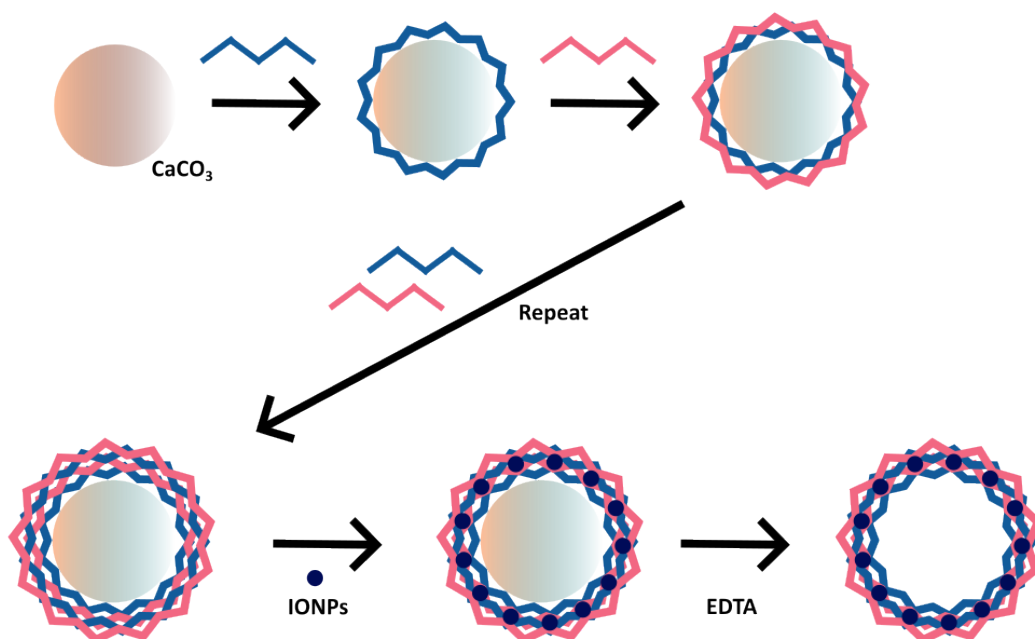
Figure 33: Fabrication of synthesis PEMCs with IONPs and guest molecules calcein. $CaCO_3$ as template constructed spherical structure. Afterwards, Polyelectrolytes PAH and PSS were repeatedly attached via electrostatic assembly. Image modified from *L. del Mercato et al.*[83]

6. Material, Synthesis and Methods

6.1. Materials

Name	CAS	Company	Comments
Iron(III) Oxide-Hydroxide	# 20344-49-4	Alfa Aesar	
Oleic Acid	#O1008	Sigma-Aldrich	
1-Octadecene	#8.22112	Sigma-Aldrich	
Dibenzyl Ether	#33630	Sigma-Aldrich	
1-Tetradecene	#87189	Sigma-Aldrich	
Poly(isobutylene-alt-maleic anhydride) (PMA)	#531278	Sigma-Aldrich	M_w~6000 kDa

Dodecylamine (DDA)	#8.03527	Sigma-Aldrich	
Calcein	#154071-48-4	Sigma-Aldrich	
Poly(sodium-4-styrene sulfonate) (PSS)	#243051	Sigma-Aldrich	
Poly(allylamine) Hydrochloride (PAH)	#283215	Sigma-Aldrich	$M_w \sim$ 17,500 kDa
Chloroform	#Y015.2	Carl Roth	
Chlorobenzene	#KK01.3	Carl Roth	
N,N-dimethylformamide (DMF)	#6251.1	Carl Roth	
Triethylamine (TEA)	#8.08352	Sigma-Aldrich	
Tetrahydrofuran (THF)	#6788.1	Carl Roth	
Ethylenediaminetetraacetic acid (EDTA)	# 60-00-4	Sigma-Aldrich	
Methanol (MeOH)	#8.22283	Supelco EMPLURA®	
Sodium Hydroxide (NaOH)	#6771.1	Carl Roth	
SYTO™ Deep Red	#S34900	Invitrogen™	Nucleic acid staining for live cells
Dulbecco's Modified Eagles Medium (DMEM)		ThermoFisher	
Phosphate-Buffered Saline (PBS)		Invitrogen	
Fetal Bovine Serum (FBS)		Biochrom	
Penicillin-Streptomycin (P/S)		ThermoFisher	
Trypsin-EDTA 0.05%		ThermoFisher	

6.2. Key Instruments

Name	Model	Company	Function
Transmission Electron Microscopy (TEM)	JEM- 1400PLUS	JEOL	NPs Geometry Visualization

Scanning Electron Microscopy (SEM)	SIGMA Gemini	ZEISS	NPs Morphology Visualization
Inductively Coupled Plasma Mass Spectrometry (ICP-MS)	7700 Series	Agilent	Concentration Control
Laser Scanning Microscope (LSM)	LSM 980 mit Airyscan 2	ZEISS	Drug Release in Cell Culture
Alternating Magnetic Field (AMF)	D5 Series	nanoscale Biomagnetics	Treatment of Drug Release
UV–vis Absorption Spectrophotometer	Agilent 8453	Agilent	NPs Characterization
Fluorescence Spectrometer (FL-spectra)	Cary Eclipse	Agilent	NPs Characterization
Dynamic Light Scattering (DLS)	NANO ZS	Malvern	NPs Characterization

6.3. Synthesis and Modification

6.3.1. Synthesis of IONPs

Synthesis of IONPs for PEMCs was followed by the report from *M. Kampferbeck et al.*[109] According to their protocol, 38.2 g (135 mmol) of OA, 13.8 g (45 mmol) of sodium oleate, 4.00 g (45 mmol) of iron(III) oxide-hydroxide α-FeO(OH) and 150 mL of 1-Octadecene were mixed in a 500 mL round-bottom three-neck flask equipped with a magnetic stirrer, a nitrogen gas inlet, a thermometer, and a distillation apparatus with a Vigreux column. The mixture was heated to 320 °C within 40 min and further to 333 °C after additional 50 min using a PILZ laboratory heater with a temperature controller operated at the maximum heating rate. Nucleation was observed 140 min after the start of heating by a change of the solution from transparent black to opaque black, accompanied by a temperature drop of the solution of ~2 °C. Once nucleation was observed, the temperature was held for 30 min at 333 °C. After cooling until room temperature, the solution was diluted with an equal volume of toluene, and 2 mL of OA was added. The nanoparticles were precipitated by addition of ethanol [1:1 (v/v)] and collected via centrifugation (6000×*g*, 6 min, 20 °C). The supernatant was decanted, and the remaining

pellet was redispersed in toluene and a few drops of OA. The purification procedure was repeated three times, followed by an additional precipitation with acetone as the nonsolvent instead of ethanol.

6.3.2.   Synthesis of Polymer PMA-DDA

Synthesis of polymer was similar as chapter 3.3.4.,following work from *C. A. J Lin et al.*[105] Only TAMRA-amine was absent by PMA-DDA synthesis.

Poly(isobutylene-alt-maleic anhydride) (PMA; M_w~6000) 10.22 mM unit (Mw 154 g/mol; 1.574g) and 30 mL DMF was added into a 100 three neck flask. The mixture was sonicated until it is not opaque anymore. Then, dodecylamine (DDA; 7.668 mM; 1.422 g; M_w: 185.35 g/mol; 75% molar ratio of PMA unit and 2.5 mL triethylamine (TEA) were added and the mixture was sonicated for a few seconds. It is recommended to add some tetrahydrofuran (THF) to solubilize DDA if the mixture cannot be dissolved in DMF. The mixture was heated to 70°C in darkness overnight.

Later on, the solvent of mixture was removed by contribution of rotary evaporator with rotation 100 rpm, temperature 75°C and maximum vacuum. Following this, 25 mL chloroform was added to dissolve the polymer and the whole solvent was removed again via rotary evaporator. Finally, 20.44 mL chloroform was added to polymer in order to get 0.5 M stock solution.

6.3.3.   Coating of IONPs with PMA-DDA

In order to modify the IONPs, polymer PMA-DDA-TAMRA was involved for modification. Referred from the work from *J. Hühn et al.*,[106] PMA-DDA stock solution (0.5 mL; 0.5 M) was diluted with 2.5 mL chloroform. Then, particles IONPs@ZIF-8 in 1mL methanol was added and mixed. Subsequently, the solvent was removed gently by rotary evaporator with rotation 100 rpm, temperature 30°C and vacuum 300 mbr. Afterwards, 4 mL chloroform was added to the product again for dissolving and removed again via rotary evaporator with rotation 100 rpm, temperature 30°C and maximum vacuum.

Following above, 10 mL NaOH aq was added and the mixture was sonicated for hydrophilization. Product was twice washed with MillQ-water, collected by magnet and finally redispersed in 1 mL methanol for next step.

6.3.4. PEMCs Construction (PAH/PSS)

Synthesis of PEMCs by self-assembly of polyelectrolytes is followed by *S. Carregal-Romero et al.*[91] In order to prepare the $CaCO_3$ templates, 1 mL of 0.33 M Na_2CO_3 and 0.33 M $CaCl_2$ in 0.1 M NaCl were mixed and stirred at 1000 rpm for 30 seconds, and then uninterrupted for 3 min. The resulting $CaCO_3$ particles were transferred into 2 mL tubes and washed with Milli-Q water three times removing residual salts.

Following this, alternating layers of poly(allylamine hydrochloride) (PAH) with a positive charge and poly(sodium 4-styrene sulfonate) (PSS) with a negative charge were sequentially deposited on the $CaCO_3$ cores. Both PSS and PAH were applied with concentration of 0.2 M in 0.1 M NaCl aq. First, 2 mL PSS solution was mixed with $CaCO_3$ cores in water solution, followed by 3 min sonication and 10 min shaking for assembly. The suspension was then washed three times to remove excess polymer. Afterwards, 2 mL PAH was added as the same as the previous step. The process was repeated to build the desired multilayer structure, depending on the design of expecting structure. IONPs coated with PMA-DDA possessing negative surface charge were incorporated into the capsule shell by assembling them between two positive charged layers due to electrostatic interactions. Zeta potential of the surface was tracked by dynamic light scattering (DLS) to recognize the changing of the surface charge. Once the designed multilayered capsule was fine constructed, $CaCO_3$ cores were removed by stewing in 0.2 M EDTA aq (pH=7) overnight, forming an EDTA-Ca complex and leaving behind hollow capsules.

6.3.5. Drug Loading (Calcein)

Drug loading of PEMCs with calcein is followed by the protocol, from which 1 mL of 3 mg/mL calcein aq solution (pH=5.8) was mixed with capsules and the resulting suspension was stewed in 1 h followed by heat shrinkage at 75°C for 90 minutes for encapsulation. Finally, the unencapsulated dye was removed by washing capsules with Milli-Q water three times.

6.3.6. Cell Culture

Cell culture is followed as mentioned in chapter 3.3.8.

HeLa (cervical cancer cell line) were cultured in Dulbecco's Modified Eagle Medium with phenol red, 4.5 g/L D-glucose, L-glutamine and pyruvate (DMEM, 1X, Gibco, #41966-029) supplemented with 10% Fetal Bovine Serum (Gibco, #10270-106) and 1% Penicillin Streptomycin (P/S, Corning, 100X, #30-002-CI). Cells were maintained under humid conditions at 37 °C and 5% of CO_2.

In order to perform 2-photon images with living cells, Hela Cells with amount 50×10^3 in1 mL cell culture medium were seeded on 35 mm low µ-Dish with 500 grids (Ibidi, Germany, #80156) for 24 h before up-taking particles again 24h incubation.

6.3.7. Two-Photon Imaging

All 2-Photon images were acquired by LSM 980 mit Airyscan 2 with objective 20x and processed with ZEN Microscopy Software. Applied ex./em. wavelengths for 2-photon images were followed:

- 488 nm/510-540 nm: Calcein as uptaken drug (green)

Images were taken from the beginning and after each 10 min AMF treatment until 60 min. Cell dish was placed at the center of the planar coil PC70 from D5 Serie by nanoScale Biomagnetic. Program of software from D5 was set as experiment mode with frequency 300 kHz and current 15.2 kA/m or 24.4 kA/m for 10 min.

7.   Results

7.1. Capsules

As a start investigation, first PEMCs with structure IONPs@(PAH/PSS)$_4$ has been synthesized and characterized in Figure 34, demonstrating that the size of IONPs and PEMCs are approximately 26 nm and 5.3 µm, respectively. Besides, according to Figure 34 a) and b), it is clear to observe that IONPs are perfectly covered inside the hollow structure. Besides, Figure 34 e) determined that guest molecules calcein were loaded inside the PEMCs successfully based on the perfect overlap from visible image and fluorescence signal.
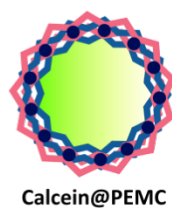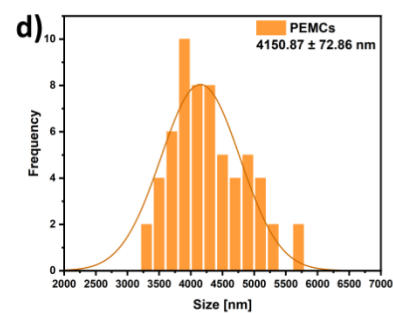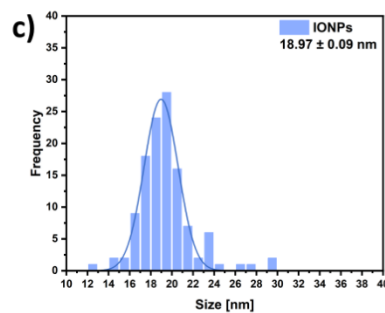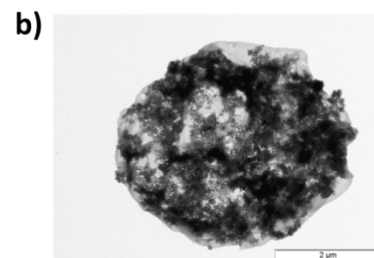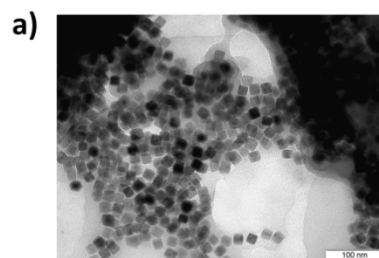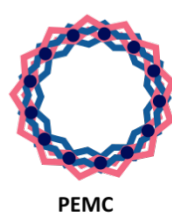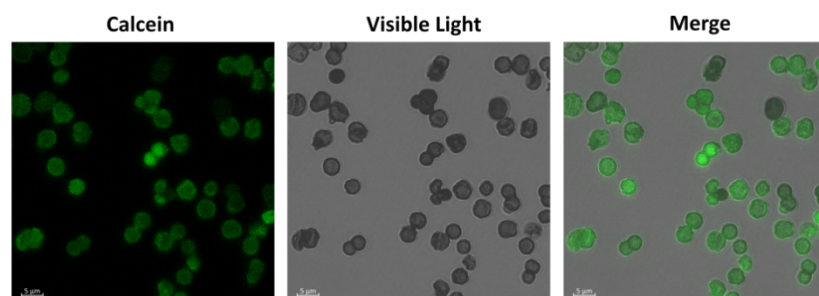
Figure 34: a) and b) TEM images of PEMCs IONPs@(PSS/PAH)$_4$ in different magnitudes; c) and d) Size distributions of IONPs and PEMCs, respectively; e) Two-photon images of PEMCs loaded with calcein.

7.2. Heat Generation

Similar as process of chapter 4.3., 1 mL 0.25 mg/mL PEMCs in water were dispersed in glass vial, which is matched with temperature sensor and calorimetry coil from D5. Vial was inserted into the coil. Frequency and current (300 kHz; 15.2 kA/m, 24.4 kA/m, 36.6 kA/m) were as set and temperature was tracked and recorded for 600 s.

According to Figure 35, the temperature of PEMCs increased with AMF treatment, which proved that PEMCs are able to generate heat during AMF process. However, due to lower concentration IONPs, the increase rate is not quite significant. Thus, it is curious to see the performance of PEMCs with AMF in cell cultural application.
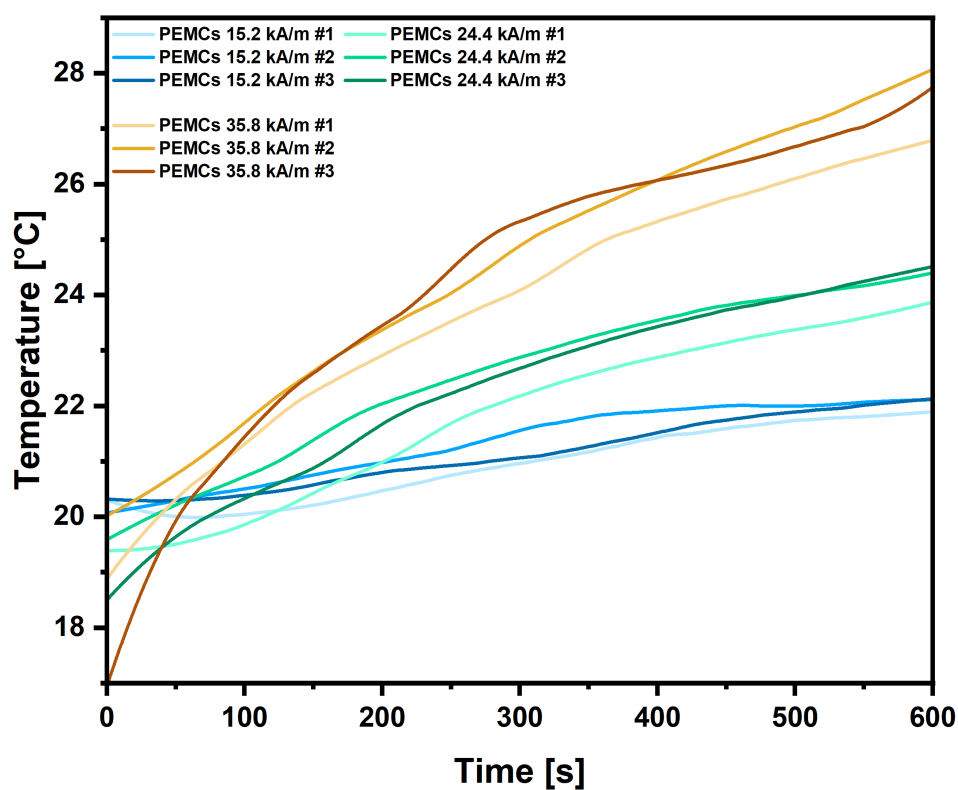
Figure 35:   Heat generation of 0.25 mg/mL PEMCs IONPs@(PSS/PAH)$_4$ in treatment of alternating magnetic field with frequency 303 kHz and current 15.2 kA/m, 24.4 kA/m and 35.8 kA/m. Image demonstrates the reproducibility of heat generation.

7.3. Two-Photon Imaging (Uptake)

Before AMF treatment for PEMCs with cells, shown from images of 2-photon spectroscopy, it is clear to see the signal from calcein (green) and bright field. From Figure 36, fluorescence of calcein (green) and and the hollow structure in bright field are perfectly overlapped, which were separated in cells, demonstrating that PEMCs were uptaken after 24 h incubation. In addition, there were several stained cell in green, which determined there was calcein drug leakage during the incubation and it is not expected.
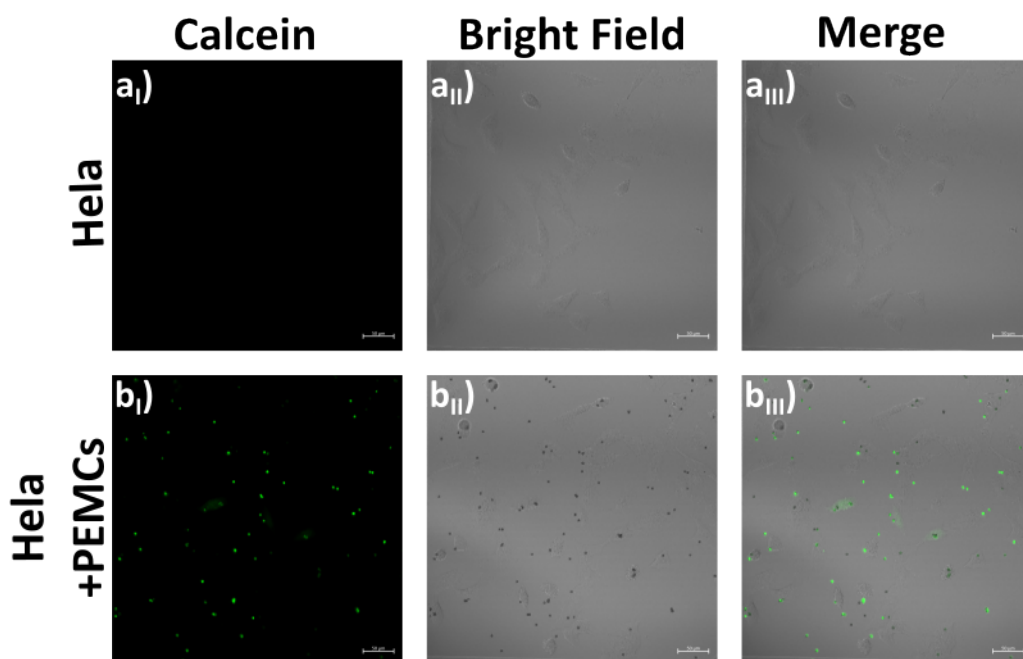

Figure 36:   2-photon images of a) Hela cells and b) Hela cells with PEMCs: IONPs@(PAH/PSS)$_4$. Each channel represents respectively: I) calcein

(green), II) bright field and III) merge. All images were taken after 24 h incubation and before AMF treatment.

7.4. Two-Photon Imaging (Drug Release)

Drug release of PEMCs with various structure has been investigated. Based on the results from first release studying, as shown in Figure 37, there were several stained cells before the alternating magnetic treatment due to the drug leakage from several capsules. Furthermore, there were barely no increase of stained cells, which demonstrated no drug release from calcein@PEMCs with AMF treatment. Thus, it is necessary to investigate a proper structure for achieving release.
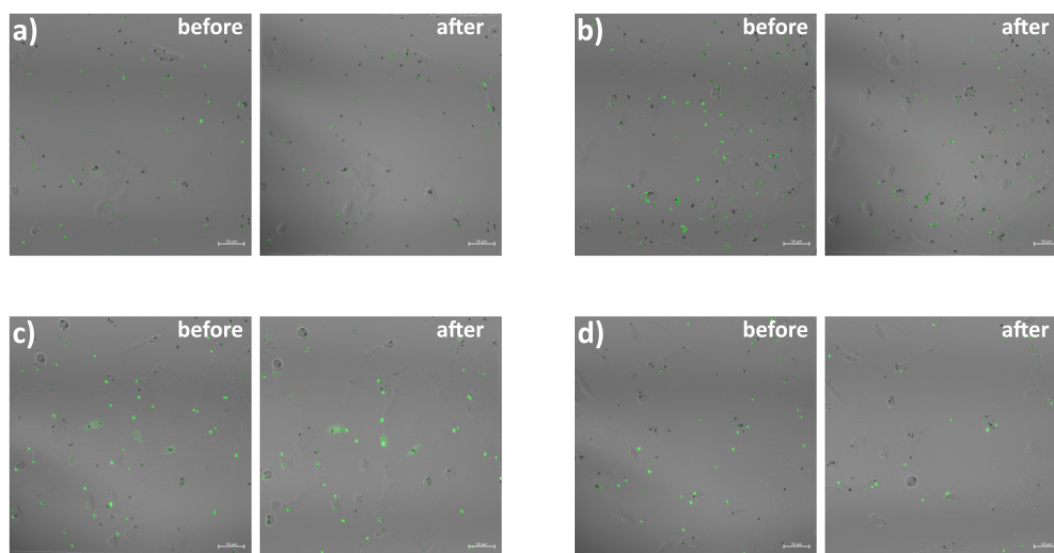

Figure 37: Representative 2-photon images of Hela cells with PEMCs before (left) and after (right) treated with different conditions: a-b) blank: 0 kHz, 0 kA/m; c-d) AMF:300 kHz, 24.4 kA/m. Channels of intensity of calcein is labeled in green. It is determined there is no drug release by AMF treatment.

Comparison A:

In the first point for investigation, the structures for comparison are designed as followed:

No.	Multilayer Structure
#1	(PSS/PAH)$_2$/IONPs/PAH/PSS
#2	(PSS/PAH)$_2$/IONPs/(PAH/PSS)$_2$
#3	(PSS/PAH)$_2$/IONPs/PAH/IONPs/PAH/PSS

Here, two layer-pairs of PSS/PAH were contributed for building up the base of the spherical structure. Then, iron particles were placed at the third layer with introduced concentration 1 mg/mL and different structure were designed. Sample no. 1 and 2 were the comparison of the thickness in order to avoid calcein leakage before AMF treatment. Furthermore, the introduction of multi-IONPs-layers in PEMCs would also be interesting to investigate the possibility for increasing magnetic thermal responsivity. According to Figure 38, however, there were stained cells before AMF treatment in all cases, demonstrated the drug leakage. Plus, difference can be barely observed because there was no increased stained cells after AMF treatment, although the fluorescence of calcein can still be observed in PEMCs. Therefore, it could be determined that the structures above were not ideal for magnetic triggered release platforms and it inspiring to play around other possibility.
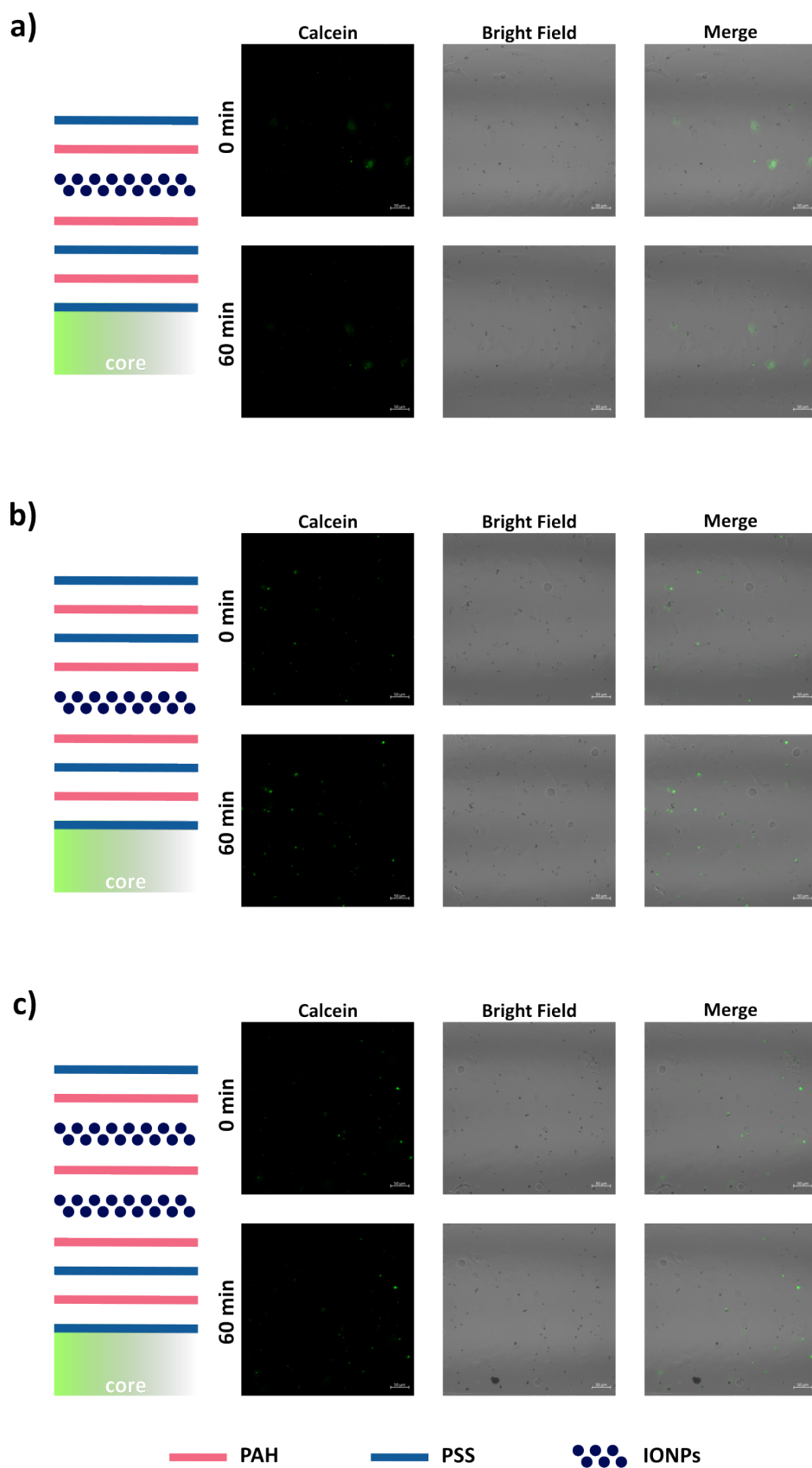
Figure 38: 2-photon images of PEMCs uptaken from Hela cells in AMF treatment with frequency 303 kHz and 24.4 kA/m: a) #1, b) #2, c) #3.

Comparison B:

Inspired by the main project, the guidance of IONPs inside the core might be also a promising possibility for optimization. Designs were followed:

No.	Multilayer Structure
#4	IONPs@(PAH/PSS)$_4$
#5	IONPs@PAH/PSS/PAH/IONPs/(PAH/PSS)$_2$
#6	IONPs@PAH/PSS/PAH/IONPs/PAH/IONPs/PAH/PSS

Herein, since drug release is the main assignment, the responsivity of PEMCs should be in priority, for which IONPs were placed in core and also between multilayers. Besides, the concentration of IONPs introduction for cores and multilayers was 1 mg/mL. According to Figure 39, unfortunately, the result looked like the same as before that the issue of drug leakage remained and there was no increased stained cells for release demonstration.
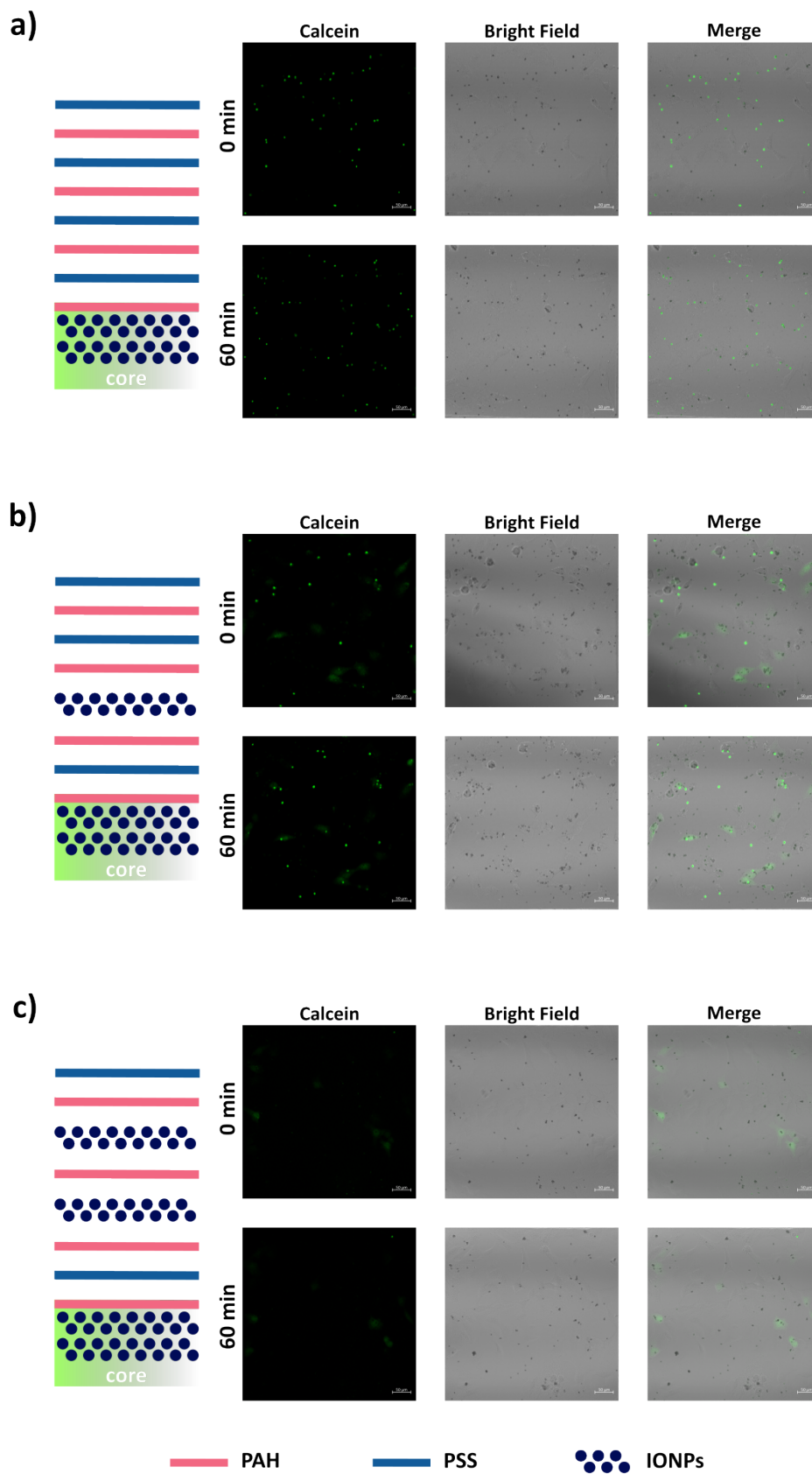
Figure 39: 2-photon images of PEMCs uptaken from Hela cells in AMF treatment with frequency 303 kHz and 24.4 kA/m: a) #4, b) #5, c) #6.

Comparison C:

Another point of view for optimization would be if the different sorts of multilayers for PEMCs could be optimized. Thus, another comparison was designed as followed:

No.	Multilayer Structure
#7	PSS/PAH/IONPs/(PAH/PSS)$_3$
#8	(PSS/PAH)$_2$/IONPs/(PAH/PSS)$_2$
#9	(PSS/PAH)$_3$/IONPs/PAH/PSS

As the same as before, IONPs introduction remained with remained concentration 1 mg/mL and were placed in PEMCs with the same general combinations but different sort. According to Figure 40, the previous issues still occurred: drug leakage and no controllable release. This led us to review and have a discussion between PEMCs and the nano cargo by main project.
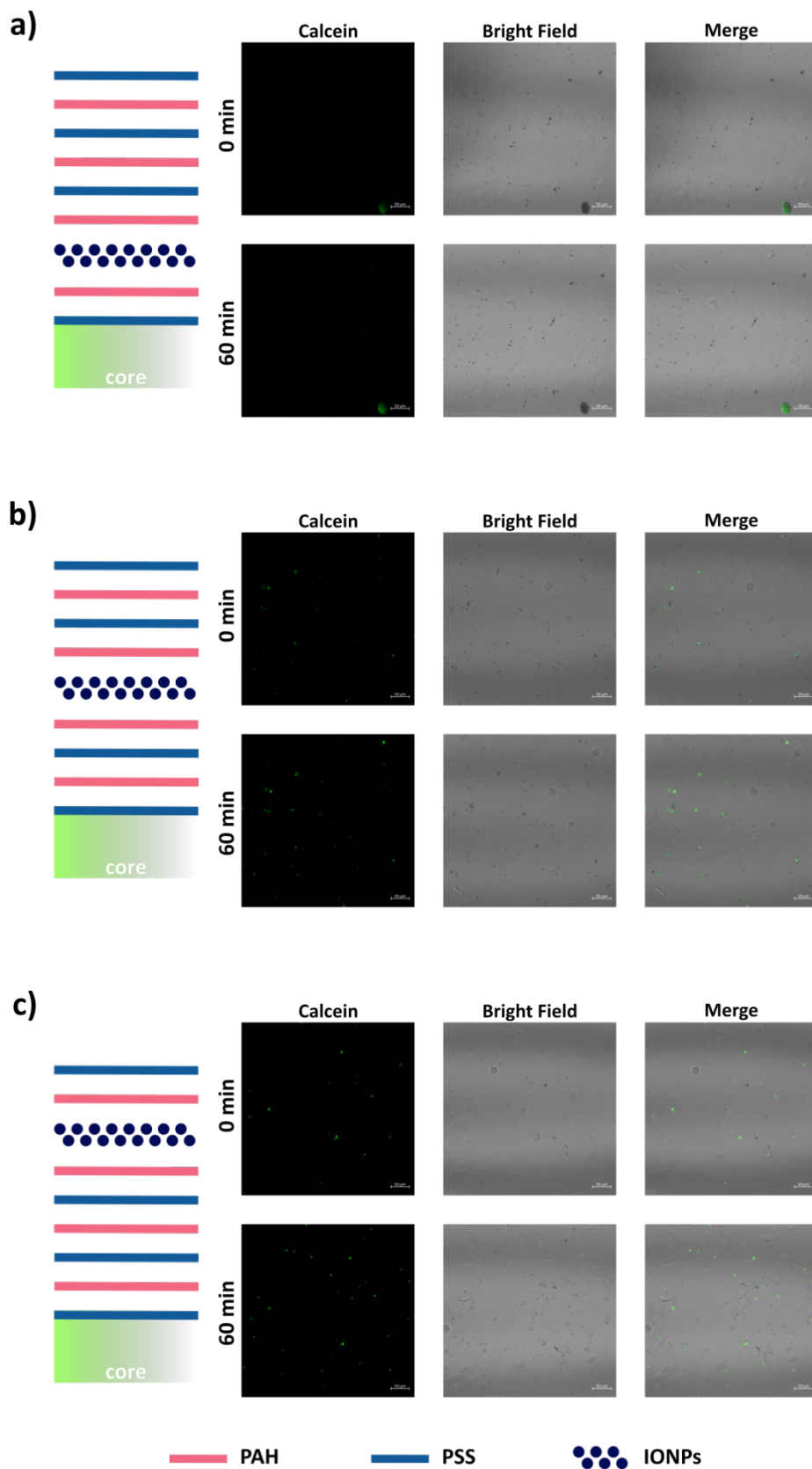
Figure 40: 2-photon images of PEMCs uptaken from Hela cells in AMF treatment with frequency 303 kHz and 24.4 kA/m: a) #7, b) #8, c) #9.

7.5. Discussion

Unfortunately, there was no release from PEMCs despite different structure designs. In contrast with MOFs-composites in main project, it is necessary to review for optimization. First reason might be the size. Comparing between Figure 19 e) and Figure 34 b), the size of IONPs between Zn-IONPs@ZIF-8@PMA-DDA-TAMRA@(PAH/PSS)$_3$ (MOFs-cargos) and PEMCs are quite different, which causes different uptake distribution in cell culture. As shown in Figure 19 e) and Figure 34 b), it is clear to observe the size of MOFs-cargos and PEMCs are 657.69 nm and 5.3 μm (5300 nm), respectively. Comparing with each HeLa cell taking around 3-6 MOFs-cargos, only 1-2 PEMCs can be uptaken from several HeLa cells, shown in Figure 41. It caused the different concentration of uptaken magnetic particles in cells. If it can be supposed that 20 nm MNPs fully occupied the ZIF-8 sphere by MOF-cargo, it is be estimated that there would be about 10,000 – 20,000 MNPs inside the cells, followed by spherical volume function. In contrast, if 20nm MNPs were homogeneous separated as a single layer by PEMCs, there would be around 7,000 – 14,000 MNPs in some individual cells based on spherical area function. Due to higher concentration of MNPs leading to more heat generation, MOFs-cargos possessed adequate heat to process the drug release. In another side, lower concentration of MNPs by PEMCs led to less energy production, which might be the reason why multilayered structure cannot be damaged.
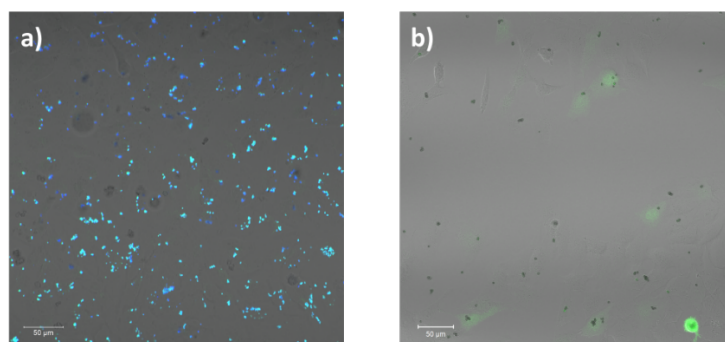

Figure 41:   2-photon images of particles uptake pattern: a) MOFs-cargos and b) PEMCs.

Second, it is a competition between MNPs and guest molecules in a cargo. If it is supposed that the size of MOFs-cargos and PEMCs are the same, for example 500 nm, MNPs are only distributed in the multilayers of PEMC spheres offering the core space for guest molecules. In contrast, an almost full occupation of MNPs in the core cause less space for guest molecules. That might be the reason that there is weak but controllable release from MOFs-cargo via AMF control and, at the same time, no release by PEMCs with AMF treatment. Therefore, it would be a potential to find out the equilibrium between MNPs and guest molecules, by which MNPs offer enough heat generation and there is abundant space for taking guest molecules.

Concluding the reasons above, smaller size particles with proper distribution between MNPs and guest molecules is definitely a nice agenda for further investigation. For MOFs-cargo, one promising optimization could be removing ZIF-8 structure by smooth acid after PEs layer assembly. The elimination of ZIF-8 leave relatively more free space. i.e., ZIF-8 can be a template for smaller PEMCs.

Conclusion

In this study, two nanoplatforms were responsive with alternating magnetic field and demonstrated potential for applications in biomedical field. In main project, MOFs-cargo Zn-IONPs@ZIF-8@PMA-DDA-TAMRA@(PAH/PSS)$_3$ showed the stability, low-toxicity, fluorescence localizing and outstanding release controllability but small drug capacity, while PEMCs provide large space for drug molecules but not controllable breakage due to lack of MNPs, showed in side project. The results pointed out the amount of MNPs is crucial for heat generation and the conciliation of space between MNPs and drug molecules. However, this thesis also showed that magnetic field triggered materials have still bright future for drug delivery system and it is definitely worthwhile to explore and investigate further performance of these nanomaterials in biomedical applications.

Appendix

A1. List of Hazardous Substances

Substance	Signal	GHS-Symbols	Hazard Statements	Precautionary Statements
Iron(III) Acetylacetonate	Danger		H302 + H312 + H332, H318	P26 - P280 - P30 + P312 - P302 + P352 + P31 - P304 + P340 + P312 - P305 + P351 + P338
Zinc(II) Acetylacetonate	Warning		H317 - H319 - H410	P261 - P264 - P273 - P280 - P302 + P352 - P305 + P351 + P338
1-Octadecene	Danger		H304	P301 + P310 - P331 - P405 - P501
Dibenzyl Ether	Warning		H317, H410	P261 - P272 - P273 - P280 - P302 + P352 - P333 + P313
1-Tetradecene	Danger		H304	P301 + P310 - P331 - P405 - P501
Citric Acid	Warning		H319, H335	P261 - P264 - P271 - P280 - P304 + P340 + P312 - P305 + P351 + P338

Zinc Nitrate Hexahydrate ($Zn(NO_3)_2 \cdot 6H_2O$)	Danger		H272, H302, H315, H319, H335, H410	P210 - P220 - P273 - P301 + P312 - P302 + P352 - P305 + P351 + P338
2-Methylimidazole (2-MeIM)	Danger		H302, H314, H351, H360Df	P260 - P280 - P301 + P312 - P303 + P361 + P353 - P304 + P340 + P310 - P305 + P351 + P338
Dodecylamine (DDA)	Danger		H304, H314, H335, H373, H410	P260 - P280 - P301 + P330 + P331 - P303 + P361 + P353 - P304 + P340 + P310 - P305 + P351 + P338
Poly(allylamine) Hydrochloride (PAH)	Warning		H302, H317	P280 - P301 + P312 + P330 - P302 + P352
Chloroform	Danger		H302, H315, H319, H331, H336, H351, H361d, H372	P202 - P301 + P312 - P302 + P352 - P304 + P340 + P311 - P305 + P351 + P338 - P308 + P313
Chlorobenzene	Warning		H226, H315, H332, H411	P210 - P233 - P240 - P273 - P303 + P361 +

				P353 - P304 + P340 + P312
N,N-dimethylformamide (DMF)	Danger		H226, H312 + H332, H319, H360D	P210 - P280 - P303 + P361 + P353 - P304 + P340 + P312 - P305 + P351 + P338 - P308 + P313
Triethylamine (TEA)	Danger		H225, H302, H311 + H331, H314, H335	P210 - P280 - P301 + P312 - P303 + P361 + P353 - P304 + P340 + P310 - P305 + P351 + P338
Tetrahydrofuran (THF)	Danger		H225, H302, H319, H335, H336, H351	P202 - P210 - P233 - P301 + P312 - P305 + P351 + P338 - P308 + P313
Methanol (MeOH)	Danger		H225, H301 + H311 + H331, H370	P210 - P233 - P280 - P301 + P310 - P303 + P361 + P353 - P304 + P340 + P311
Sodium Hydroxide (NaOH)	Danger		H290, H314	P234 - P260 - P280 - P303 + P361 + P353 - P304 + P340 + P310 - P305 + P351 + P338

A2. Internship

- **HeatNMof:**

Heating triggered drug release from nanometric inorganic-metal–organic frameworks composites, an EU innovative training network aims to train the next generation of material scientists in a highly interdisciplinary and intersectoral research environment.

Post Section, Hamburg, Germany, 24th-26th October 2022

Website: https://heatnmof.eu/

- **Girls' Day in den Nanowissenschaften**:

Educational programme for teenagers above 5th Grade for occupational orientation in the future.

Leader of Block 3: SEM and Liquid Nitrogen, Hamburg, Germany, 25th April 2024

Website: https://www.physik.uni-hamburg.de/ueber-den-fachbereich/aktuelles/2024/0508-girlsday-in-nanophysik.html

Acknowledgement

I would like to express my deepest gratitude to all those who have contributed to the completion of this thesis. First and foremost, I would like to thank my supervisor, Prof. Dr. Wolfgang J. Parak, for his invaluable guidance, support, inspiration and encouragement throughout my research. Their expertise and insights have greatly enriched my work. Also, I am grateful for his adventurous decision and guidance for me to take responsibility for compulsory teaching (exercise classes for bachelors) and a section of event Girls' Day with over 300 students. These are definitely precious experiences and chance to communicate with young generation in Germany. Moreover, it is for me an honor to encourage them to join the scientific field.

I am also thankful to my co-supervisor, Prof. Dr. Robert H. Blick, for his invaluable insight and constructive suggestions during my doctoral studying, which are meaningful for thesis development.

A sincere appreciation to Assoc. Prof. Dr. Dingcheng Zhu, Assoc. Prof. Dr. Lili Feng and Dr. Florian Schulz for their professional support and guidance in different moments of my Ph.D. journey and their precious experience sharing of various appliable technologies.

Thanks to Prof. Dr. Nils Huse and Dr. Robert Frömter for their allowance and training for SEM operation and thanks to Stefan Werner for his TEM service. Thanks to Maria Pozzi for giving me great suggestions and knowledge to solve issues related to cell biology. Thanks to Dr. Gerwin Chilla and Marten Rittner for their technical support in order to make sure the instruments are in great stand. Thanks to Yang Ye and Helen Oqueka for their support for all administrative documents.

Special, special thanks to Le Kim Yen Nguyen for her contribution in PEMCs side project and the credits belong to her. With her effort, we found out some possibilities and know how to make things better.

Furthermore, a sincere thank you goes to my colleagues in Biophotonik Group, whose camaraderie and stimulating discussions made my time in the department truly enjoyable. I appreciate the support and friendship for being there during both challenging and rewarding moments:

Dr. Yanan Kang   Dr. Yang Liu   Dr. Bing Qi

I would like to express my heartfelt gratitude to my parents for their unwavering support and encouragement throughout my journey. Their belief in my potential and their sacrifices have provided me with the foundation necessary to pursue my goals and aspirations. They have instilled in me the values of perseverance, hard work, and integrity, which have guided me in both my personal and professional endeavors. Their love and guidance have been instrumental in shaping my character and ambitions, allowing me to overcome challenges and strive for excellence. I am deeply grateful for their encouragement during moments of uncertainty and for celebrating my achievements with me. Thank you for always being there.

Last but not least, I would like to thank myself for determination, effort and still belief in me. This journey is full of challenges and I am proud of myself always trying my best to conquer them. I will always remember my academic life in this wonderful city.

Thank you for always being there!

References

1. Vargason, A.M., A.C. Anselmo, and S. Mitragotri, *The evolution of commercial drug delivery technologies.* Nat Biomed Eng, 2021. **5**(9): p. 951-967.

2. Langer, R., *New Methods of Drug Delivery.* Science, 1990. **249**(4976): p. 1527-1533.

3. Theresa M. Allen, P.R.C., *Drug Delivery Systems: Entering the Mainstream.* Science, 2004. **303**(5665): p. 1818-1822.

4. Sun, T., et al., *Physical triggering strategies for drug delivery.* Adv Drug Deliv Rev, 2020. **158**: p. 36-62.

5. Naumenko, E., I. Guryanov, and M. Gomzikova, *Drug Delivery Nano-Platforms for Advanced Cancer Therapy.* Scientia Pharmaceutica, 2024. **92**(2).

6. Andrew, P.A.B.E.R., *RF magnetic field penetration, phase shift and power dissipation in biological tissue: implications for NMR imaging.* Physics in Medicine & Biology, 1978. **23**(4): p. 630-643.

7. Wang, Y. and D.S. Kohane, *External triggering and triggered targeting strategies for drug delivery.* Nature Reviews Materials, 2017. **2**(6).

8. Hegyi, G., G.P. Szigeti, and A. Szasz, *Hyperthermia versus Oncothermia: Cellular Effects in Complementary Cancer Therapy.* Evid Based Complement Alternat Med, 2013. **2013**: p. 672873.

9. Bayda, S., et al., *The History of Nanoscience and Nanotechnology: From Chemical–Physical Applications to Nanomedicine.* Molecules, 2020. **25**(1): p. 112.

10. Feynman, R., *There's plenty of room at the bottom*, in *Feynman and computation*. 2018, CRC Press. p. 63-76.

11. Iqbal, P., J.A. Preece, and P.M. Mendes, *Nanotechnology: The "Top-Down" and "Bottom-Up" Approaches*, in *Supramolecular Chemistry*. 2012.

12. Bray, F., et al., *Global cancer statistics 2022: GLOBOCAN estimates of incidence and mortality worldwide for 36 cancers in 185 countries.* CA: A Cancer Journal for Clinicians, 2024. **74**(3): p. 229-263.

13. Han, X., et al., *Applications of nanoparticles in biomedical imaging.* Nanoscale, 2019. **11**(3): p. 799-819.

14. Li, W., et al., *Fluorescent Nanoparticles for Super-Resolution Imaging.* Chemical Reviews, 2022. **122**(15): p. 12495-12543.

15. Heidt, T. and M. Nahrendorf, *Multimodal iron oxide nanoparticles for hybrid biomedical imaging.* NMR in Biomedicine, 2013. **26**(7): p. 756-765.

16. Malik, S., et al., *Nanomaterials-based biosensor and their applications: A review.* Heliyon, 2023. **9**(9): p. e19929.

17. Aldewachi, H., et al., *Gold nanoparticle-based colorimetric biosensors.* Nanoscale, 2018. **10**(1): p. 18-33.

18. Altug, H., et al., *Advances and applications of nanophotonic biosensors.* Nature Nanotechnology, 2022. **17**(1): p. 5-16.

19. Siddique, S. and J.C.L. Chow, *Gold Nanoparticles for Drug Delivery and Cancer Therapy.* Applied Sciences, 2020. **10**(11): p. 3824.

20. Altpeter, I., R. Tschuncky, and K. Szielasko, *8 - Electromagnetic techniques for materials characterization*, in *Materials Characterization Using Nondestructive Evaluation (NDE) Methods*, G. Hübschen, et al., Editors. 2016, Woodhead Publishing. p. 225-262.

21. Rapp, T.L. and C.A. DeForest, *Targeting drug delivery with light: A highly focused approach.* Advanced Drug Delivery Reviews, 2021. **171**: p. 94-107.

22. Coey, J.M.D. and F. Mazaleyrat, *History of magnetism ☆*, in *Encyclopedia of Condensed Matter Physics (Second Edition)*, T. Chakraborty, Editor. 2024, Academic Press: Oxford. p. 1-17.

23. Thompson, F., *Paramagnetic and diamagnetic materials.* Physics Education, 2011. **46**(3): p. 328.

24. Kaufman, A.A., R.O. Hansen, and R.L.K. Kleinberg, *Chapter 6 Paramagnetism, Diamagnetism, and Ferromagnetism*, in *Methods in Geochemistry and Geophysics*, A.A. Kaufman, R.O. Hansen, and R.L.K. Kleinberg, Editors. 2008, Elsevier. p. 207-254.

25. Martin, D.H., *Magnetism in solids*. 1967, London: Iliffe Books Ltd.

26. Van Den Handel, J., *Paramagnetism*, in *Advances in Electronics and Electron Physics*. 1954, Elsevier. p. 463-518.

27. Koksharov, Y.A., *Magnetism of Nanoparticles: Effects of Size, Shape, and Interactions*, in *Magnetic Nanoparticles*. 2009. p. 197-254.

28. Aharoni, A., *Introduction to the Theory of Ferromagnetism*. Vol. 109. 2000: Clarendon Press.

29. Bean, C. and u.D. Livingston, *Superparamagnetism.* Journal of Applied Physics, 1959. **30**(4): p. S120-S129.

30. Chen, D.-X., et al., *Size determination of superparamagnetic nanoparticles from magnetization curve.* Journal of Applied Physics, 2009. **105**(8).

31. Fortin, J.-P., F. Gazeau, and C. Wilhelm, *Intracellular heating of living cells through Néel relaxation of magnetic nanoparticles.* European Biophysics Journal, 2008. **37**: p. 223-228.

32. Dieckhoff, J., et al., *Magnetic-field dependence of Brownian and Néel relaxation times.* Journal of applied physics, 2016. **119**(4).

33. Zhao, W., et al., *Superparamagnetic enhancement of thermoelectric performance.* Nature, 2017. **549**(7671): p. 247-251.

34.   Kita, E., et al., *Ferromagnetic nanoparticles for magnetic hyperthermia and thermoablation therapy.* Journal of Physics D: Applied Physics, 2010. **43**(47): p. 474011.

35.   Gossuin, Y., et al., *Magnetic resonance relaxation properties of superparamagnetic particles.* Wiley Interdisciplinary Reviews: Nanomedicine and Nanobiotechnology, 2009. **1**(3): p. 299-310.

36.   Hergt, R., S. Dutz, and M. Röder, *Effects of size distribution on hysteresis losses of magnetic nanoparticles for hyperthermia.* Journal of Physics: Condensed Matter, 2008. **20**(38): p. 385214.

37.   Noh, S.-h., et al., *Nanoscale Magnetism Control via Surface and Exchange Anisotropy for Optimized Ferrimagnetic Hysteresis.* Nano Letters, 2012. **12**(7): p. 3716-3721.

38.   Alcantara, D. and L. Josephson, *Chapter 11. Magnetic Nanoparticles for Application in Biomedical Sensing*. 2012.

39.   Rosensweig, R.E., *Heating magnetic fluid with alternating magnetic field.* Journal of Magnetism and Magnetic Materials, 2002. **252**: p. 370-374.

40.   Q. A. Pankhurst, J.C., S. K. Jones and J. Dobson, *Applications of magnetic nanoparticles in biomedicine.* Journal of physics D: Applied physics, 2003. **36**: p. 167-181.

41.   Harris, L.A., *Polymer Stabilized Magnetite Nanoparticles and Poly(propylene oxide) Modified Styrene-Dimethacrylate Networks* in *Virginia Polytechnic Institute and State University*. 2002.

42.   Bouchard LS, A.M., Liu GL, Hann B, Xie ZH, Gray JW, Wang X, Pines A, Chen FF, *Picomolar sensitivity MRI and photoacoustic imaging of cobalt nanoparticles.* Proc Natl Acad Sci U S A, 2009. **106**(11): p. 4085-4089.

43.   Verónica Salgueiriño-Maceira, M.A.C.-D., Michael Farle, M. Arturo López-Quintela, Karl Sieradzki, Rodolfo Diaz, *Synthesis and Characterization of Large Colloidal Cobalt Particles.* Langmuir, 2006. **22**(4): p. 1455-1458.

44.   Tran, N. and T.J. Webster, *Magnetic nanoparticles: biomedical applications and challenges.* Journal of Materials Chemistry, 2010. **20**(40).

45.   Moreno, R., et al., *The role of faceting and elongation on the magnetic anisotropy of magnetite Fe3O4 nanocrystals.* Scientific Reports, 2020. **10**(1): p. 2722.

46.   Muro-Cruces, J., et al., *Precise Size Control of the Growth of Fe(3)O(4) Nanocubes over a Wide Size Range Using a Rationally Designed One-Pot Synthesis.* ACS Nano, 2019. **13**(7): p. 7716-7728.

47.   Nassar, N. and M. Husein, *Preparation of iron oxide nanoparticles from FeCl3 solid powder using microemulsions.* physica status solidi (a), 2006. **203**(6): p. 1324-1328.

48.   Andrés Vergés, M., et al., *Uniform and water stable magnetite nanoparticles with diameters around the monodomain–multidomain limit.* Journal of Physics D: Applied Physics, 2008. **41**(13).

49.   Dokyoon Kim, N.L., Mihyun Park, Byung Hyo Kim, Kwangjin An, and Taeghwan Hyeon, *Synthesis of Uniform Ferrimagnetic Magnetite Nanocubes.* J. AM. CHEM. SOC, 2009. **131**(2): p. 454–455.

50.   Scopel, E., et al., *Synthesis of functionalized magnetite nanoparticles using only oleic acid and iron (III) acetylacetonate.* SN Applied Sciences, 2019. **1**(2).

51.   Soon Gu Kwon, Y.P., Jongnam Park, Subramanian Angappane, Younghun Jo, Nong-Moon Hwang, Je-Geun Park, Taeghwan Hyeon, *Kinetics of Monodisperse Iron Oxide Nanocrystal Formationby "Heating-Up" Process.* Journal of the American Chemical Society, 2007. **129**(41).

52.   Robert Davis, H.P.S., *Studies of Thermal Decarboxylation of Iron Carboxylates. I. Preparation of Symmetrical Aliphatic Ketones.* The Journal of Organic Chemistry, 1962. **27**(3).

53.   Narnaware, P.K. and C. Ravikumar, *Mechanistic Insights into the Formation and Growth of Anisotropic-Shaped Wüstite–Spinel Core–Shell Iron Oxide Nanoparticles in a Coordinating Solvent.* The Journal of Physical Chemistry C, 2020. **124**(45): p. 25010-25027.

54.   Qiao, L., et al., *Standardizing Size- and Shape-Controlled Synthesis of Monodisperse Magnetite (Fe3O4) Nanocrystals by Identifying and Exploiting Effects of Organic Impurities.* ACS Nano, 2017. **11**(6): p. 6370-6381.

55.   Dr. R. M. Cornell, P.e.D.D.h.c.U.S., *The Iron Oxides: Structure, Properties, Reactions, Occurences and Uses.* 2003: Wiley‐VCH Verlag GmbH & Co. KGaA.

56.   I. Prigogine, S.A.R., *Advances in Chemical Physics.* Vol. 98. 2008.

57.   Aghdasi, P., S. Yousefi, and R. Ansari, *Doping-induced changes in the structural and mechanical properties of germanene monolayers: A DFT-Based study.* Materials Science in Semiconductor Processing, 2024. **174**: p. 108246.

58.   Pandey, S., et al., *Effect of doping metal ions on microstructural evolution and dielectric behaviors of CaCu3Ti4O12 ceramics synthesized by semi-wet route.* Materials Chemistry and Physics, 2020. **253**: p. 123384.

59.   Abdelhamid, H.N., *Zeolitic Imidazolate Frameworks (ZIF-8) for Biomedical Applications: A Review.* Curr Med Chem, 2021. **28**(34): p. 7023-7075.

60.   Anekwe, I.M.S., B. Oboirien, and Y.M. Isa, *Effects of transition metal doping on the properties and catalytic performance of ZSM-5 zeolite catalyst on ethanol-to-hydrocarbons conversion.* Fuel Communications, 2024. **18**: p. 100101.

61.   Zoroddu, M.A., et al., *The essential metals for humans: a brief overview.* J Inorg Biochem, 2019. **195**: p. 120-129.

62.   Maret, W., *The Metals in the Biological Periodic System of the Elements: Concepts and Conjectures.* Int J Mol Sci, 2016. **17**(1).

63. Gammoh, N.Z. and L. Rink, *Zinc in Infection and Inflammation.* Nutrients, 2017. **9**(6).

64. Zyba, S.J., et al., *A moderate increase in dietary zinc reduces DNA strand breaks in leukocytes and alters plasma proteins without changing plasma zinc concentrations.* Am J Clin Nutr, 2017. **105**(2): p. 343-351.

65. Prasad, A.S., *Discovery of human zinc deficiency: its impact on human health and disease.* Adv Nutr, 2013. **4**(2): p. 176-90.

66. Emily Ho, B.N.A., *Low intracellular zinc induces oxidative DNA damage, disrupts p53, NFκB, and AP1 DNA binding, and affects DNA repair in a rat glioma cell line.* Proc. Natl. Acad. Sci. U. S. A., 2002. **99**(26): p. 16770-16775.

67. Kasparis, G., et al., *Zn doped iron oxide nanoparticles with high magnetization and photothermal efficiency for cancer treatment.* Journal of Materials Chemistry B, 2023. **11**(4): p. 787-801.

68. Yaghi, O.M. and H. Li, *Hydrothermal Synthesis of a Metal-Organic Framework Containing Large Rectangular Channels.* Journal of the American Chemical Society, 1995. **117**(41): p. 10401-10402.

69. Moghadam, P.Z., et al., *Development of a Cambridge Structural Database Subset: A Collection of Metal–Organic Frameworks for Past, Present, and Future.* Chemistry of Materials, 2017. **29**(7): p. 2618-2625.

70. Zhang, X., et al., *A historical overview of the activation and porosity of metal–organic frameworks.* Chemical Society Reviews, 2020. **49**(20): p. 7406-7427.

71. Moosavi, S.M., et al., *Understanding the diversity of the metal-organic framework ecosystem.* Nature Communications, 2020. **11**(1): p. 4068.

72. Felix Sahayaraj, A., et al., *Metal–Organic Frameworks (MOFs): The Next Generation of Materials for Catalysis, Gas Storage, and Separation.* Journal of Inorganic and Organometallic Polymers and Materials, 2023. **33**(7): p. 1757-1781.

73. Song, X., et al., *Revealing Structure Properties of ZIF-8 Particles Prepared by Wet Chemical Etching via 3D Electron Tomography.* ACS Materials Letters, 2021. **3**(2): p. 171-178.

74. Yin, H., et al., *Thermal stability of ZIF-8 under oxidative and inert environments: A practical perspective on using ZIF-8 as a catalyst support.* Chemical Engineering Journal, 2015. **278**: p. 293-300.

75. Sun, C.-Y., et al., *Zeolitic imidazolate framework-8 as efficient pH-sensitive drug delivery vehicle.* Dalton Transactions, 2012. **41**(23): p. 6906-6909.

76. Zheng, C., et al., *ZnO–DOX@ZIF-8 Core–Shell Nanoparticles for pH-Responsive Drug Delivery.* ACS Biomaterials Science & Engineering, 2017. **3**(10): p. 2223-2229.

77. Zhu, W., et al., *Facile preparation of succinylated-zein-ZIF-8 hybrid for enhanced stability and pH-responsive drug delivery.* Chemical Engineering Science, 2020. **228**: p. 115981.

78. Hoseinpour, V. and Z. Shariatinia, *Applications of zeolitic imidazolate framework-8 (ZIF-8) in bone tissue engineering: A review.* Tissue and Cell, 2021. **72**: p. 101588.

79. Wang, Y., et al., *Biomimetic ZIF-8 Nanoparticles: A Novel Approach for Biomimetic Drug Delivery Systems.* Int J Nanomedicine, 2024. **19**: p. 5523-5544.

80. Hara, N., *ZIF-8 Membrane*, in *Encyclopedia of Membranes*, E. Drioli and L. Giorno, Editors. 2016, Springer Berlin Heidelberg: Berlin, Heidelberg. p. 2064-2067.

81. Iler, R.K., *Multilayers of colloidal particles.* Journal of Colloid and Interface Science, 1966. **21**(6): p. 569-594.

82. Petrila, L.M., et al., *Polyelectrolyte Multilayers: An Overview on Fabrication, Properties, and Biomedical and Environmental Applications.* Materials (Basel), 2021. **14**(15).

83. del Mercato, L.L., et al., *LbL multilayer capsules: recent progress and future outlook for their use in life sciences.* Nanoscale, 2010. **2**(4): p. 458-467.

84. Oberdick, S.D., et al., *Iron oxide nanoparticles as positive T1 contrast agents for low-field magnetic resonance imaging at 64 mT.* Scientific Reports, 2023. **13**(1): p. 11520.

85. Hunter, A.C., *Molecular hurdles in polyfectin design and mechanistic background to polycation induced cytotoxicity.* Advanced Drug Delivery Reviews, 2006. **58**(14): p. 1523-1531.

86. Fischer, D., et al., *In vitro cytotoxicity testing of polycations: influence of polymer structure on cell viability and hemolysis.* Biomaterials, 2003. **24**(7): p. 1121-1131.

87. Bieber, T., et al., *Intracellular route and transcriptional competence of polyethylenimine–DNA complexes.* Journal of Controlled Release, 2002. **82**(2): p. 441-454.

88. Godbey, W.T., K.K. Wu, and A.G. Mikos, *Size matters: Molecular weight affects the efficiency of poly(ethylenimine) as a gene delivery vehicle.* Journal of Biomedical Materials Research, 1999. **45**(3): p. 268-275.

89. Seiler, N. and F. Raul, *Polyamines and apoptosis.* Journal of Cellular and Molecular Medicine, 2005. **9**(3): p. 623-642.

90. Brkovic, N., et al., *Quantitative Assessment of Endosomal Escape of Various Endocytosed Polymer-Encapsulated Molecular Cargos upon Photothermal Heating.* Small, 2020. **16**(46): p. 2003639.

91. Carregal-Romero, S., et al., *Magnetically triggered release of molecular cargo from iron oxide nanoparticle loaded microcapsules.* Nanoscale, 2015. **7**(2): p. 570-576.

92. Arango MT, Q.-R.P., Castiblanco J, et al, *Chapter 45 Cell culture and cell analysis*. Autoimmunity: From Bench to Bedside, ed. S.Y. Anaya JM, Rojas-Villarraga A, et al. 2013.

93. Segeritz, C.-P. and L. Vallier, *Chapter 9 - Cell Culture: Growing Cells as Model Systems In Vitro*, in *Basic Science Methods for Clinical Researchers*, M. Jalali, F.Y.L. Saldanha, and M. Jalali, Editors. 2017, Academic Press: Boston. p. 151-172.

94. Sangeeta, B., et al., *Two-Dimensional and Three-Dimensional Cell Culture and Their Applications*, in *Cell Culture*, Z. Xianquan, Editor. 2021, IntechOpen: Rijeka. p. Ch. 3.

95. Kapałczyńska, M., et al., *2D and 3D cell cultures – a comparison of different types of cancer cell cultures.* Archives of Medical Science, 2018. **14**(4): p. 910-919.

96. Renz, M., *Fluorescence microscopy—A historical and technical perspective.* Cytometry Part A, 2013. **83**(9): p. 767-779.

97. Herschel, J.F.W., *IV.Ἀμόρφωτα, no. I.—on a case of superficial colour presented by a homogeneous liquid internally colourless.* Philosophical Transactions of the Royal Society of London, 1845(135): p. 143-145.

98. Stokes, G.G., *XXX. On the change of refrangibility of light.* Philosophical transactions of the Royal Society of London, 1852(142): p. 463-562.

99. Jonkman, J., et al., *Tutorial: guidance for quantitative confocal microscopy.* Nature Protocols, 2020. **15**(5): p. 1585-1611.

100. Zipfel, W.R., R.M. Williams, and W.W. Webb, *Nonlinear magic: multiphoton microscopy in the biosciences.* Nature Biotechnology, 2003. **21**(11): p. 1369-1377.

101. Drobizhev, M., et al., *Two-photon absorption properties of fluorescent proteins.* Nature Methods, 2011. **8**(5): p. 393-399.

102. Schenck, J.F., et al., *Human exposure to 4.0-Tesla magnetic fields in a whole-body scanner.* Medical Physics, 1992. **19**(4): p. 1089-1098.

103. Davis, K., et al., *Quantitative Measurement of Ligand Exchange with Small-Molecule Ligands on Iron Oxide Nanoparticles via Radioanalytical Techniques.* Langmuir, 2016. **32**(51): p. 13716-13727.

104. Carrillo-Carrión, C., et al., *Aqueous Stable Gold Nanostar/ZIF-8 Nanocomposites for Light-Triggered Release of Active Cargo Inside Living Cells.* Angewandte Chemie International Edition, 2019. **58**(21): p. 7078-7082.

105. Lin, C.-A.J., et al., *Design of an Amphiphilic Polymer for Nanoparticle Coating and Functionalization.* Small, 2008. **4**(3): p. 334-341.

106. Hühn, J., et al., *Selected Standard Protocols for the Synthesis, Phase Transfer, and Characterization of Inorganic Colloidal Nanoparticles.* Chemistry of Materials, 2017. **29**(1): p. 399-461.

107. Li, Q., et al., *Correlation between particle size/domain structure and magnetic properties of highly crystalline Fe3O4 nanoparticles.* Scientific Reports, 2017. **7**(1): p. 9894.

108. Akay, S., et al., *Solubility of coumarin in (ethanol + water) mixtures: Determination, correlation, thermodynamics and preferential solvation.* Journal of Molecular Liquids, 2021. **339**: p. 116761.

109. Kampferbeck, M., et al., *Little Adjustments Significantly Simplify the Gram-Scale Synthesis of High-Quality Iron Oxide Nanocubes.* Langmuir, 2021. **37**(32): p. 9851-9857.

Eidesstattliche Erklärung / Affidavit

versichere ich an Eid statt, die vorliegende Dissertationsschrift selbst verfasst und keine anderen als die angegebenen Hilfsmittel und Quellen benutzt zu haben. Sofern im Zuge der Erstellung der vorliegenden Dissertationsschrift generative Künstliche Intelligenz (gKI) basierte elektronische Hilfsmittel verwendet wurden, versichere ich, dass meine eigene Leistung im Vordergrund stand und dass eine vollständige Dokumentation aller verwendeten Hilfsmittel gemäß der Guten wissenschaftlichen Praxis vorliegt.

I hereby declare on oath that I have authored the present dissertation myself and have not used any sources or tools other than those specified. In the course of preparing this dissertation, if any generative artificial intelligence (gAI) based electronic tools were used, I assure that my own contributions were paramount and that a complete documentation of all used tools is available in accordance with good scientific practice.

Hamburg 05.12.2024

Ort, Datum   Unterschrift